UNIVERSITÀ DI PISA

Dipartimento di fisica "Enrico Fermi"
Scuola di dottorato in scienze di base "Galileo Galilei"
Dottorato di ricerca in fisica

Maggio 2014

Tesi di dottorato

Touschek lifetime studies and optimization of the ESRF: present and upgraded lattice

Candidato:
Nicola Carmignani

Relatore:
Prof. Franco Cervelli

Correlatori:
Dott. Laurent Farvacque
Dott. Pantaleo Raimondi

Contents

Introduction

The lifetime of the electron beam in a storage ring is a measure of how fast the electrons are being lost. This is an important parameter in third generation synchrotron light sources for a number of reasons. First of all, the intensity of radiation seen in an experiment, at the end of a beamline, is proportional to the electron beam current. Further, as the current changes, there are important effects on the x-ray optics along the beamline. Changes in heat-load can effect the transport and focusing properties of the beamline. For these reasons, more electrons must be injected when the current drops below some threshold value.

The electron beam lifetime determines the injection frequency. If the lifetime is long enough, the injections can be done less frequently. The injection disturbs the stability of the stored beam, it increases the radiation losses and it increases the energy consumption of the facility, because the linac and the synchrotron booster must be turned on during the injection.

When the lifetime is too short, the top-up injection is needed. The top-up injection is a very frequent injection of electrons into the storage ring, one every few minutes, and it is done without interrupting the x-ray flux and the users' experiments. Top-up injection needs a high injection efficiency.

In the ESRF storage ring, the top-up injection is not used now. In the low emittance ESRF upgrade storage ring, the top-up injection will be used, because the very low horizontal emittance, from the actual $\varepsilon_x = 4\,\mathrm{nm}$ to $\varepsilon_x = 150\,\mathrm{pm}$, will result in a very short Touschek lifetime.

The Touschek effect is the main limitation in the beam lifetime in third generation synchrotron light sources. It is a single scattering between two electrons of the bunch. The collision can transfer momentum from transverse to longitudinal motion and both the electrons can exceed the momentum acceptance, in which case they are lost. The Touschek scattering probability is larger when the charge density is high, so when emittances and β functions are small and the current is high.

The Touschek effect depends on many electron beam and machine parameters: the RF voltage, the bunch current, the bunch length, the beam emittances and the

momentum acceptance.

The small horizontal emittance storage rings, necessary to have a high brilliance x-ray source, have small β-functions and horizontal dispersion and strong focusing magnets. The natural chromaticity of low emittance rings is very high and strong sextupole magnets are needed to correct it.

High nonlinear fields from sextupoles cause a high amplitude-dependent tune variation. The large tune shift with amplitude causes many resonance crossings for off-axis particles and therefore a small dynamic aperture. The small dynamic aperture causes a small injection efficiency.

The positive chromaticity, needed for the bunch stability, and the strong nonlinear fields give large tunes variation with momentum. This can cause the strong resonance crossing of off-momentum particles and therefore a small momentum acceptance. The small momentum acceptance causes a short Touschek lifetime.

Momentum acceptance is determined by RF voltage and longitudinal dynamic acceptance, which depends on the sextupole setting.

A model able to predict the Touschek lifetime, given the lattice, the current, the emittances, the RF voltage, the size of the vacuum chamber, is useful to optimize the parameters of the present ESRF lattice and the new low emittance ESRF upgrade lattice.

In this thesis, a model able to predict lifetime of the beam has been developed and tested with measurements and it has been used to optimize parameters and sextupole settings. The model is also used for the new lattice lifetime studies.

In chapter 1, a brief description of the ESRF facility and on its upgrade program is given.

In chapter 2, the Touschek lifetime derivation, from the Møller scattering differential cross section, is presented. The effects of the spin polarization in the Touschek lifetime are also treated.

In chapter 3, the measurements of some parameters, relevant for the Touschek lifetime, done for the ESRF storage ring, are reported. The RF voltage calibration factor between the readout value and the real voltage applied to the cavity is measured from the synchrotron tune and the synchronous phase measurements. A bunch lengthening with current model, derived from measurements, is presented. The momentum acceptance computation, using a 6-D particle tracking code, is described.

In chapter 4, the lifetime measurements are described: the vacuum lifetime, that must be measured before all the Touschek lifetime measurements; the effect of the spin polarization on the Touschek lifetime and the spin polarization time; the

Touschek lifetime versus the RF voltage; the Touschek lifetime versus the horizontal scraper position.

In chapter 5, the optimization of the sextupole setting is described: the multi-objective generic algorithm used is described, the results of the optimization and the measurements are reported.

In chapters 6 and 7, the Touschek lifetime model, described in previous chapters, is used to study the Touschek lifetime of the low emittance ESRF upgrade lattice. The bunch length model and the emittance growth due to the intrabeam scattering are used to predict the Touschek lifetime of the new lattice for different modes.

In first appendix, an overview of the beam physics in an electron storage ring is given. In the first section, the single particle dynamics without synchrotron radiation is treated. In the second section, the effects of synchrotron radiation on the single particle dynamics are reported. In the third section two current dependent effects, related to the beam lifetime, are treated: the bunch lengthening effect due to the longitudinal wakefield and the intrabeam scattering.

In second appendix, a `matlab` code, developed during the thesis work and used to simulate the spin depolarization with a kicker, is described.

In third appendix, two possible momentum compaction factor measurements are presented.

In fourth appendix, the effect of synchrotron motion on the dynamic aperture computation is described.

Chapter 1

The European Synchrotron Radiation Facility

The European Synchtotron Radiation Facility (ESRF) is a laboratory with third generation synchrotron light source, located in Grenoble, France. It is supported by 19 countries.

The ESRF started operations in 1994. About 6000 researchers from around the world visit the ESRF every year. More than 21700 scientific papers, based on work carried out at the ESRF, have been published since the foundation. The facility guarantees a high reliability. In 2012, the beam availability was more than 98% of the time scheduled for the users [1]. The facility provides 42 X-rays beamlines, with a wide range of spectra from undulators and bending magnets.

The ESRF accelerator complex is composed of a linear accelerator, a synchrotron booster and a storage ring. The linear accelerator accelerates electrons up to 200 MeV, the booster then accelerates the electrons up to 6.04 GeV. The storage ring does not change the beam energy, except to replenish that which is lost to synchrotron radiation.

An aerial view of the ESRF is shown in figure 1.1.

The orbit of the electrons in the storage ring has a circumference of 844 m. The ring is composed of 32 double bend achromat cells, each with two bending magnets, six quadrupole magnets and seven sextupole magnets.

Three sextupoles are placed in the high dispersion area, between the two dipoles, and they are used to correct the chromaticity. Four sextupoles are placed in low dispersion areas and they are used as harmonic sextupoles, to control the non-linear geometric effects.

In the ring, there are seven sextupole families and it is not possible to change gradients of some sextupoles without changing the family gradient.

Figure 1.1: Aerial view of the European Synchrotron Radiation Facility.

At the end of every cell, in the straight sections, there are the undulators. Undulators produce synchrotron radiation, along with the bending magnets.

The horizontal emittance of the beam in the storage ring is about $\epsilon_x = 4\,\mathrm{nm}$.

In figure 1.2 the beta functions and the horizontal dispersion of two cells are shown.

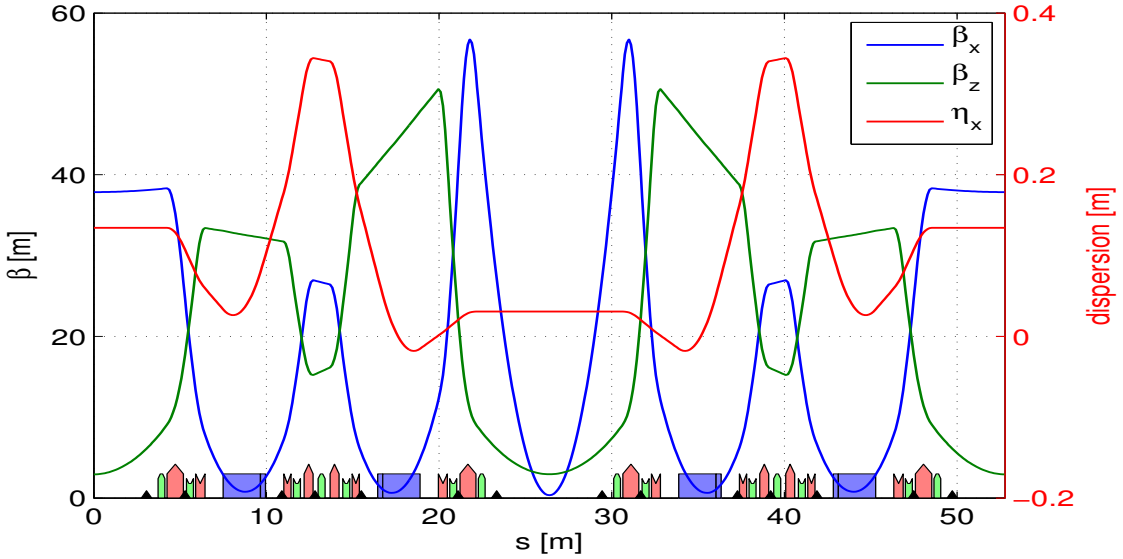

Figure 1.2: Beta functions and horizontal dispersion in two cells of the ESRF storage ring. Blue magnets are the dipoles, red magnets are the quadrupoles and green magnets are the sextupoles.

The β functions and the dispersion have a periodicity of two cells. Two adjacent cells have a mirror symmetry structure. Half of the straight sections have a low horizontal beta function ($\beta_x \simeq 33\,\mathrm{cm}$), half of them have a high horizontal beta function ($\beta_x \simeq 36\,\mathrm{m}$). The horizontal dispersion is slightly different in high beta and low beta straight sections.

There are four RF cavities which can provide a total RF voltage up to around 9 MV. The harmonic number is 992, which determines the maximum number of bunches that can be stored. The frequency of the RF cavity is 992 times the electron revolution frequency.

$$f_{RF} = h\, f_0 \simeq 353\,\mathrm{MHz} \tag{1.1}$$

The number of bunches and the current per bunch can be changed in order to have different operation modes for different experiments. The filling modes, with the total current, the number of bunches, the current per bunch, the electric charge per bunch, the number of electrons per bunch and a typical value of the lifetime are shown in table 1.1.

Table 1.1: Operation modes used at ESRF.

Mode	I (mA)	n_b	I_b (mA)	Q_b (nC)	$N_b(\times 10^9)$	LT (h)
Multi-bunch (uniform)	200	992	0.202	0.568	3.54	60
Multi-bunch (7/8)	200	868	0.230	0.649	4.05	55
16 bunches	92	16	5.62	15.8	98.8	10
4 bunches	40	4	10	28.1	176	6

A list of parameters of the ESRF storage ring is shown in table 1.2.

Table 1.2: Parameters for ESRF lattice, in multi-bunch mode.

Parameter	Value
Energy [GeV]	6.04
Circumference [m]	844.391
Beam current [mA]	200
ν_x	36.44
ν_y	13.39
ν_z	0.00543
α	$1.78 \cdot 10^{-4}$
τ_x, τ_y, τ_s [ms]	6.97, 6.98, 3.49
U_0 [MeV]	4.88
V_{rf} [MV]	8
h	992
ε_x [pm rad]	4000
ε_y [pm rad]	4
σ_δ	$1.03 \cdot 10^{-3}$

1.1 Upgrade program

An upgrade program of the ESRF is under study. A new low-emittance lattice will replace the present double-bend achromat one [2].

The new lattice project must satisfy some requirements. The horizontal emittance must be reduced from the 4 nm of the present lattice, to less than 200 pm. The insertion device source points must be in the same positions, in order to use the present beamlines, and the bending magnet beamlines must be used, therefore the number of cells must be 32, as it is in the present ESRF storage ring. The present filling modes, described in table 1.1, must be provided. The injector of the new storage ring must not be changed. The energy loss per turn must be reduced, in order to reduce the operation costs.

The linear lattice functions of the low-emittance upgrade lattice are shown in figure 1.3. The periodicity of the linear lattice functions is one cell.

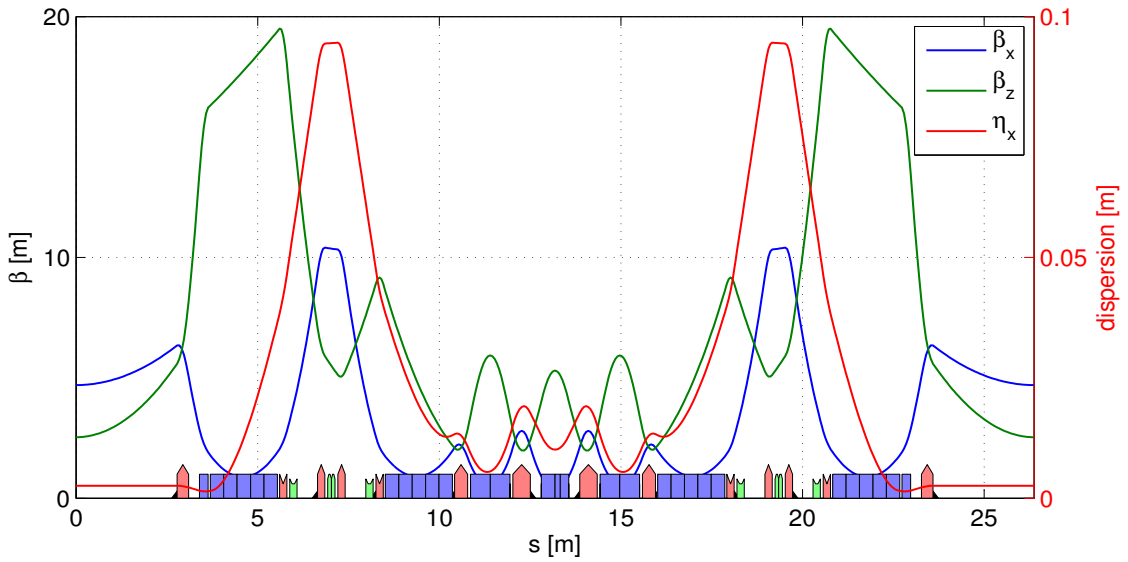

Figure 1.3: Beta functions and horizontal dispersion in one cell of the S28 version of the low-emittance ESRF upgrade lattice.

In order to have a small horizontal emittance, many other light sources have also proposed an upgrade with a multi bend achromat cell structure, such as the 7-bend achromat of MAX IV, the light source under construction in MAX-lab, Lund, Sweden [3].

In high energy large storage rings, like the ESRF one, the 7 bend scheme gives very weak dipoles and so a very small dispersion function. In order to correct the chromaticity, the sextupole strengths must be very high. A variation on the multi-bend scheme, inspired by the Super-B lattice [4], is used for the ESRF upgrade.

Between dipoles 1 and 2 and between dipoles 6 and 7, the distance is larger and the dispersion function grows. The sextupoles for the chromaticity corrections are placed in the dispersion bumps. With this scheme, a lower strength of the sextupoles is possible, compared with the normal multi-bend achromat scheme. The layout of the cell is called hybrid multi-bend lattice (HMB).

The three central dipoles have a quadrupolar defocusing field, i.e. the field has a transverse gradient. The other four quadrupoles have a longitudinal field gradient.

The injection of the beam into the storage ring is done in one of the straight sections. The low emittance and the low β functions are such that the dynamic aperture, i.e. the area in the transverse plane where a particle without transverse momentum can be injected without being lost, is too small. Two modified cells are designed for the injection region. The horizontal β function of the injection straight section is larger than the standard one, to satisfy the dynamic aperture requirements.

In figure 1.4, the two injection sections are shown.

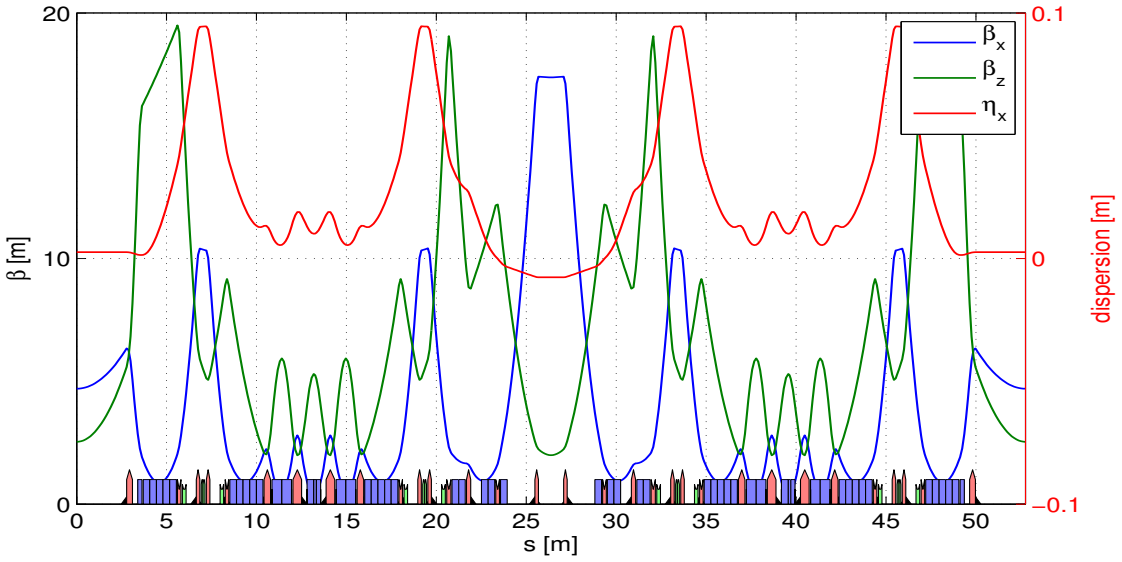

Figure 1.4: Beta functions and horizontal dispersion in the two injection cells of the S28 version of the low-emittance ESRF upgrade lattice.

In table 1.3 some parameters for the new low emittance lattice are shown.

The injection system of the new storage ring, i.e. the booster and the linac, will not be changed. The injection frequency will be higher than now, because the lifetime will be shorter.

Table 1.3: Parameters for ESRF upgrade lattice, version S28.

Parameter	value
Energy [GeV]	6.00
Circumference [m]	843.991
Beam current [mA]	200
ν_x	75.60
ν_y	27.60
ν_z	0.00345
α	$8.95 \cdot 10^{-5}$
τ_x, τ_y, τ_s [ms]	9.03, 13.9, 9.46
U_0 [MeV]	2.45
V_{rf} [MV]	6
h	992
ε_x [pm rad]	150
ε_y [pm rad]	5
σ_δ	$9.13 \cdot 10^{-4}$

Chapter 2

Touschek effect in electron storage rings

The electrons in a stable beam in a high energy particle accelerator can be lost due to the scattering with residual gas molecules in the beam pipe (elastic or inelastic scattering) or due to the scattering with other electrons of the beam (Touschek effect).

The two effects may be combined in terms of the total lifetime as follows:

$$\frac{1}{\tau} = \frac{1}{\tau_v} + \frac{1}{\tau_t} \tag{2.1}$$

where τ_t is the Touschek lifetime and τ_v is the vacuum lifetime.

Vacuum lifetime depends on the residual gas pressure inside the beam pipe. It varies with time, because the pressure is not constant during the machine operation and it is higher after the shutdowns. In third generation synchrotron light sources, vacuum lifetime is generally longer than Touschek lifetime.

The Touschek effect is a single scattering between two electrons of the bunch. The collision can transfer momentum from transverse to longitudinal motion and both the electrons can exceed the longitudinal acceptance, in which case they are lost.

The high density of particles into a small bunch increases the probability of collisions between particles. The elastic scattering between electrons is called Møller scattering. The Møller differential cross section is given at leading order by [5]:

$$\frac{\mathrm{d}\sigma}{\mathrm{d}\Omega} = \frac{4r_0^2}{\beta^4}\left(\frac{4}{\sin^4\theta} - \frac{3}{\sin^2\theta}\right) \tag{2.2}$$

In high energy accelerators, in the bunch frame, the transverse oscillation energy is larger than the longitudinal one. A collision can transfer momentum from trans-

verse to longitudinal motion and the electron can exceed the longitudinal acceptance limit.

The Møller cross section can be integrated on the solid angles which give a momentum deviation larger than the momentum aperture of the ring in a certain position. We note that it is assumed that the electron spin has been averaged over in the formula for the cross section. In the case where the beam is polarized, there is a correction term which we consider later.

The resulting Touschek lifetime, in non-relativistic approximation, with a flat beam, i.e. with a very small vertical oscillation, has been derived by Bruck [6] [7].

$$\frac{1}{\tau} = \left\langle \frac{{r_e}^2 c N_b}{8\pi\sigma_x\sigma_y\sigma_l\gamma^2} \frac{1}{\delta_{acc}^3} D(\epsilon) \right\rangle \tag{2.3}$$

where r_e is the classical electron radius, c is the speed of light, N_b is the number of electrons per bunch, σ_x, σ_y and σ_l are the bunch width, height and length, γ is the Lorentz factor, δ_{acc} is the momentum acceptance. $D(\epsilon)$ is defined as:

$$D(\epsilon) = \sqrt{\epsilon}\left[-\frac{3}{2}e^{-\epsilon} + \frac{\epsilon}{2}\int_\epsilon^\infty \frac{\ln u}{u} e^{-u}\mathrm{d}u + \frac{1}{2}\left(3\epsilon - \epsilon\ln\epsilon + 2\right)\int_\epsilon^\infty \frac{e^{-u}}{u}\mathrm{d}u\right] \tag{2.4}$$

where the parameter ϵ is:

$$\epsilon = \left(\frac{\delta_{acc}}{\gamma\sigma'_x}\right)^2 \tag{2.5}$$

and

$$\sigma'_x = \sqrt{\frac{\varepsilon_x}{\beta_x}} \tag{2.6}$$

For the ESRF storage ring, assuming $\beta_x = 1\,\mathrm{m}$, the value of ϵ is given by:

$$\epsilon = \frac{\delta_{acc}^2}{0.57} \tag{2.7}$$

The function $D(\epsilon)$ is shown in figure 2.1. The function $\frac{1}{\delta_{acc}^3}D(\epsilon)$ for the ESRF lattice is shown in figure 2.2.

Beam sizes, β functions and momentum acceptance are not constant along the ring, so the total lifetime has to be obtained averaging equation (2.3) on the whole ring.

Assuming a small variation of δ_{acc} along the ring, a scaling law for the Touschek lifetime can be obtained from equation (2.3):

$$\tau_t \propto \frac{\sqrt{\varepsilon_y}\sigma_z}{I_b}\delta_{acc}^3 \tag{2.8}$$

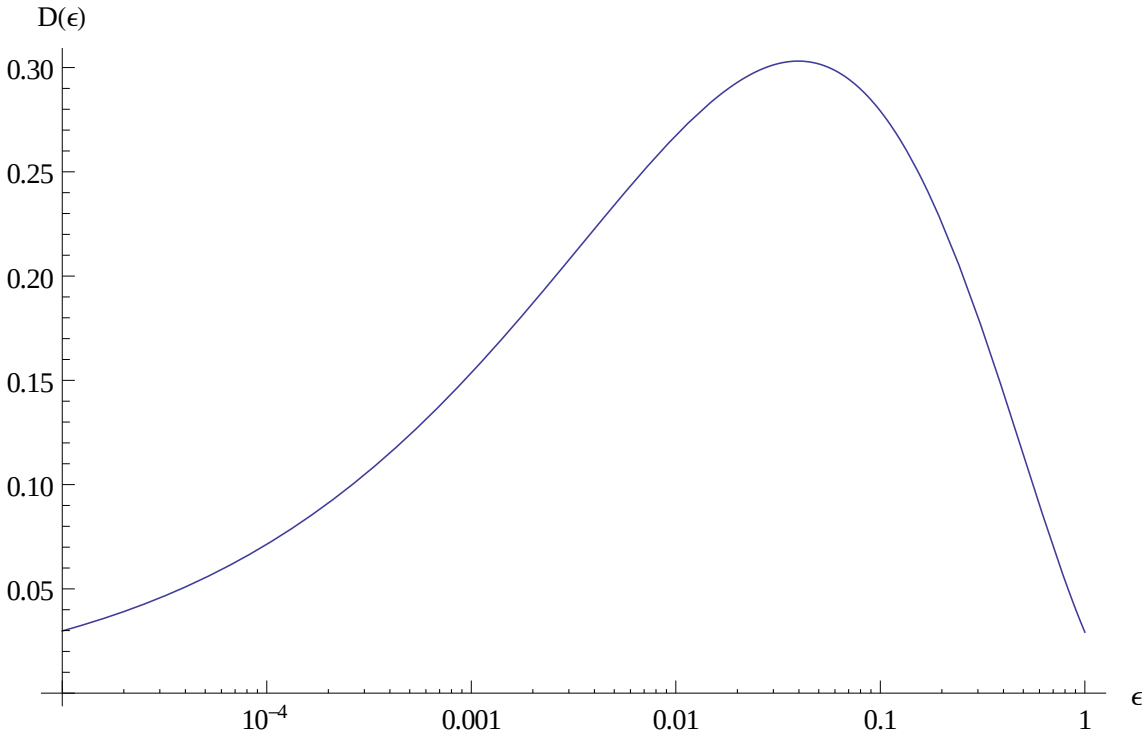

Figure 2.1: Function $D(\epsilon)$.

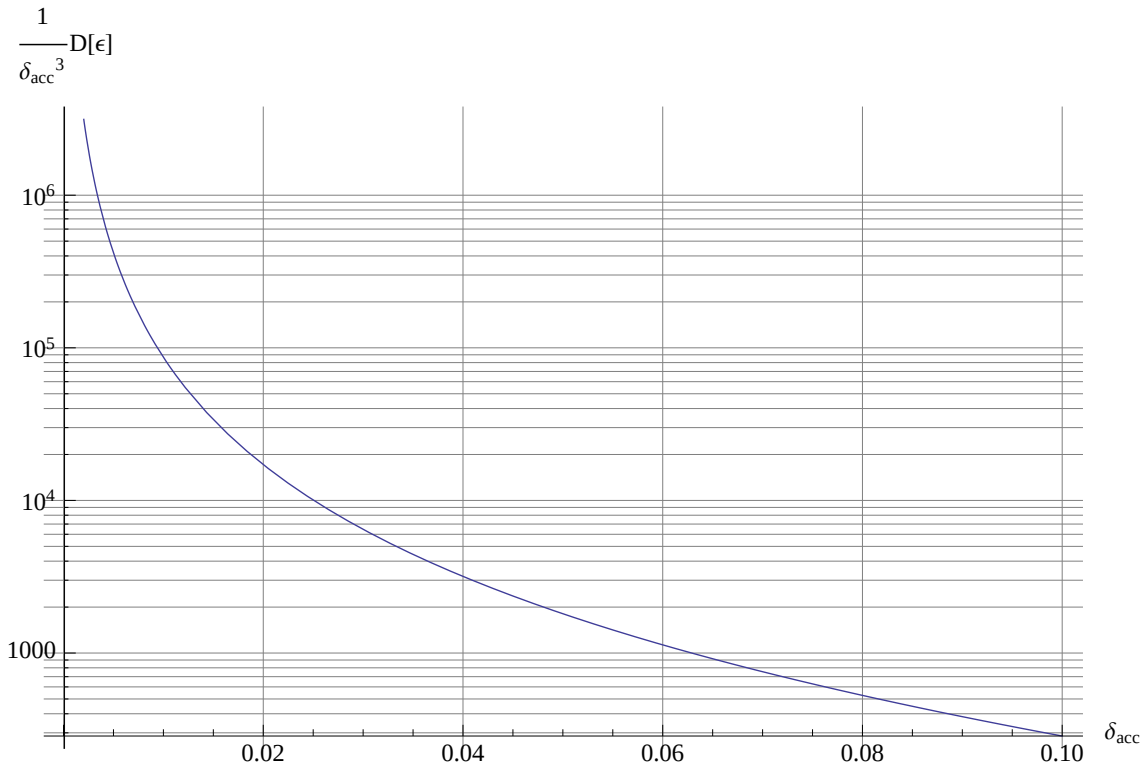

Figure 2.2: Function $\frac{1}{\delta_{acc}^3} D(\epsilon)$ as a function of δ_{acc}, assuming $\beta_x = 1\,\mathrm{m}$, for ESRF storage ring.

A more precise result has been obtained by Piwinski [8] [9]. Piwinski derivation is valid for a general case, with arbitrary energies in the rest frame of the colliding particles and arbitrary transverse beam envelops.

The inverse of Touschek lifetime derived by Piwinski is given by:

$$\frac{1}{\tau} = \left\langle \frac{r_o^2 c N_b}{8\pi\gamma^2\sigma_s\sqrt{\sigma_x^2\sigma_y^2 - \sigma_p^4 D_x^2 D_y^2 \tau_m}} F\left(\tau_m, B_1, B_2\right) \right\rangle \tag{2.9}$$

where σ_p is the energy spread, σ_s is the bunch length, D_x and D_y are the dispersion functions, σ_x and σ_x are the beam sizes defined by:

$$\sigma_x = \sqrt{\varepsilon_x\beta_x + \sigma_p^2 D_x^2} \tag{2.10}$$

$$\sigma_y = \sqrt{\varepsilon_y\beta_y + \sigma_p^2 D_y^2} \tag{2.11}$$

and

$$\tau_m = \beta^2\delta_{acc}^2 \tag{2.12}$$

the function $F\left(\tau_m, B_1, B_2\right)$ is:

$$F\left(\tau_m, B_1, B_2\right) = \sqrt{\pi\left(B_1^2 - B_2^2\right)}\tau_m \int_{\tau_m}^{\infty} \left[\left(2 + \frac{1}{\tau}\right)^2 \left(\frac{\tau/\tau_m}{1+\tau} - 1\right) + 1 - \frac{\sqrt{1+\tau}}{\sqrt{\tau/\tau_m}} - \frac{1}{2\tau}\left(4 + \frac{1}{\tau}\right)\ln\frac{\tau/\tau_m}{1+\tau} \right] e^{-B_1\tau} I_0\left(B_2\tau\right) \frac{\sqrt{\tau}\mathrm{d}\tau}{\sqrt{1+\tau}} \tag{2.13}$$

where I_0 is the modified Bessel function. The functions B_1 and B_2 are given by:

$$B_1 = \frac{\beta_x^2}{2\beta^2\gamma^2\sigma_{x\beta}^2}\left(1 - \frac{\sigma_h^2\tilde{D}_x^2}{\sigma_{x\beta}^2}\right) + \frac{\beta_y^2}{2\beta^2\gamma^2\sigma_{y\beta}^2}\left(1 - \frac{\sigma_h^2\tilde{D}_y^2}{\sigma_{y\beta}^2}\right) \tag{2.14}$$

$$B_2^2 = B_1^2 - \frac{\beta_x^2\beta_y^2\sigma_h^2}{\beta^4\gamma^4\sigma_{x\beta}^4\sigma_{y\beta}^4\sigma_p^2}\left(\sigma_x^2\sigma_y^2 - \sigma_p^4 D_x^2 D_y^2\right) \tag{2.15}$$

$\tilde{D}_x$ and $\tilde{D}_y$ are given by:

$$\tilde{D}_x = \alpha_x D_x + \beta_x D_x' \tag{2.16}$$

$$\tilde{D}_y = \alpha_y D_y + \beta_y D_y' \tag{2.17}$$

where D'_x and D'_y are the slopes dispersion functions. σ_h is defined by:

$$\frac{1}{\sigma_h^2} = \frac{1}{\sigma_p^2 \sigma_{x\beta}^2 \sigma_{y\beta}^2} \left(\tilde{\sigma}_x^2 \sigma_{y\beta}^2 + \tilde{\sigma}_y^2 \sigma_{x\beta}^2 - \sigma_{x\beta}^2 \sigma_{y\beta}^2 \right) \tag{2.18}$$

$\sigma_{x\beta}$, $\tilde{\sigma}_x$, $\sigma_{y\beta}$ and $\tilde{\sigma}_y$ are defined:

$$\sigma_{x\beta} = \sqrt{\varepsilon_x \beta_x} \tag{2.19}$$

$$\tilde{\sigma}_x = \sqrt{\sigma_x^2 + \sigma_p^2 \left(D_x^2 + \tilde{D}_x^2 \right)} \tag{2.20}$$

$$\sigma_{y\beta} = \sqrt{\varepsilon_y \beta_y} \tag{2.21}$$

$$\tilde{\sigma}_y = \sqrt{\sigma_y^2 + \sigma_p^2 \left(D_y^2 + \tilde{D}_y^2 \right)} \tag{2.22}$$

β and γ are the relativistic factors, β_x, β_y, α_x and α_y are the Twiss functions.

Beam sizes, β functions, momentum acceptance are not constant along the ring, so the total lifetime has to be obtained averaging equation (2.9) on the whole ring.

2.1 Spin polarization in electron storage rings

The polarization of an electron beam is the average value of the vertical spin of the electrons.

An electron beam with an initial random distribution of the spin becomes polarized over time due to the Sokolov-Ternov effect [10] [11]. A little fraction of the photons emitted as synchrotron radiation causes a spin-flip to the electrons.

The transition rates between the two possible spin status are:

$$W_{\uparrow\downarrow} = \frac{5\sqrt{3}}{16} \frac{r_e \gamma^5 \hbar}{m_e} \left\langle \frac{1}{\rho^3} \right\rangle \left(1 + \frac{8}{5\sqrt{3}} \right) \tag{2.23}$$

and

$$W_{\downarrow\uparrow} = \frac{5\sqrt{3}}{16} \frac{r_e \gamma^5 \hbar}{m_e} \left\langle \frac{1}{\rho^3} \right\rangle \left(1 - \frac{8}{5\sqrt{3}} \right) \tag{2.24}$$

where r_e is the electron classical radius, γ is the Lorentz relativistic factor, $\hbar$ is the reduced Planck constant, m_e is the electron mass, ρ is the instantaneous bending radius of dipoles. The symbol $\uparrow$ denotes a spin along the magnetic field and the symbol $\downarrow$ denotes a spin opposite to the magnetic field.

These two transition rates are different and so an unpolarized beam becomes

polarized. The maximum value of polarization achievable is given by:

$$P_{ST} = \frac{W_{\uparrow\downarrow} - W_{\downarrow\uparrow}}{W_{\uparrow\downarrow} + W_{\downarrow\uparrow}} = \frac{8}{5\sqrt{3}} \simeq 0.9238 \tag{2.25}$$

where P_{ST} is called the Sokolov-Ternov level of polarization.

The polarization follows an exponential law:

$$P(t) = P_{ST}\left(1 - e^{-t/\tau_p}\right) \tag{2.26}$$

The exponential time constant for the polarization effect is given by:

$$\tau_p^{-1} = W_{\uparrow\downarrow} + W_{\downarrow\uparrow} = \frac{5\sqrt{3}}{8}\frac{r_e \hbar \gamma^5}{m_e}\left\langle \frac{1}{\rho^3} \right\rangle \tag{2.27}$$

The average of $1/\rho^3$ is given by:

$$\left\langle \frac{1}{\rho^3} \right\rangle = \frac{1}{C}\oint \frac{1}{\rho^3(s)} \mathrm{d}s \tag{2.28}$$

where C is the total length of the ring and s is the longitudinal coordinate.

Spin depolarization

The spin of the electrons does a precession around the magnetic field of the dipoles, following the Thomas-BMT equation.

The number of total precessions done by the electrons in a revolution time is the spin tune and it is given by:

$$\nu_{spin} = \frac{g-2}{2}\,\gamma \tag{2.29}$$

where γ is the Lorentz relativistic factor and $a = \frac{g-2}{2}$ is the electron anomalous magnetic dipole moment. Its value is [12]:

$$a = \frac{g-2}{2} = (1.15965218076 \pm 0.00000000027) \times 10^{-3} \tag{2.30}$$

The precession frequency of the electron spin is proportional to the beam energy:

$$f_{spin} = f_0\,\nu_{spin} = f_0\,a\,\gamma \tag{2.31}$$

where f_0 is the revolution frequency.

If a vertical kick, from an horizontal magnetic field, is applied to the beam, the electron spin vector is rotated by an angle, around the magnetic field direction, given

by:

$$\theta_{spin} = \nu_{spin}\,\theta_k \tag{2.32}$$

where θ_k is the kick given by the kicker to the beam in radians.

The kicker can be powered with an angular frequency resonant with the spin tune:

$$\omega_{dep} = (\nu_{spin} \pm m)\,\omega_0 \tag{2.33}$$

where m is an integer and $\omega_0 = 2\pi f_0$.

The rotation angle given to the spin vector, as a function of time, is:

$$\theta_{spin}(t) = |A_{spin}\cos(\omega_{dep}t)| \tag{2.34}$$

where $A_{spin} = A_k\,\nu_{spin}$ is the maximum rotation angle given by the kicker to the spin vector and A_k is the amplitude in radiants of the kick.

Assuming a beam without energy spread, with nominal energy, it can be depolarized if the spin vectors receive a rotation angle of $\pi/2$. This is achieved when the sum of the angles given to the spins is $\pi/2$:

$$\sum_{n=1}^{N} \theta_{spin}(nT_0) = \frac{\pi}{2} \tag{2.35}$$

The function $\theta_{spin}(t)$ is the absolute value of a sinusoidal function, its average value can be computed:

$$\langle\theta_{spin}\rangle = \frac{2A_{spin}}{\pi} \tag{2.36}$$

The number of turns needed to depolarize the beam, in the simple assumption of beam without energy spread, is given by:

$$N = \frac{\pi/2}{\langle\theta_{spin}\rangle} = \frac{\pi^2}{4A_{spin}} = \frac{\pi^2}{4A_k\nu_{spin}} \tag{2.37}$$

In electron storage rings, the beam has an energy spread and electrons suffer synchrotron oscillations. The spin tune is not constant, it oscillates with energy and there is a spin tune spread. The depolarization of a polarized electron beam can be studied only with a simulation. A simple spin tracking simulation program has been developed and is described in Appendix B.

Either the experimental results from different electron storage rings (LEP [13], SLS [14], Australian Synchrotron [15], Spear3 [15]) and the simulations show that the beam depolarization in real cases, with synchrotron oscillations, is possible only if the frequency of the kicker is in a narrow interval around the value of ω_{dep}, defined

in equation (2.33).

The size of the spin depolarization resonance has been studied with deuteron beams at COSY synchrotron, experimentally and with simulations [16]. In heavy particles beam, the synchrotron oscillations can be switched off, turning off the cavity, because the synchrotron radiation is negligible. In these experiments, it is confirmed that without synchrotron oscillations the resonance is broadened by the energy spread; with synchrotron oscillations the resonance becomes much narrower, even with energy spread.

Effect of spin polarization on Touschek lifetime

The Møller cross section is smaller if the beam is polarized [17] [18] [19]. When the beam is polarized, the Touschek lifetime is longer.

An expression for the effect of the polarization on Touschek lifetime is given in [20]. In particular, if P is the polarization, the Touschek lifetime is given by:

$$\frac{1}{\tau_t(P)} = \frac{1}{\tau_t(0)} + \left\langle R(\epsilon)\frac{1}{\tau_t(0)} \right\rangle P^2 \tag{2.38}$$

where

$$R(\epsilon) = \frac{F(\epsilon)}{C(\epsilon)} \tag{2.39}$$

with

$$C(\epsilon) = \epsilon \int_\epsilon^\infty \frac{1}{u^2}\left(\left(\frac{u}{\epsilon}\right) - \frac{1}{2}\ln\left(\frac{u}{\epsilon}\right) - 1\right) e^{-u}\mathrm{d}u \tag{2.40}$$

and

$$F(\epsilon) = -\frac{\epsilon}{2}\int_\epsilon^\infty \frac{1}{u^2}\ln\left(\frac{u}{\epsilon}\right) e^{-u}\mathrm{d}u \tag{2.41}$$

The quantity ϵ is given by:

$$\epsilon = \left(\frac{\delta_{acc}}{\gamma\sigma_{x'}}\right)^2 \tag{2.42}$$

where δ_{acc} is the momentum acceptance, γ is the Lorentz relativistic factor, $\sigma_{x'}$ is the standard deviation of the beam distribution in horizontal angle.

The value of $-F(\epsilon)/C(\epsilon)$ as a function of ϵ is shown in figure 2.3.

Effect of spin polarization in Touschek lifetime of ESRF storage ring

In the ESRF storage ring there are 64 compound dipoles, with a hard component and a soft one. The lengths and bending radii are:

$$L_H = 2.1573\,\mathrm{m} \quad \rho_H = 23.37\,\mathrm{m} \tag{2.43}$$

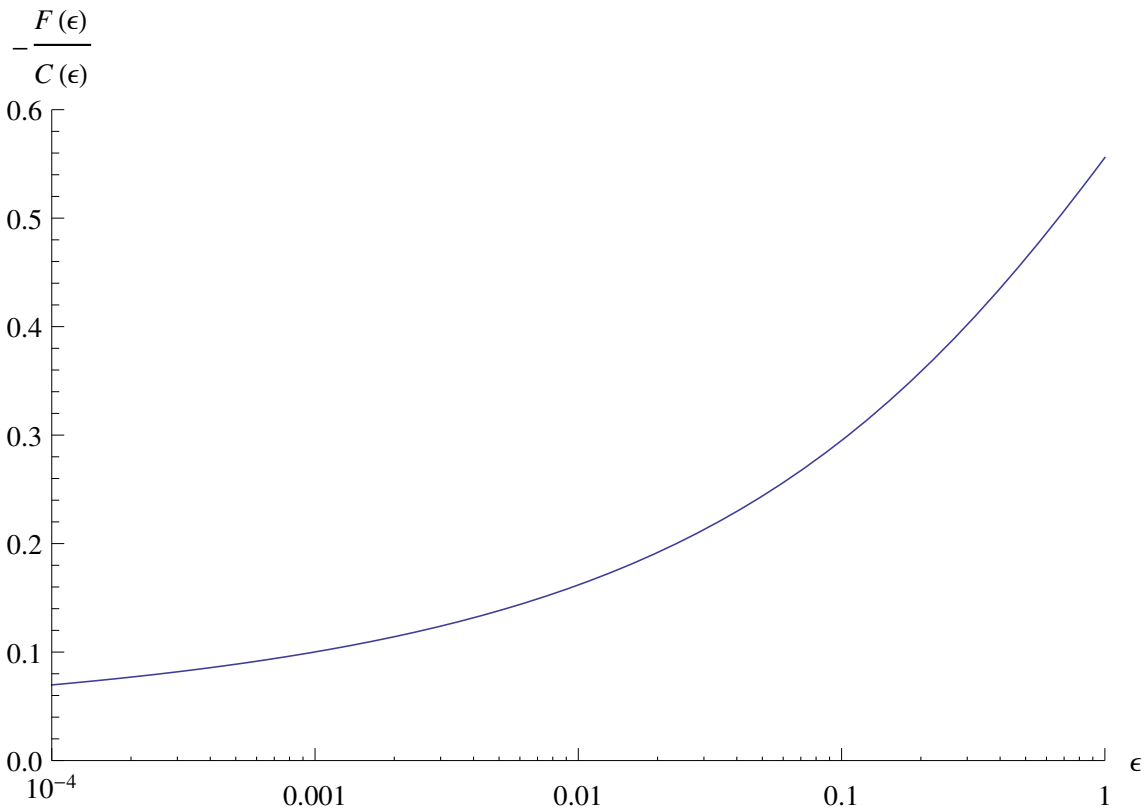

Figure 2.3: Function $-R(\epsilon) = -F(\epsilon)/C(\epsilon)$.

$$L_S = 0.2927\,\mathrm{m} \quad \rho_S = 49.61\,\mathrm{m} \tag{2.44}$$

The length Arc of the curvilinear trajectory of the particles, given the length L of the rectangular bending magnet and the curvature radius ρ of the particle, is given by:

$$Arc = 2\rho \arcsin \frac{L}{2\rho} \tag{2.45}$$

The average of the third power of the bending radius is given by:

$$\left\langle \frac{1}{\rho^3} \right\rangle = \frac{64}{C} \left(\frac{Arc_H}{\rho_H^3} + \frac{Arc_S}{\rho_S^3} \right) = 1.2997 \times 10^{-5}\,\mathrm{m}^{-3} \tag{2.46}$$

Using equations (2.27) and (2.46), the inverse of the polarization time can be computed. The polarization time (in minutes) for the ESRF storage ring is:

$$\tau_p = 15.75\,\mathrm{min} \tag{2.47}$$

Using the Sokolov-Ternov level of polarization, $S = 0.9238$, the beam sizes of the ESRF storage ring and a constant value of the momentum acceptance, the functions C and F in equations (2.40) and (2.41) have been computed by mean of `mathematica` [21] and the lifetime increase has been computed. In table 2.1, the increasing in Touschek lifetime for three different constant momentum acceptance are shown. We have assumed the maximum polarization P_{ST}.

Table 2.1: Touschek lifetime increase due to spin polarization, for five different constant momentum acceptances, for the ESRF storage ring.

δ_{acc} (%)	Lifetime increase (%)
1.5	12.20
2.0	13.75
2.5	15.09
3.0	16.27
3.5	17.30

Chapter 3

Touschek lifetime parameters measurements

The Touschek lifetime scales with bunch current, beam vertical emittance, bunch length and momentum acceptance, as derived in previous chapter:

$$\tau_t \propto \frac{\sqrt{\varepsilon_y}\sigma_z}{I_b}\delta_{acc}^3 \tag{3.1}$$

where ε_y is the vertical emittance, σ_z is the root mean square bunch length, I_b is the bunch current and δ_{acc} is the momentum acceptance.

In this chapter, the measurements of all the relevant parameters for the Touschek lifetime are discussed.

The vertical emittance can be measured using the x-ray pinhole cameras installed in the storage ring [22]. They are used to detect the bending magnets synchrotron radiation. The vertical emittance depends on the coupling between the horizontal and the vertical motion, that may be controlled using skew quadrupoles correctors, and on vertical dispersion. In exactly planar machine, in absence of coupling sources, the vertical dispersion is zero, because there are not vertical bending magnets, however, magnets misalignments produce non-zero vertical bending fields and vertical dispersion.

Vertical emittance can be increased applying an oscillating horizontal magnetic field, in a range of frequency that includes the vertical betatron oscillation frequency. This can be done using a vertical kicker.

The bunch current can be measured using the beam position monitors. In the ESRF storage ring, there are 224 beam position monitors: 7 per cell. The number of bunches depends on the operation mode and can be 4, 16, 868 or 992 (table 1.1). During machine dedicated times, it can be varied between 1 and 992, that is the

harmonic number of the RF cavity and the number of buckets. The total current is the sum of all the bunch currents. We assume throughout this thesis that the charge per bunch is the same in all bunches: $I_{tot} = N_b \cdot I_b$, where N_b is the number of bunches, I_b is the current per bunch and I_{tot} is the total current.

The zero-current bunch length is related to the energy spread of the electron beam and it is derived in the appendix A, in section A.2. The value is given by:

$$\sigma_{z0} = \frac{C\alpha}{2\pi\nu_s}\sigma_\delta \tag{3.2}$$

where C is the ring circumference, α is the momentum compaction factor, ν_s is the synchrotron tune and σ_δ is the equilibrium energy spread.

The synchrotron tune depends on the RF voltage as follows:

$$\nu_s = \sqrt{\frac{heV_{RF}\eta\cos\phi_s}{2\pi\beta^2 E_0}} \tag{3.3}$$

where h is the harmonic number, e is the electron charge, η is the phase-slip factor, ϕ_s is the synchronous phase, β is the relativistic factor and E_0 is the electron energy.

The phase-slip factor and the synchronous phase, as written in the appendix A, are given by:

$$\eta = \frac{1}{\gamma^2} - \alpha \tag{3.4}$$

$$\phi_s = \pi - \arcsin\left(\frac{U_0}{eV_{RF}}\right) \tag{3.5}$$

where γ is the Lorentz relativistic factor and U_0 is the energy loss per turn.

The interactions between the bunch and the vacuum chamber is responsible for the bunch lengthening.

The effect of the vacuum chamber can be described by an impedance and the relevant quantity for the lengthening effect is the parameter Z_n. The lengthening is current dependent, as explained in appendix A, section A.3.1. The lengthening effect is given by:

$$\left(\frac{\sigma_z}{\sigma_{z_0}}\right) = \frac{\sqrt[3]{\sqrt{3}\sqrt{27Q^2-4}+9Q}}{\sqrt[3]{18}} + \frac{\sqrt[3]{\frac{2}{3}}}{\sqrt[3]{\sqrt{3}\sqrt{27Q^2-4}+9Q}} \tag{3.6}$$

where σ_z/σ_{z_0} is the bunch lengthening, $Q = \frac{\Delta}{4\sqrt{\pi}}$ and

$$\Delta = \frac{\alpha e I_b}{E_0\nu_s^2}\left(\frac{c}{\omega_0\sigma_{z0}}\right)^3 Z_n \tag{3.7}$$

where c is the speed of light and ω_0 is the revolution angular frequency ($\omega_0 = 2\pi\frac{c}{C}$).

The bunch length can be measured using a streak camera.

A streak camera is an instrument able to measure the time structure of an ultra fast x-ray signal, in the range of picoseconds. The output is a picture where the spatial intensity is proportional to the time intensity of the original signal [23].

The x-rays hit the photo-cathode causing the emission of photo-electrons. The photo-electrons are bent by a time dependent electric field and the electrons goes into the detector screen in a position that depends on the arrival time.

The bunch length measurements done at ESRF, using a streak camera, in order to measure the parameter Z_n are shown in section 3.2.

The momentum acceptance is the maximum possible momentum displacement of a particle following scattering, without losing it. This quantity is different in different position of the ring, because the dispersion and the beta functions are not constant. In particular, if we consider linear motion, then the transverse action of a particle following a scatter with momentum change δ (see section A.1 of appendix A) is:

$$\Delta J_x = \mathcal{H}\delta^2 \tag{3.8}$$

where $\mathcal{H}$ is called the curly-H function and it is given by:

$$\mathcal{H}(s) = \gamma_x(s)D_x^2(s) + 2\alpha_x(s)D_x(s)D_x'(s) + \beta_x(s)D_x'^2(s) \tag{3.9}$$

where β_x, α_x and γ_x are the horizontal Twiss functions and D_x and D_x' are the horizontal dispersion and its derivative.

The positive and negative momentum acceptance can also be different, because of the nonlinear dispersion, i.e. the dependence of the closed orbit on the square of the momentum displacement.

The momentum acceptance δ_{acc} is a function of the position along the ring and it cannot be directly measured. It is not constant along the ring: it depends on the position in the cell. However, sometimes a useful single quantity is used: the Touschek relevant effective lattice momentum acceptance (TRELMA) [24]. The TRELMA is the value of constant momentum acceptance that must be chosen to have the same Touschek lifetime that we have with the real momentum acceptance.

The momentum acceptance is limited by two effects: the longitudinal bucket size, which is related to the accelerating voltage, and the dynamic momentum aperture, which depends on the nonlinear dynamics and in particular on the sextupole setting.

The longitudinal bucket size, or RF acceptance, is given by:

$$\delta_{RF} = \frac{2\nu_s}{h\alpha}\sqrt{1 - \left(\frac{\pi}{2} - \phi_s\right)\tan(\phi_s)} \tag{3.10}$$

where ν_s is the synchrotron tune, given in equation (3.3), h is the cavity harmonic number, α is the momentum compaction factor and ϕ_s is the synchronous phase, defined in equation (3.5).

Both the bunch length and the momentum acceptance depend on the voltage applied to the accelerating cavity. In order to have a model able to predict the Touschek lifetime, the RF voltage must be known.

Some measurements done at ESRF on 2011 showed that the readout value of the RF voltage was slightly different from the value applied to the cavity [25].

A calibration factor k can be defined as follows:

$$V_{RF} = kV_{ro} \tag{3.11}$$

where V_{RF} is the voltage applied to the cavity that gives the acceleration to the beam and V_{ro} is the readout value of the voltage from the high level application in the control room.

In the first section of this chapter, the measurements done in 2011, 2013 and 2014 to understand the voltage calibration are presented. Similar measurements have been done at LEP [26].

In the second section, the bunch length measurements done in order to obtain the bunch lengthening model with current are shown.

In third section, the momentum acceptance computations, using a 6-D particle tracking program, are shown.

3.1 RF voltage calibration factor measurement

The electrons in a storage ring does a longitudinal motion, called synchrotron motion. The frequency of the longitudinal motion in units of revolution frequency, the synchrotron tune, is derived in appendix A and it is given by:

$$\nu_s = \sqrt{-\frac{eV_{RF}}{E_0}\frac{h\alpha}{2\pi}\cos\phi_s} \tag{3.12}$$

where e is the electron charge, V_{RF} is the RF voltage, h is the harmonic number of the cavity, α is the momentum compaction factor, E_0 is the electron beam energy and ϕ_s is the synchronous phase.

The synchronous phase is the relative phase between the beam and the cavity and it is given by:

$$\phi_s = \pi - \arcsin\left(\frac{U_0}{eV_{RF}}\right) \tag{3.13}$$

where U_0 is the energy loss per turn.

Using equations 3.12 and 3.13, the frequency of the synchrotron oscillations can be written:

$$f_s = f_{RF}\sqrt{\frac{\alpha}{2\pi h E_0}}\left({V_{RF}}^2 - {U_0}^2\right)^{1/4} \tag{3.14}$$

where f_{RF} is the RF cavity frequency.

The synchrotron tune and the synchronous phase depend on the RF voltage and they can be used to measure the RF voltage calibration factor.

Synchrotron tune measurement

The synchrotron tune can be measured exciting the electrons longitudinally with the bunch by bunch longitudinal feedback and measuring the sidebands of an harmonic of the revolution frequency. The resolution on synchrotron tune measurement is better than 1 %.

In figure 3.1, the synchrotron oscillation frequency measurements performed in 2011 and 2013 are plotted together with the expected value (red line). The expected value is computed using formula of equation (3.14), assuming the calibration of the RF voltage $k = 1$ and using the nominal values of the ring parameters (U_0, α, E_0).

All these measurements have been done with undulator gaps opened, in order to lose energy only for synchrotron radiation due to the dipole magnets.

The measurement of July 2011 was close to the expected value of the synchrotron tune, while the measurements of February 2011 and the two of 2013 are very similar but far from the expected value.

The synchrotron tune measurements can be fitted in order to obtain the RF voltage calibration factor.

Equation 3.14 can be written, using equation 3.11:

$$f_s = f_{RF}\sqrt{\frac{\alpha}{2\pi h E_0}}\left(k^2{V_{ro}}^2 - {U_0}^2\right)^{1/4} \tag{3.15}$$

A two parameters fit of the measured synchrotron tune versus the readout value of the RF voltage can be done.

If we assume to know the energy E_0 of the beam, and therefore the mean energy loss per turn U_0, we can fit the synchrotron tune and find the best values for the calibration factor k and the momentum compaction factor α.

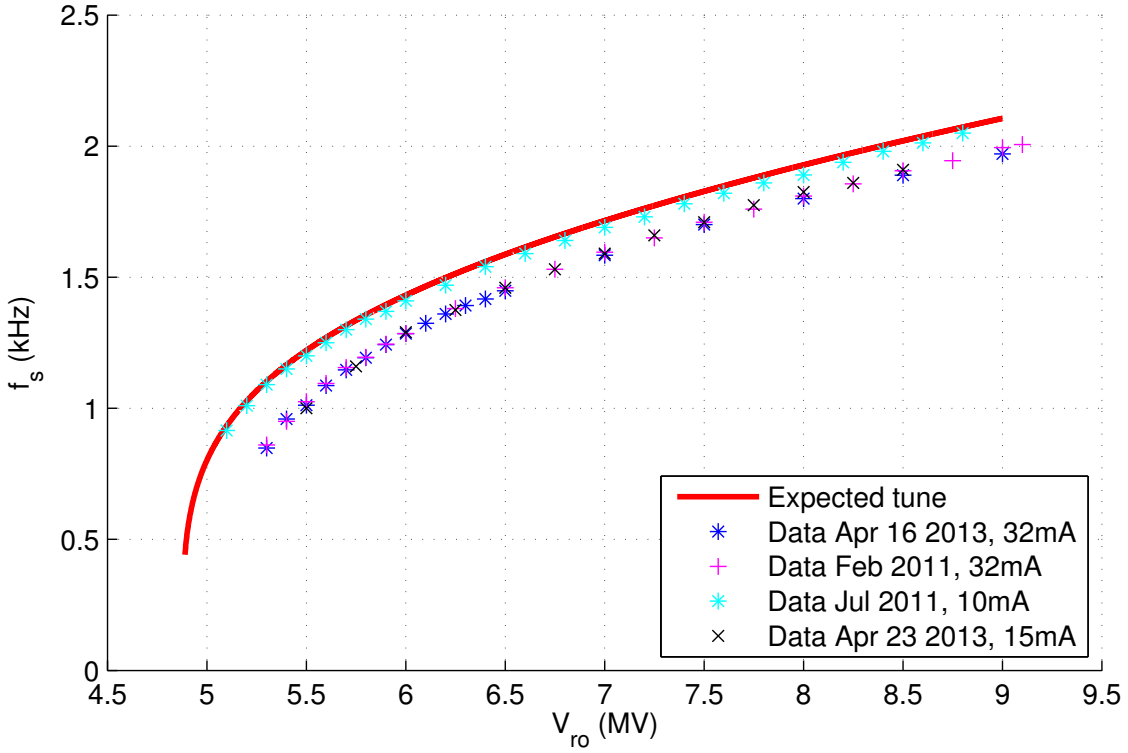

Figure 3.1: Synchrotron oscillations frequency versus readout value of RF voltage. The expected value, red line, is compared with four different measurements done in 2011 and 2013, with different total currents and filling patterns.

The fit of the measurements taken in April 16 2013, compared with the expected values, is shown in figure 3.2.

In table 3.1 the results of the fit for all the measurements of 2011 and 2013 are shown, together with the total current and the number of bunches.

The fit gives a momentum compaction factor not compatible with the one of the perfect machine model, that is $\alpha = 1.78\,10^{-4}$ (table 1.2), but smaller.

From measurement of July 2011, the calibration factor obtained from the fit is compatible with 1, but for all other measurements it is not. The measurements of July 2011 have been performed at very low current (10 mA) and the calibration could be different in that regime, due to the very low cavity beam-loading.

In April 23 2013, a measurement with very low current has been tried again, but the minimum value of the current, in order to read a signal of the synchrotron tune, was 15 mA.

The momentum compaction factor can be different with respect to the perfect machine one, because it depends on the bending angles, including the ones from the quadrupole misalignments and the orbit correctors. The orbit correction has been

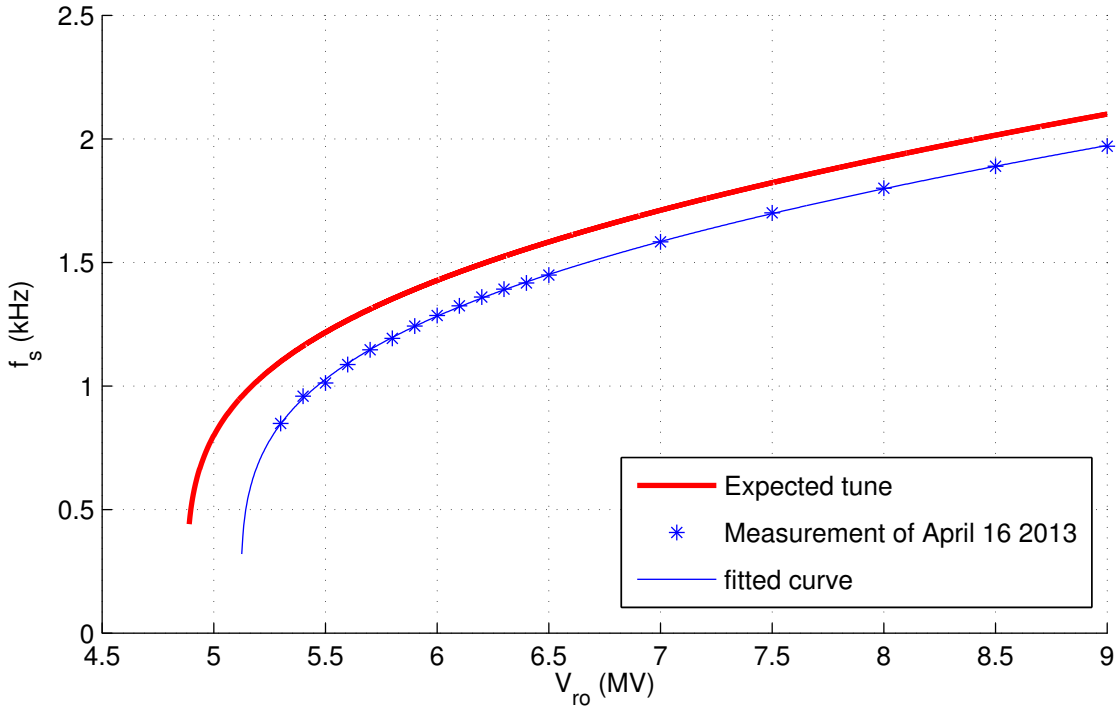

Figure 3.2: Synchrotron oscillations frequency versus read out value of the RF voltage, measured in April 16 2013, compared with the expected value. The blue line is a fit, with α and k as free parameters.

computed before all the measurements and therefore it was different in different measurements.

The ESRF lattice error model includes the gradient errors and the tilt of quadrupole and dipole magnets and it is obtained fitting the measurement of the response matrix. These errors can predict the horizontal and vertical β-beating, i.e. the variation of the β function with respect of the nominal ones, the horizontal and vertical dispersion and the coupling between horizontal and vertical motion. The error model assumes the orbit to be exact.

The momentum compaction factor predicted by the ESRF error model is larger than the nominal one, that can be computed from the perfect machine model, of about $3 - 5\%$.

Random misalignments of quadrupoles and sextupoles have been simulated, in order to understand the smaller momentum compaction factor obtained from the synchrotron tune measurements.

Some different random misalignments in quadrupole and sextupoles have been added to the perfect machine, an orbit correction has been performed, using the horizontal and vertical orbit correctors, using the Accelerator Toolbox of Matlab

Table 3.1: synchrotron tune measurements for RF voltage calibration of 2011 and 2013.

Date	I_{tot} (mA)	N_b	k	$\alpha(10^{-4})$
February 2011	32	661	0.949 ± 0.005	1.712 ± 0.009
July 2011	10	661	0.998 ± 0.009	1.74 ± 0.01
April 16 2013	32	992	0.953 ± 0.005	1.674 ± 0.007
April 23 2013	15	992	0.942 ± 0.016	1.75 ± 0.02

[27]. The momentum compaction factor has been computed for 50 different seeds of random misalignments. In figure 3.3, the 50 momentum compaction factors computed for different random misalignments are shown and compared with the value of the perfect machine. This kind of error model gives a lower momentum compaction factor than the perfect machine one, but still larger than the one obtained from the synchrotron tune measurements.

The root mean square value of the misalignments distributions is 50 μm in horizontal and vertical, for both quadrupoles and sextupoles.

A measurement of the momentum compaction factor could help to understand the RF calibration. In the appendix C, two possible momentum compaction factor measurements are described.

Synchronous phase measurement

Using the bunch by bunch feedback, the measurement of the phase between the beam and the master clock is possible. In April 16 2013, this measurement has been performed.

The synchronous phase is defined as the phase between the beam and the signal into the cavity. It can be used to measure the RF voltage calibration factor, because it depends on the RF voltage as follows:

$$\phi_s = \pi - \arcsin\left(\frac{U_0}{eV_{RF}}\right) \tag{3.16}$$

The measurement has been done with all gaps opened, in order to have a known energy loss per turn.

The measured phase differs from the synchronous phase of a constant value and it is defined with an opposite sign. The measurements are fitted with function 3.17, with two degrees of freedom: an additive phase ϕ_0 and the RF voltage calibration factor k.

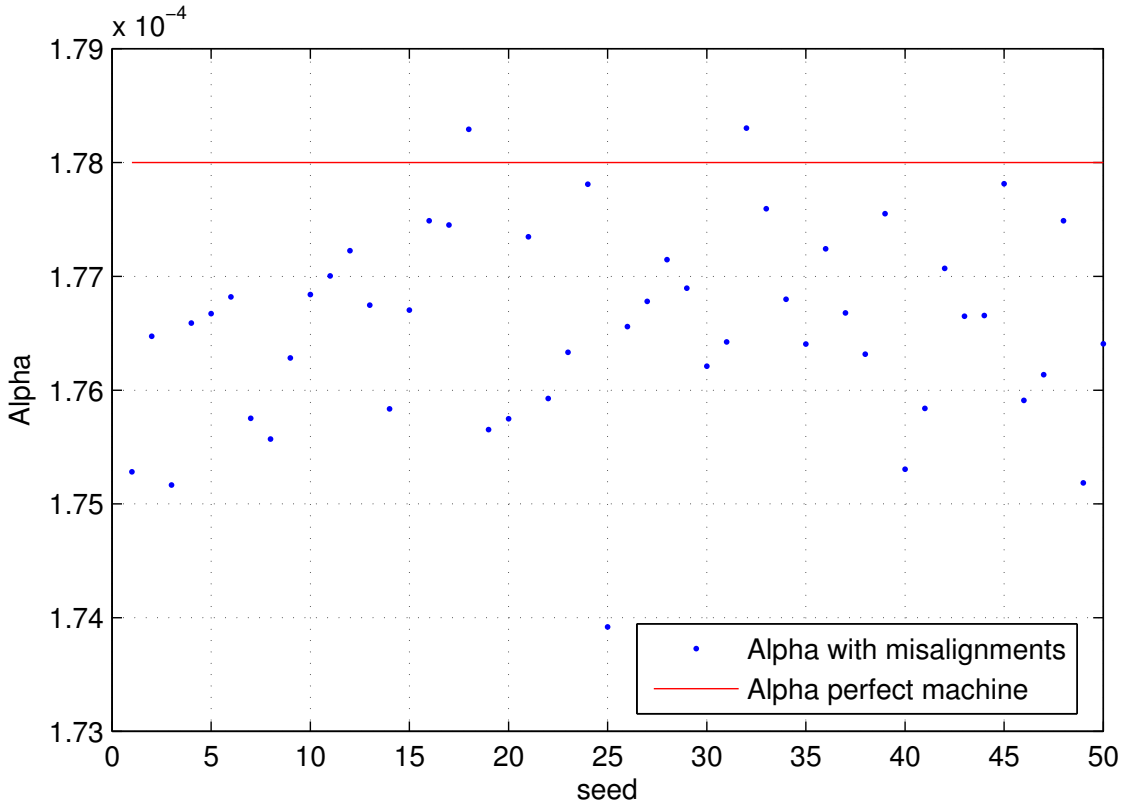

Figure 3.3: Momentum compaction factors for 50 different set of misalignment errors in quadrupoles and sextupoles. The red line shows the value of the momentum compaction factor of the perfect machine.

$$\phi = \phi_0 + \arcsin\left(\frac{U_0}{ekV_{ro}}\right) \tag{3.17}$$

The results of the fit are:

$$\phi_0 = (61.0 \pm 0.4)^\circ \tag{3.18}$$

$$k = 0.949 \pm 0.007 \tag{3.19}$$

The calibration factor is compatible with the one obtained from the synchrotron tune measurements, assuming the nominal beam energy.

A different method for the phase measurement, using the beam position monitor data, has been recently developed at ESRF [28] and it can be also used to measure the RF voltage calibration factor.

The measured phase differs from the synchronous phase of a constant value. The measurements are fitted with function of equation 3.20, with two degrees of freedom: an additive phase ϕ_0 and the RF voltage calibration factor k.

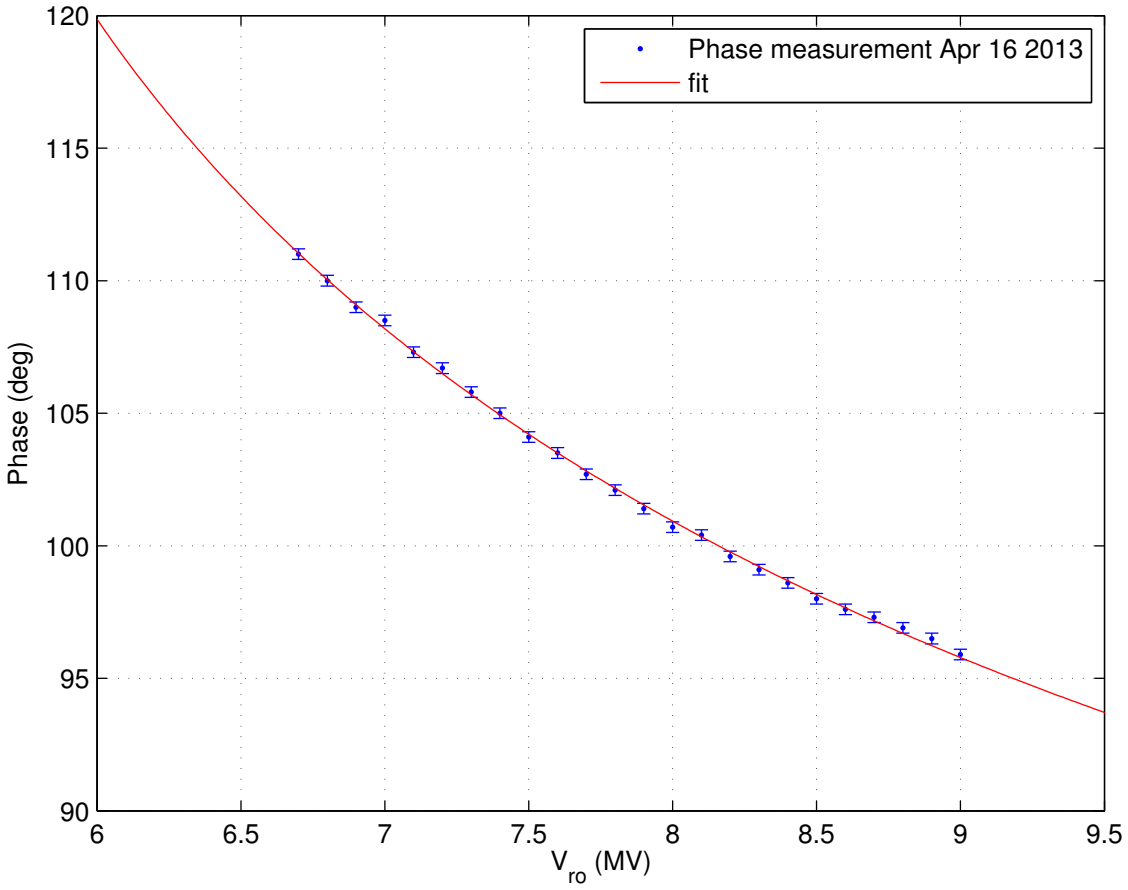

Figure 3.4: Measurement of phase between the beam and the master clock, fitted with function 3.17, with two free parameters: an additive phase and the RF voltage calibration factor.

$$\phi = \phi_0 - \arcsin\left(\frac{U_0}{ekV_{ro}}\right) \tag{3.20}$$

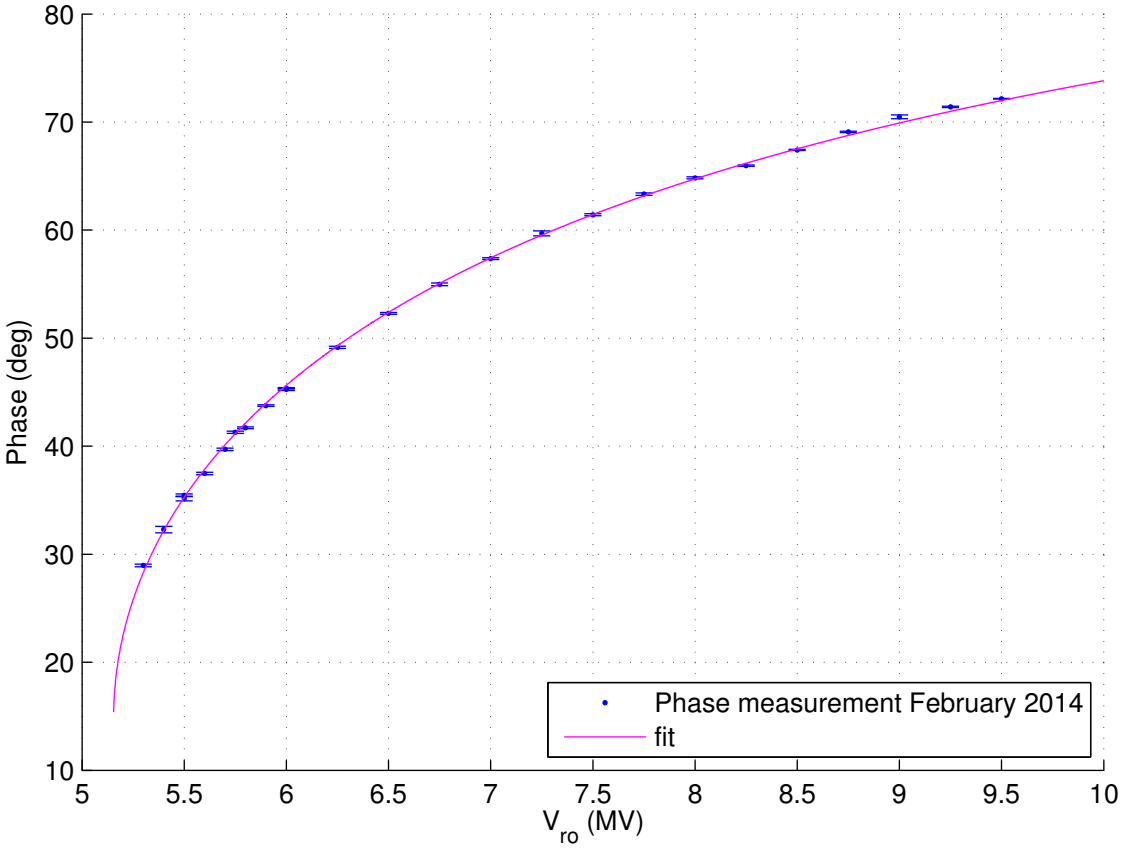

Figure 3.5: Measurement of phase between the beam and the master clock, measured using BPM signals on February 2013. Measurements are fitted with function 3.20, with two free parameters: an additive phase and the RF voltage calibration factor.

The results of the fit are:

$$\phi_0 = (104.9 \pm 0.3)^\circ \tag{3.21}$$

$$k = 0.947 \pm 0.004 \tag{3.22}$$

From the synchrotron tune and synchronous phase measurements, we can derive the RF voltage calibration factor:

$$k = 0.949 \pm 0.003 \tag{3.23}$$

3.2 Bunch length

Current dependent bunch lengthening effect has been observed and measured at ESRF [29] [30]. This effect is due to longitudinal impedance, via the potential well effect, as described in section A.3.1.

Bunch length as a function of bunch current and RF voltage has been measured in 2011 with a streak camera.

An example of an image from the ESRF streak camera is shown in figure 3.6. From this image, the rms bunch length can be obtained.

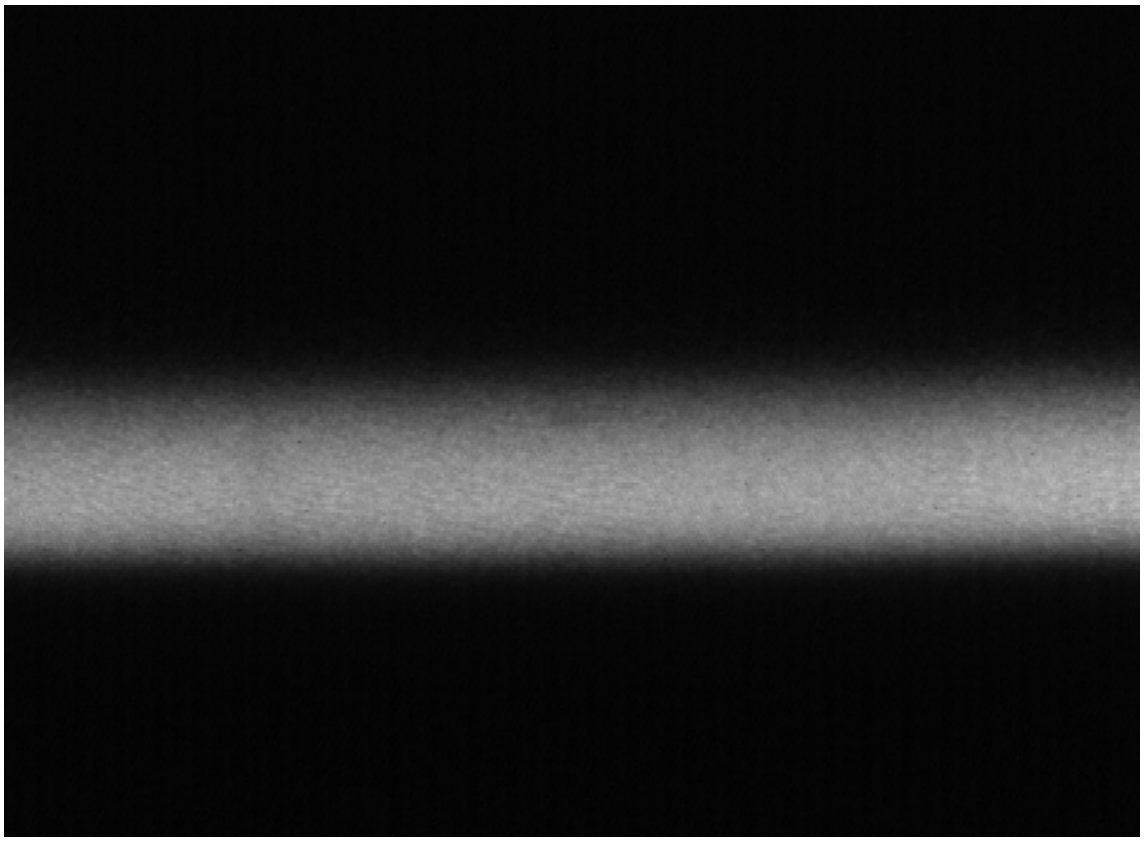

Figure 3.6: Streak camera picture of the synchrotron radiation. The time is the vertical direction.

In figure 3.7 the density profile of the electron bunch, with four different beam settings, is shown.

In 2011, some bunch length measurements with different bunch currents (from 0.012 mA to 5.8 mA) and with two different RF voltages (6.0 MV and 8.0 MV, read-out values) have been performed.

An analysis of those measurements has been done in order to have a simple model to know the bunch length as a function of bunch current and RF voltage.

In previous analyses of the bunch length data, the standard deviation of the

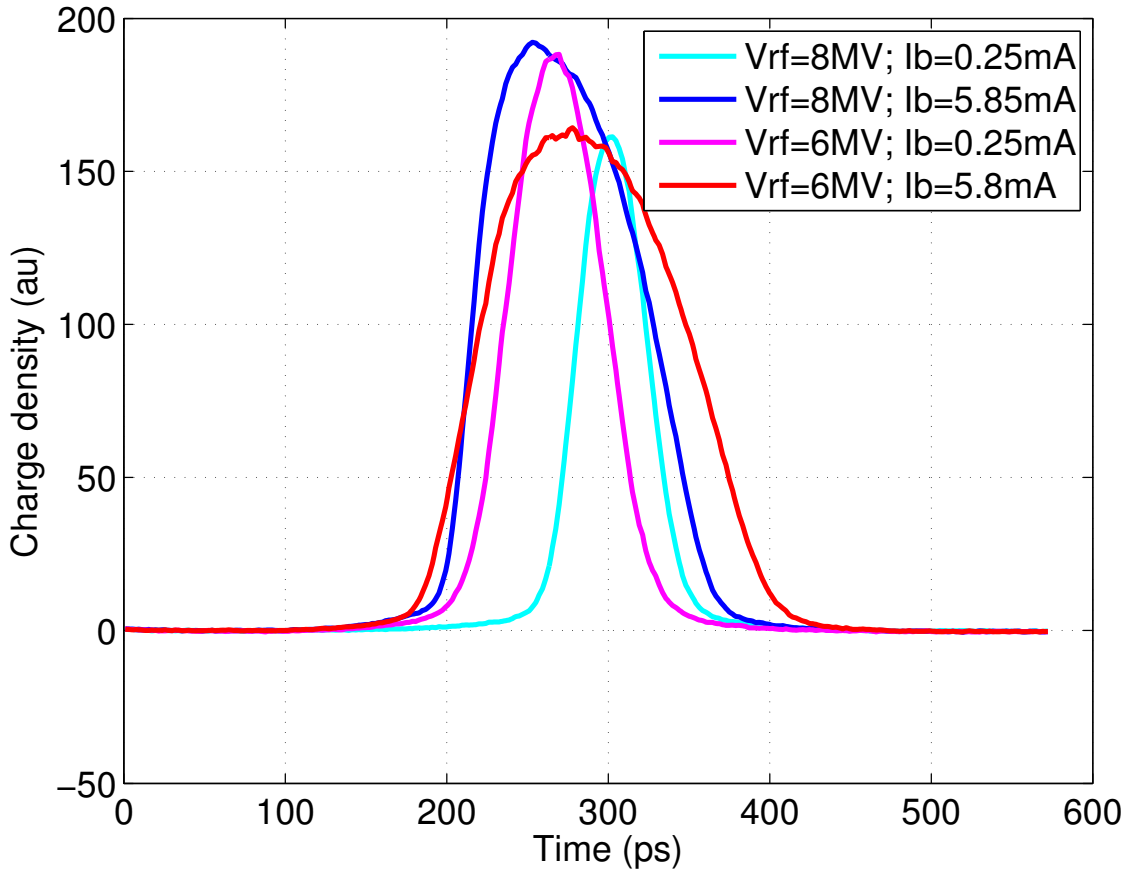

Figure 3.7: Bunch time structure for four different beam settings.

distribution was computed assuming a gaussian distribution and computing the rms from the full width half maximum value, using the relation:

$$FWHM = 2\sqrt{-2\ln\frac{1}{2}}\,\sigma \tag{3.24}$$

where $FWHM$ is the full width half maximum and σ is the standard deviation of the gaussian distribution.

This assumption is correct when the current is low, but when current is too large the bunch is not gaussian but asymmetric, as we can see from the bunch profiles of figure 3.7, and the equation 3.24 is no longer valid.

In order to compute the standard deviation of the bunch density, the tails of the distribution have been removed, because at large distance from the mean the noise can affect the standard deviation computation disproportionately.

The current dependent bunch lengthening effect can be computed solving the Haissinski equation (see appendix A, section A.3.1), for example with the `haissinski` module of `elegant`, or using the approximated formula of equation 3.6. For a purely

inductive impedance, the two result are very similar.

The RF voltage calibration factor from the synchrotron tune measurements has been used for this study ($k = 0.95$).

The bunch length measurements are shown in figure 3.8. With a purely inductive impedance $Z_n = 0.7\,\Omega$, the computed bunch lengthening match quite well both sets of measurements, at 6.0 MV and 8.0 MV, readout values.

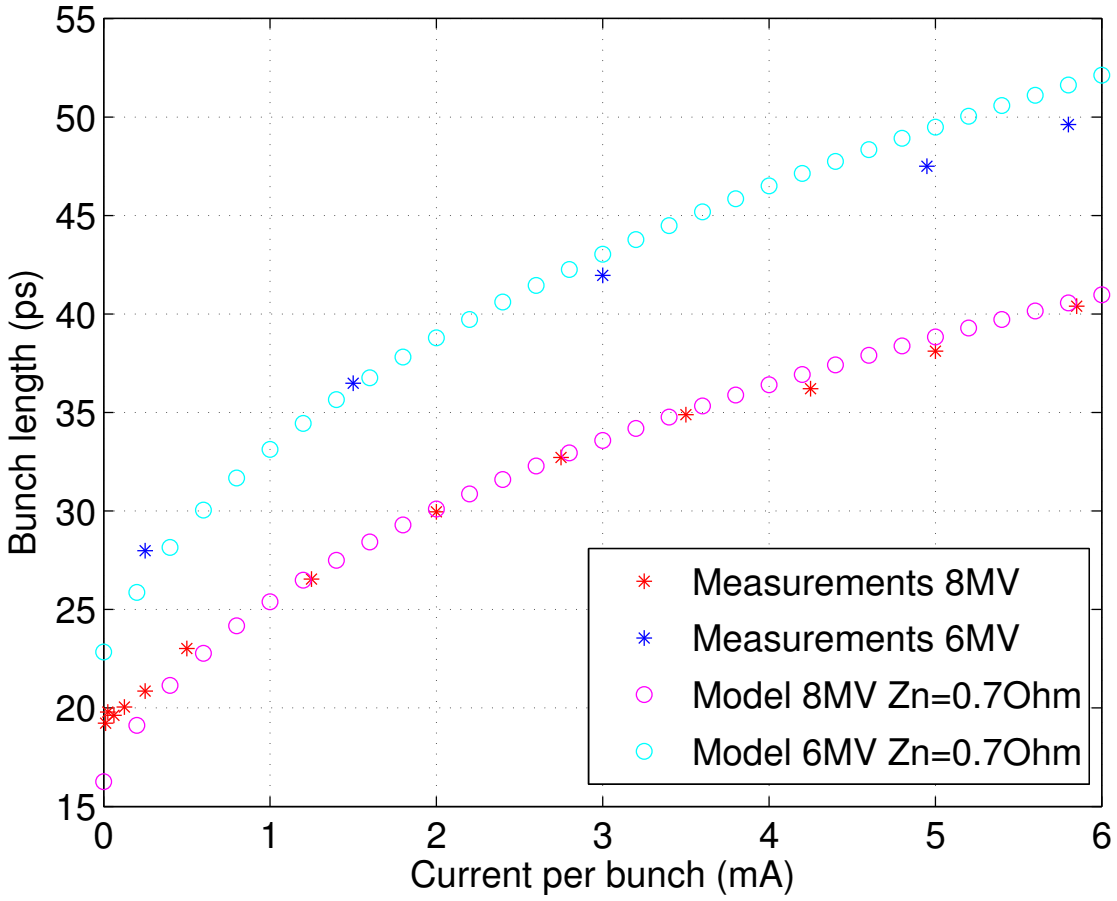

Figure 3.8: Bunch length measurements and model, assuming a purely inductive impedance, computed with formula of equation 3.6, for different currents and RF voltages. For both the measurements and the model, the RF voltage is assumed to be the readout value.

3.3 Momentum acceptance simulation

Touschek lifetime can be computed with the Piwinski formula, equation (2.9), using the program `touschekLifetime`, distributed with `elegant` [31].

The momentum acceptance is needed in both the Piwinski and Bruck formulas

and it can be computed with a 6-D particle tracking code like `elegant`, AT [27] or MAD-X [32].

Two functions, $\delta_p(s)$ and $\delta_n(s)$, represent the maximum positive and negative momentum displacement at a position s around the ring. The function *momentum_aperture* of `elegant` allows to compute those two quantities around the ring, in any position chosen by the user. The method used is described in [33]. Essentially, for each chosen longitudinal position, an on axis particle, with a momentum displacement δ, is tracked for a given number of turns. If the particle is not lost for all the turns, δ is increased. The function initially uses large steps of δ, to find approximate boundary. Then, a fine search of the boundary between the values of δ where the particles are lost and the values where the particles are stable is performed.

$\delta_p(s)$ and $\delta_n(s)$ are generally different and they must be independently computed. The closed orbit of particles with positive or negative energy displacements are not symmetric, due to the nonlinear dispersion.

In figure 3.9, the closed orbit for some positive and negative momentum displacements in two ESRF cells, computed with `elegant`, are shown. The closed orbit with negative values of δ is larger than the one with positive values of δ.

Longitudinal motion

The longitudinal motion may have a significant effect in the simulation of the momentum acceptance [34]. If the synchrotron radiation is on, at least one cavity must be defined in the lattice, in order to provide the energy loss per turn. In this case, we include the effects of radiation damping and synchrotron oscillations. Note that we do not consider quantum fluctuations from the radiation.

In figure 3.10, the oscillations and damping of the energy in the ESRF storage ring are shown for four electrons with different initial energy. The synchrotron period is about 200 turns and the longitudinal damping period is about 1200 turns.

In figures 3.11 and 3.12, the momentum acceptance computed in two cells of the ESRF lattice is shown for some different numbers of turns: in figure 3.11 the synchrotron radiation was turned off and the cavities were switched off; in figure 3.12 the synchrotron radiation was on and there were two RF cavities in the lattice that provide the energy lost.

As we can see from the figures, a too small number of turns gives an higher momentum acceptance and therefore an overestimation of the Touschek lifetime.

From figure 3.12, we can see that the difference in momentum acceptance between 512 turns and 2048 turns are quite small. 512 turns are used for all momentum acceptance simulations in this thesis.

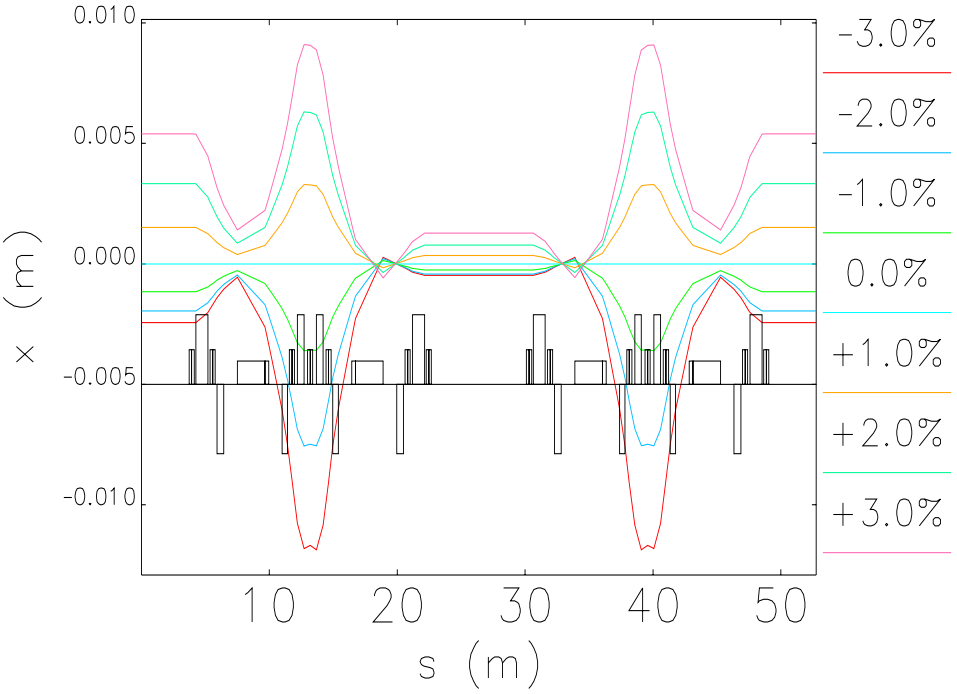

Figure 3.9: Closed orbit in the ESRF storage ring for 7 different electron momentum displacements. The asymmetry is due to the nonlinear dispersion.

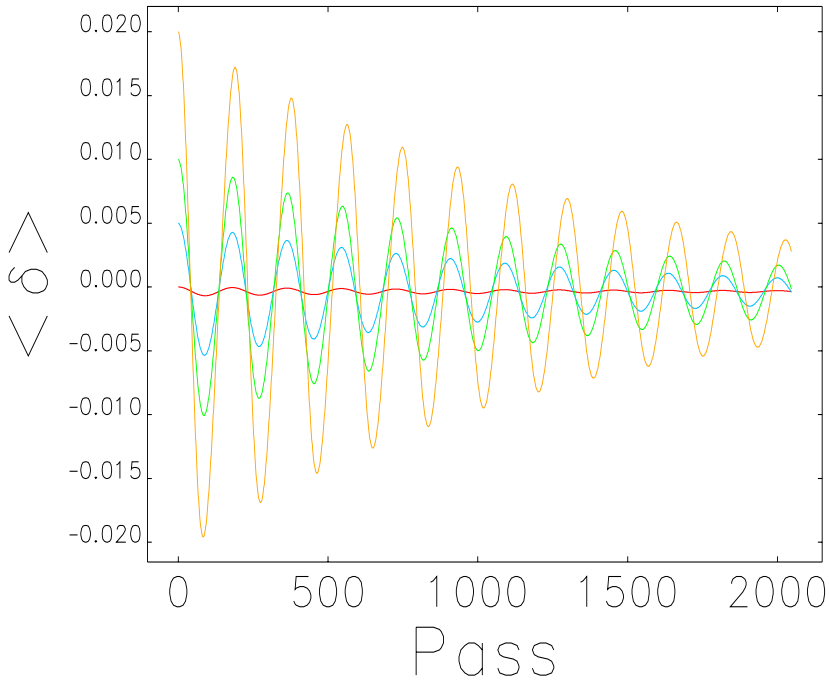

Figure 3.10: Momentum deviation versus number of turns, for four different electrons with different starting δ value: 0, 0.005, 0.01 and 0.02.

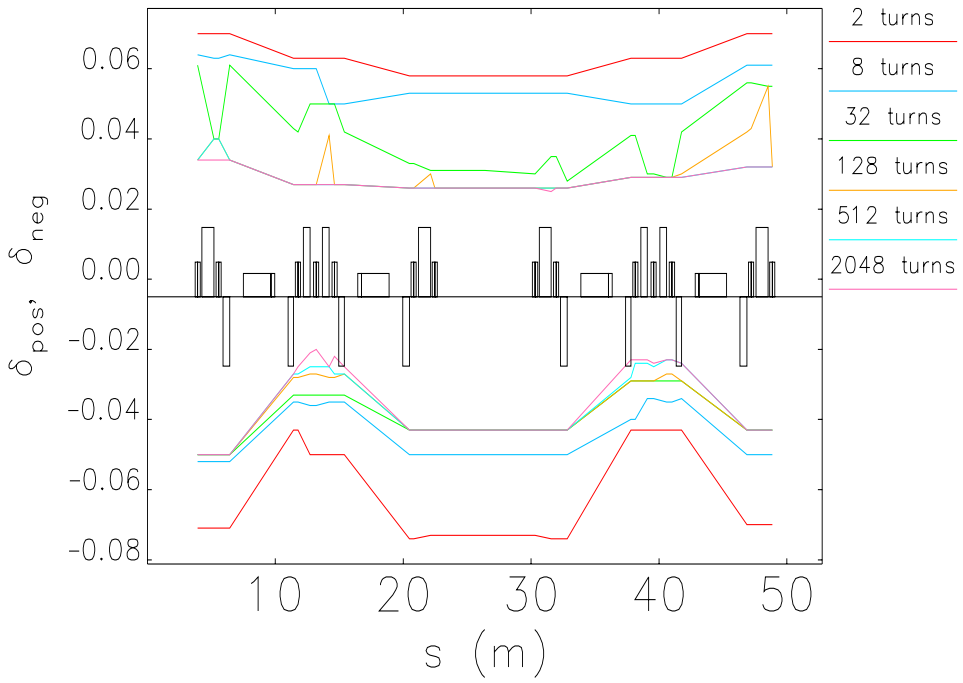

Figure 3.11: Momentum acceptance computed in two cells of the ESRF lattice with some different numbers of turns. Without synchrotron motion.

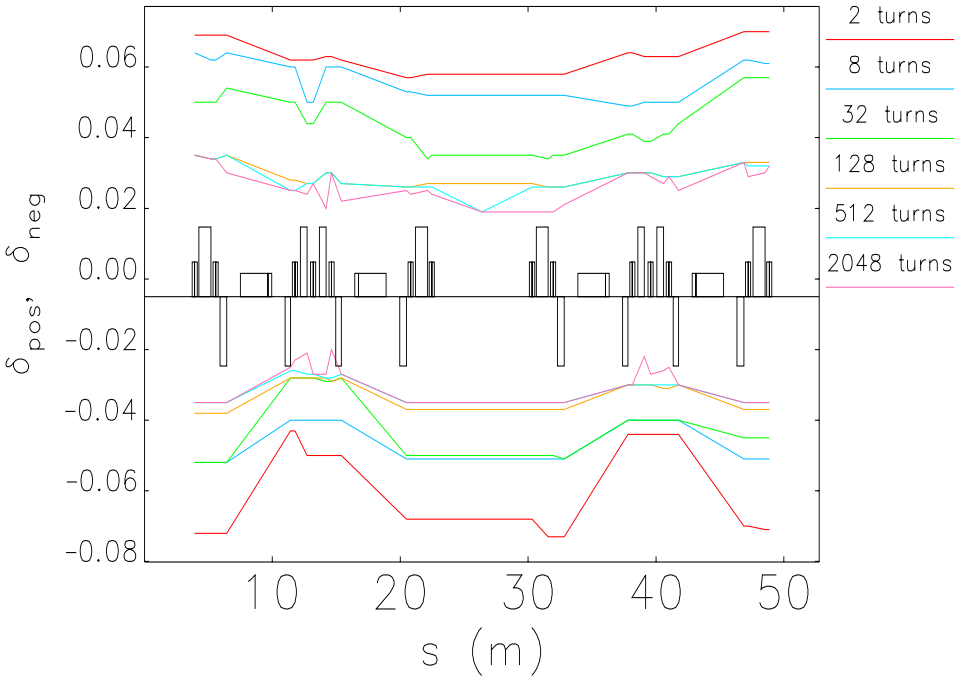

Figure 3.12: Momentum acceptance computed in two cells of the ESRF lattice with some different numbers of turns. With synchrotron motion and synchrotron radiation.

Physical apertures

In the storage ring model, the physical apertures can be defined. The physical aperture in a position of the ring is the size of the vacuum chamber. During the tracking, a particle is considered lost if one of the horizontal or vertical coordinates is larger than the size of the vacuum chamber in that position.

In figure 3.13, the physical apertures of the ESRF storage ring are shown as a function of the longitudinal coordinate along one cell.

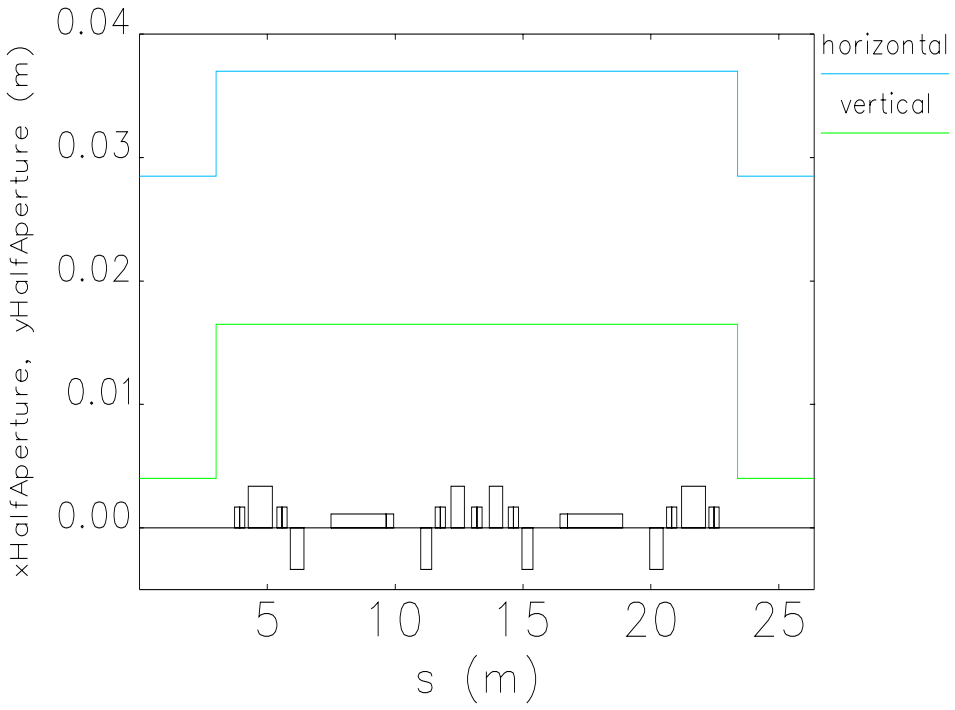

Figure 3.13: Horizontal and vertical semi-axis of the ESRF elliptical vacuum chamber as a function of the position in one cell.

Some other positions of the ring have smaller physical apertures: the injection septum, in the straight section of cell 4, and the absorbers of second dipoles of cell 16 and 30.

The septum is located in the internal side of the ring. The distance between the septum and the beam is 19.52 mm. The two absorbers are close to the dipoles, in the external side of the ring. The external radius of the beam pipe near these absorbers is 19 mm.

Adding the physical apertures to the lattice, the momentum acceptance become smaller and therefore the Touschek lifetime become shorter. In figure 3.14, the

momentum acceptance of the ESRF lattice is shown with and without the physical apertures. The momentum acceptance is computed with `elegant`, with 512 turns, including longitudinal motion and synchrotron radiation.

In figure 3.15, the Touschek scattering rate of the ESRF lattice is shown, with and without the physical apertures. The scattering rate is the number of particles lost due to Touschek scattering per unit of time in a certain position of the ring and it depends on the local beam size and on the local momentum aperture. We note that it is sharply peaked in the region with small β_x and β_y, i.e. in the low beta straight sections. Since most of the scattering occurs at this regions, the momentum acceptance is most significant at this positions.

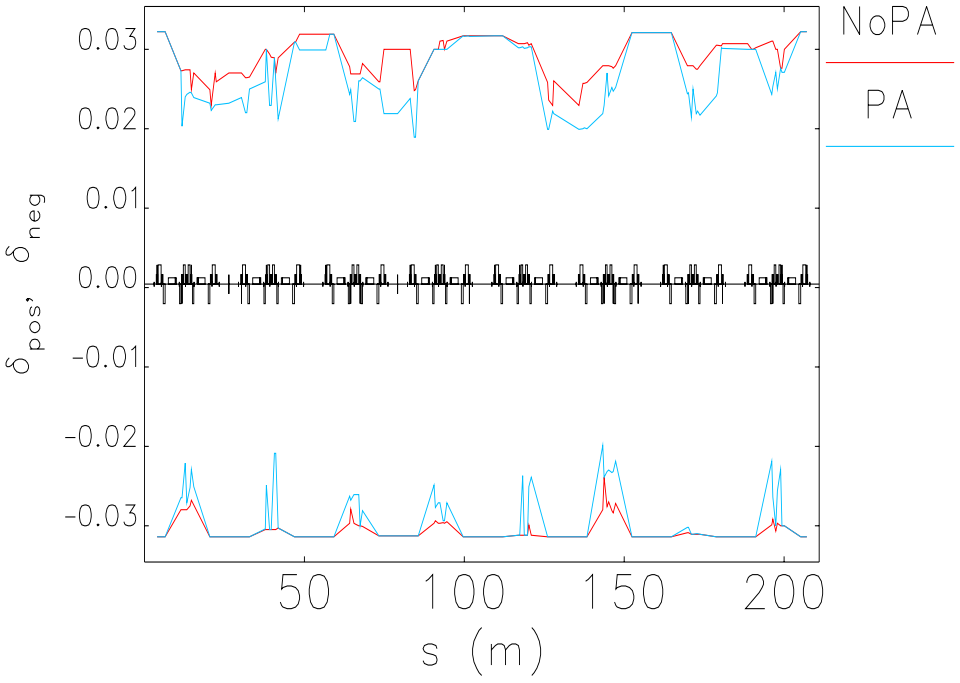

Figure 3.14: Momentum aperture of the ESRF multi-bunch lattice computed in 8 cells, with physical apertures (blue lines) and without physical apertures (red lines).

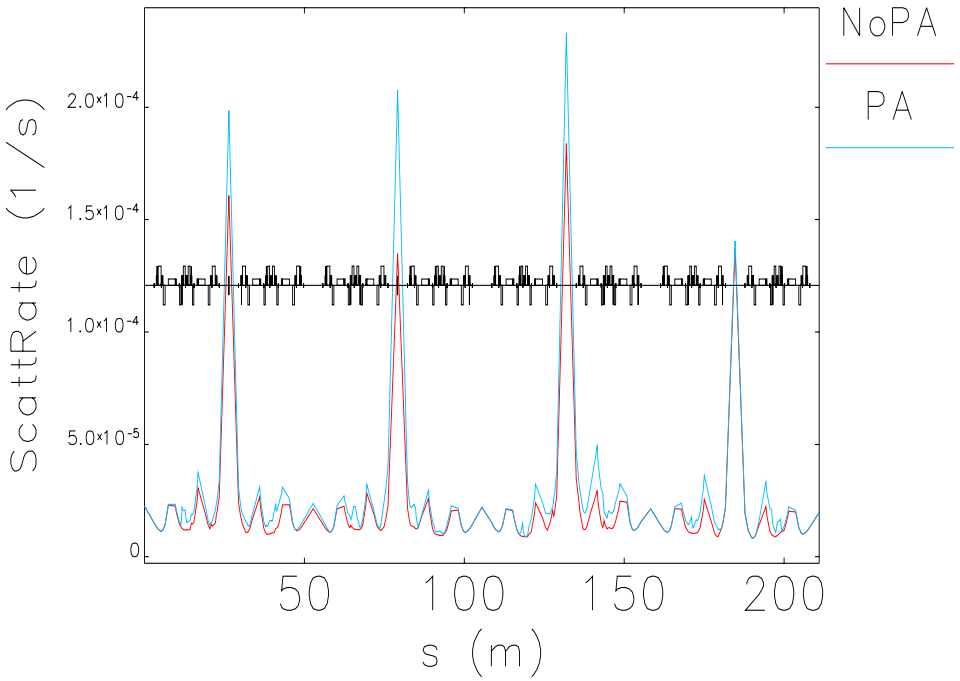

Figure 3.15: Inverse of Touschek lifetime of the ESRF lattice computed in 8 cells, with physical apertures (blue line) and without physical apertures (red line).

Additional physical limitations can be added to the model, in order to simulate the presence of the scrapers. The scrapers are defined in `elegant` as rectangular collimators, where the sizes of the rectangle can be independently defined.

In figure 3.16, the momentum acceptance for different value of the internal scraper position, computed with `elegant`, is shown.

An experiment was performed to measure the Touschek lifetime versus scraper position. The results, described in chapter 5, indicate that the modeling of apertures and their effect on momentum acceptance are quite accurate.

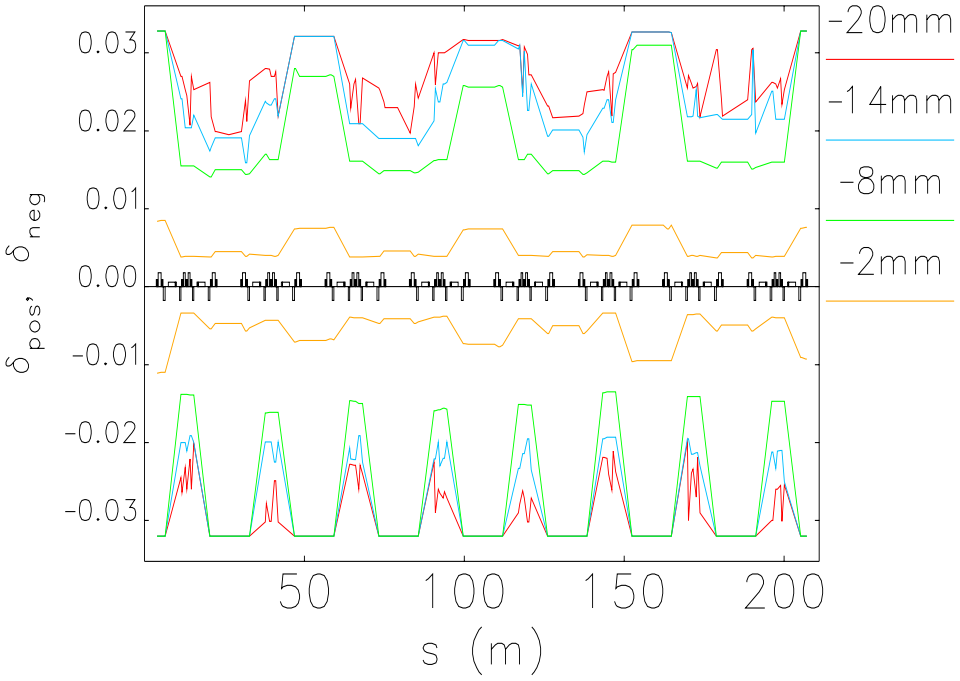

Figure 3.16: Momentum acceptance in 8 cells of ESRF storage ring, with different values of internal scraper position.

Errors

A good model of the machine, with field errors to reproduce β-beating, horizontal and vertical dispersion and coupling is needed to have a good prediction of Touschek lifetime.

The β-beating is the variation on the β functions of the real machine with respect to the ones of the perfect machine and it is defined as:

$$\beta_{beat}(s) = \frac{\beta_{em}(s) - \beta_{pm}(s)}{\beta_{pm}(s)} \tag{3.25}$$

where $\beta_{em}(s)$ is the β function (horizontal or vertical) of the machine with errors and $\beta_{pm}(s)$ is the β function of the perfect machine.

At ESRF, an error model is obtained from the measurement of the response matrix and from the measurement of the horizontal and vertical dispersion. The error model is used to compute the normal and skew quadrupole corrections.

In figure 3.17, the β-beating obtained from the model of the ESRF lattice with errors, measured on July 02 2013, is shown, together with the vertical dispersion.

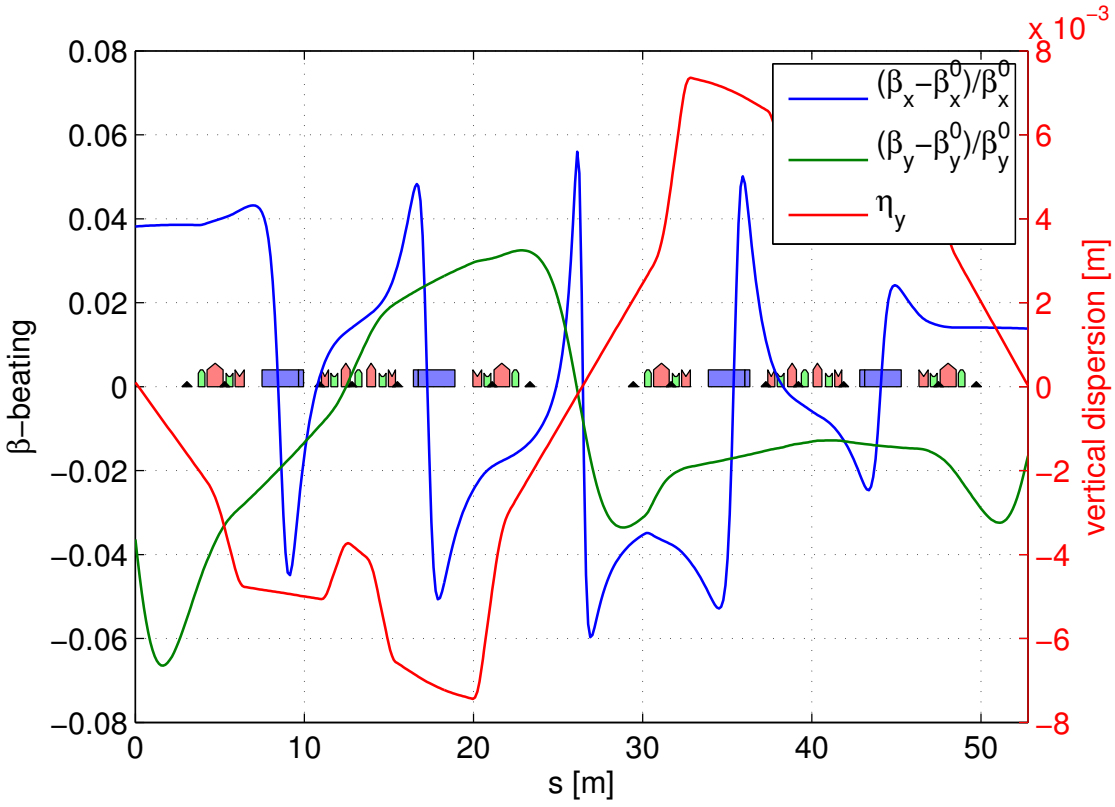

Figure 3.17: Horizontal and vertical β-beating and vertical dispersion of the ESRF lattice with errors measured on July 02 2013.

In figure 3.18, the momentum acceptances for the perfect lattice and for the lattice with errors are compared. For the lattice with errors, the momentum acceptance is smaller.

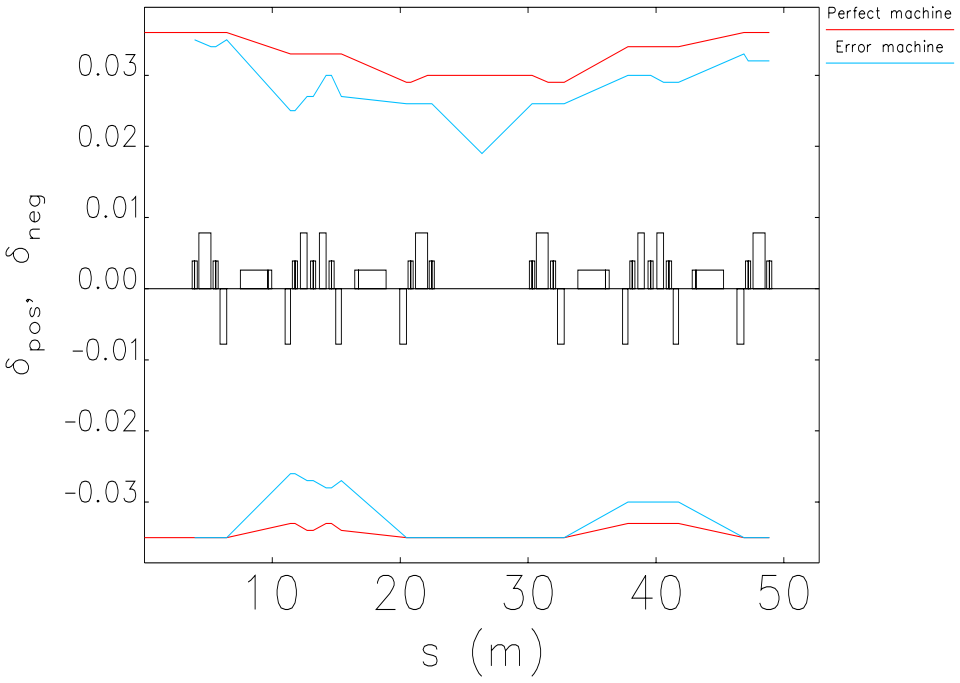

Figure 3.18: Momentum acceptance in 2 cells of ESRF storage ring, for the perfect machine (in red) and for the machine with quadrupole gradient errors, dipole field errors, quadrupole tilts and dipole tilts, corrected with quadrupole and skew quadrupole correctors.

RF voltage

The momentum acceptance is limited by two effects: the longitudinal bucket size, which is related to the accelerating voltage, and the dynamic momentum aperture.

The longitudinal bucket size, or RF acceptance, is given by:

$$\delta_{RF} = \frac{2\nu_s}{h\alpha}\sqrt{1 - \left(\frac{\pi}{2} - \phi_s\right)\tan(\phi_s)} \tag{3.26}$$

where ν_s is the synchrotron tune, h is the cavity harmonic number, α is the momentum compaction factor and ϕ_s is the synchronous phase, defined in equation (A.82).

In figure 3.19, the RF acceptance of equation (3.10) is shown as a function of the RF voltage, for the ESRF storage ring.

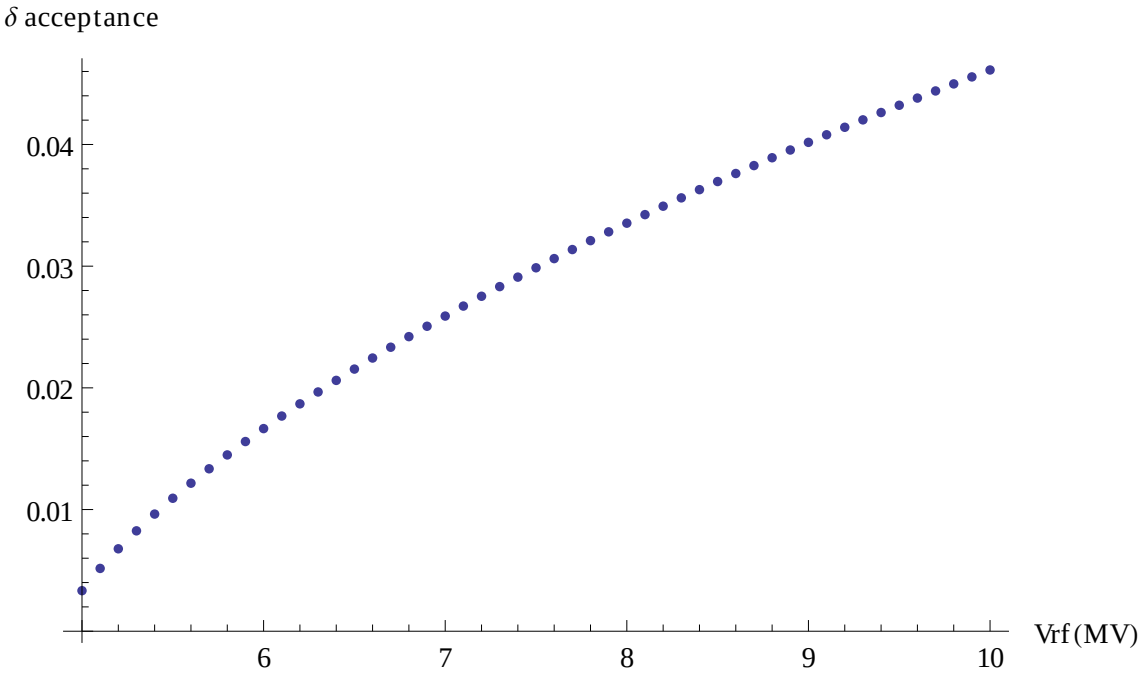

Figure 3.19: RF acceptance as a function of RF voltage for the ESRF storage ring.

In figure 3.20, the simulated momentum acceptance with different RF-voltage is shown. The simulation is done with `elegant`, including synchrotron radiation.

For low RF-voltage, the momentum acceptance is limited by the size of the longitudinal bucket and it is defined by the value of the voltage; for higher RF voltage, the momentum acceptance is limited by the dynamic acceptance, defined by the nonlinear dynamics.

The RF-acceptance obtained from the tracking is slightly different from the one of equation 3.26. In particular, it is asymmetric, because the bucket itself it asymmetric.

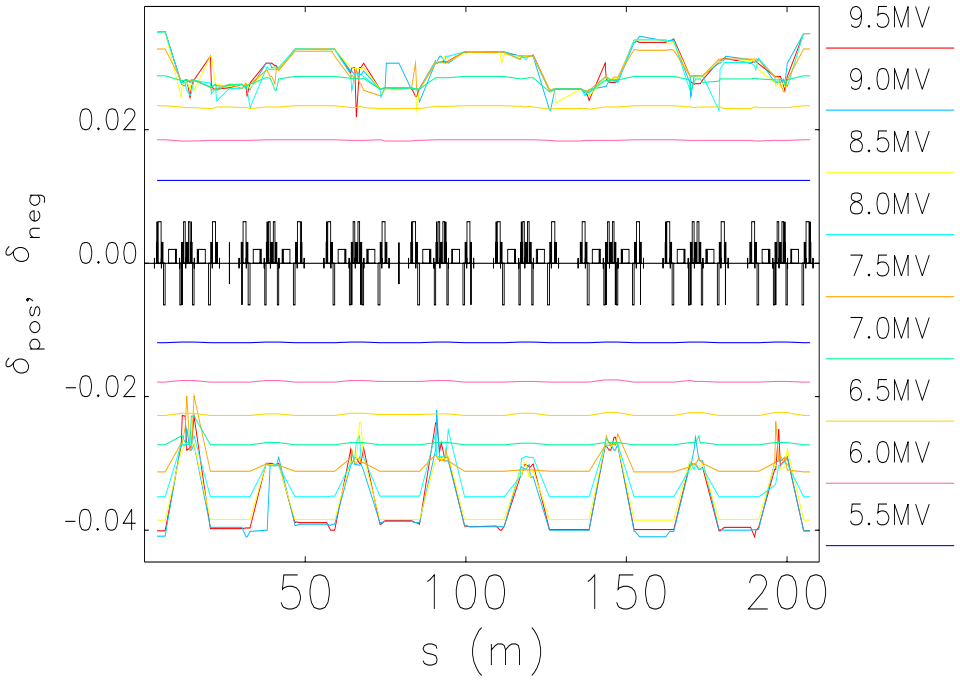

Figure 3.20: Momentum acceptance computed in 8 cells of the ESRF storage ring for different RF-voltage, from 5.5 MV and 9.5 MV.

Chapter 4

Lifetime measurements

The signal from the beam position monitors is proportional to the beam current and can be used for a current measurement. The variation of current is used for the lifetime measurement.

In the ESRF storage ring there are 7 beam position monitors per cell, i.e. 224 in all the ring.

A series of Touschek lifetime measurements were carried out during machine dedicated time (MDT) shifts in 2013. In this chapter, the results of these measurements are described.

Using the theory and measurements described in preceding chapters, we can compare the measured lifetime to the expected value, given the beam conditions. We find that the careful work modeling the momentum acceptance pays off, since we are able to predict the correct lifetime for a range of beam parameters.

In the first section, the measurement of the vacuum lifetime is shown. The vacuum lifetime must be measured every time we want a Touschek lifetime measurement. In the second section, the measurement of the effects of the spin polarization on the Touschek lifetime are shown. In the third section, the measurements of the Touschek lifetime at different RF-voltages are shown. In the fourth section, the measurements of Touschek lifetime with different physical apertures are shown.

4.1 Vacuum lifetime

The vacuum lifetime depends on the scattering of the electron with residual gas molecules in the beam pipe. The scattering rate depends on the residual pressure inside the beam pipe [35].

Vacuum lifetime measurement can be done by increasing the Touschek lifetime, without changing the gas scattering rate, i.e. without changing the total current.

The gas scattering rate does not depend on the beam emittance, therefore a simple method to measure the vacuum lifetime is to measure the total beam lifetime for many different vertical emittances.

From equation (3.1), we see that the inverse of Touschek lifetime is proportional to the inverse of square root of vertical emittance:

$$\frac{1}{\tau_t} = K\frac{1}{\sqrt{\varepsilon_y}} \tag{4.1}$$

where K is the proportionality factor. The total lifetime as a function of the vertical emittance can be written:

$$\frac{1}{\tau}(\varepsilon_y) = K\frac{1}{\sqrt{\varepsilon_y}} + \frac{1}{\tau_v} \tag{4.2}$$

The total lifetime can be measured for many different values of vertical emittance, without changing other parameters, and the vacuum lifetime can be obtained from a linear fit between $1/\tau$ and $1/\sqrt{\varepsilon_y}$.

At ESRF, the vertical emittance can be easily increased using a white noise vertical shaker, where the range of frequency includes the vertical betatron oscillation frequency. This method does not change the coupling between horizontal and vertical motion and it does not change horizontal emittance. Vertical emittance can be varied within a large range of values, from a minimum of $\varepsilon_y \simeq 4\,\text{pm}$ up to a few nm.

A measurement of the vacuum lifetime, for three different bunch currents and filling modes, in order to have the same total current of 32 mA, is reported in figure 4.1. The results of the measurements are reported in table 4.1.

Table 4.1: vacuum lifetime measurements for three different bunch currents.

I_b (mA)	I_{tot} (mA)	N_b	τ_v(h)
2.0	32	16	900 ± 200
1.0	32	32	700 ± 100
0.037	32	868	770 ± 90

Vacuum lifetime depends on total beam current, but it does not depend on bunch current, so we perform all measurements on a given day with the same total current, even for different filling patterns.

The vacuum lifetime measurement is done before all lifetime measurements, so that the Touschek lifetime may be inferred from the total lifetime.

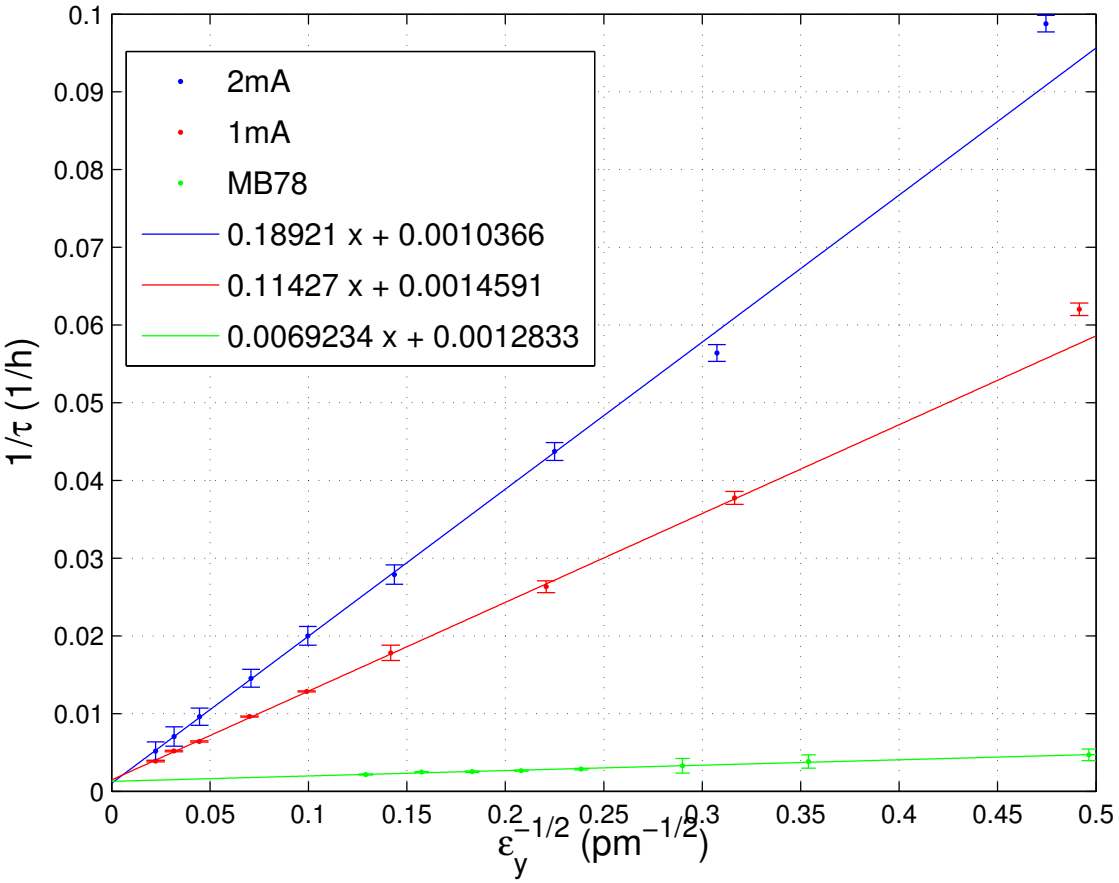

Figure 4.1: Inverse beam lifetime versus inverse square root of vertical emittance for three different bunch currents. Measurements of April 2 2013.

4.2 Spin polarization time

As described in section 2.1, the Touschek lifetime depends on the spin polarization.

The polarization follows an exponential law, equation (2.26):

$$P(t) = P_{ST}\left(1 - e^{-t/\tau_p}\right) \tag{4.3}$$

and the Touschek lifetime depends on the polarization value S, equation (2.38)

$$\frac{1}{\tau_t(P)} = \frac{1}{\tau_t(0)} + \left\langle R(\epsilon)\frac{1}{\tau_t(0)} \right\rangle P^2 \tag{4.4}$$

where $R(\epsilon)$ is defined in equation 2.39, P is the vertical spin polarization, τ_t is the Touschek lifetime.

A procedure able to depolarize completely the beam has been defined using the considerations in section 2.1.

Using a kicker with frequency scanned from 249 kHz to 253 kHz in 40 s, with 10 ms steps, powered with a voltage of 0.5 V, the beam is completely unpolarized[1].

The complete depolarization has been proved experimentally: if the procedure is applied twice, after the second time the lifetime doesn't change.

In order to verify the polarization time and the effect of the polarization on the Touschek lifetime, a long measurement has been done in November 2013.

The beam has been injected with 16 bunches and 2 mA per bunch. The vacuum lifetime has been measured. After a complete depolarization procedure, the lifetime has been measured every 30 s for 67 min. For each lifetime measurement, also the beam current has been measured.

In figure 4.2, the decay of the current during the measurement is shown.

The Touschek lifetime with 16 bunches of 2 mA and a vertical emittance of 5 pm is about 12 h, so the lifetime is dominated by the Touschek effect, because the vacuum lifetime has been measured and it was more than 600 h.

As we can see from figure 4.2, the total beam current changed during the measurement from a starting value of about 31 mA to about 28.4 mA.

During the measurement, the Touschek lifetime changes due to three effects: the current reduction, the bunch shortening due to the current reduction and the spin polarization. In order to see the effect of the polarization, the Touschek lifetime

[1] Calibration suggests that 0.5 V corresponds to a kick of 1 μrad. This does not agree with the results of the simple simulation described in the appendix. Further work is necessary to clarify this point.

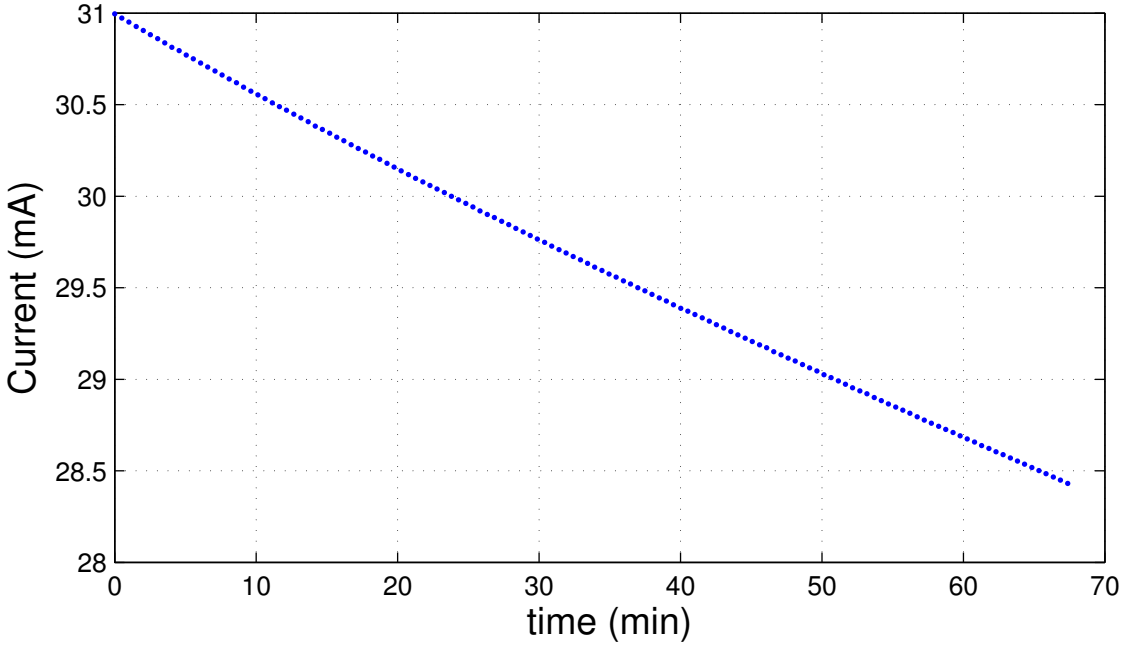

Figure 4.2: Current decay during the polarization measurement over 67 min.

has been rescaled to the value it would have at 31 mA, considering both the current reduction and the bunch shortening.

In figure 4.3, four different lifetime values are shown. The blue points are the measured total lifetimes; the cyan points are the Touschek lifetimes; the green points are the Touschek lifetimes rescaled to the initial current; the red points are the Touschek lifetimes rescaled to the initial current and bunch length.

The Touschek lifetime measured and rescaled to the initial current and bunch length has been fitted, according to equation 4.4, with the function:

$$\tau_t(t) = \left[\frac{1}{\tau_{t0}} - \frac{1}{DTL}\left[1 - \exp\left(-\frac{t-dt}{\tau_p}\right)\right]^2\right]^{-1} \tag{4.5}$$

where τ_{t0}, DTL, dt and τ_p are free parameters.

The results of the fit gives a polarization time:

$$\tau_p = (15.9 \pm 0.6)\,\text{min} \tag{4.6}$$

and the lifetime increase with the total polarization can be computed:

$$\frac{\Delta\tau_t}{\tau_t} = \lim_{t\to+\infty}\frac{\tau_t(t) - \tau_t(dt)}{\tau_t(dt)} = \frac{\frac{1}{\tau_{t0}-\frac{1}{DTM}} - \tau_{t0}}{\tau_{t0}} = 0.150 \pm 0.005 \tag{4.7}$$

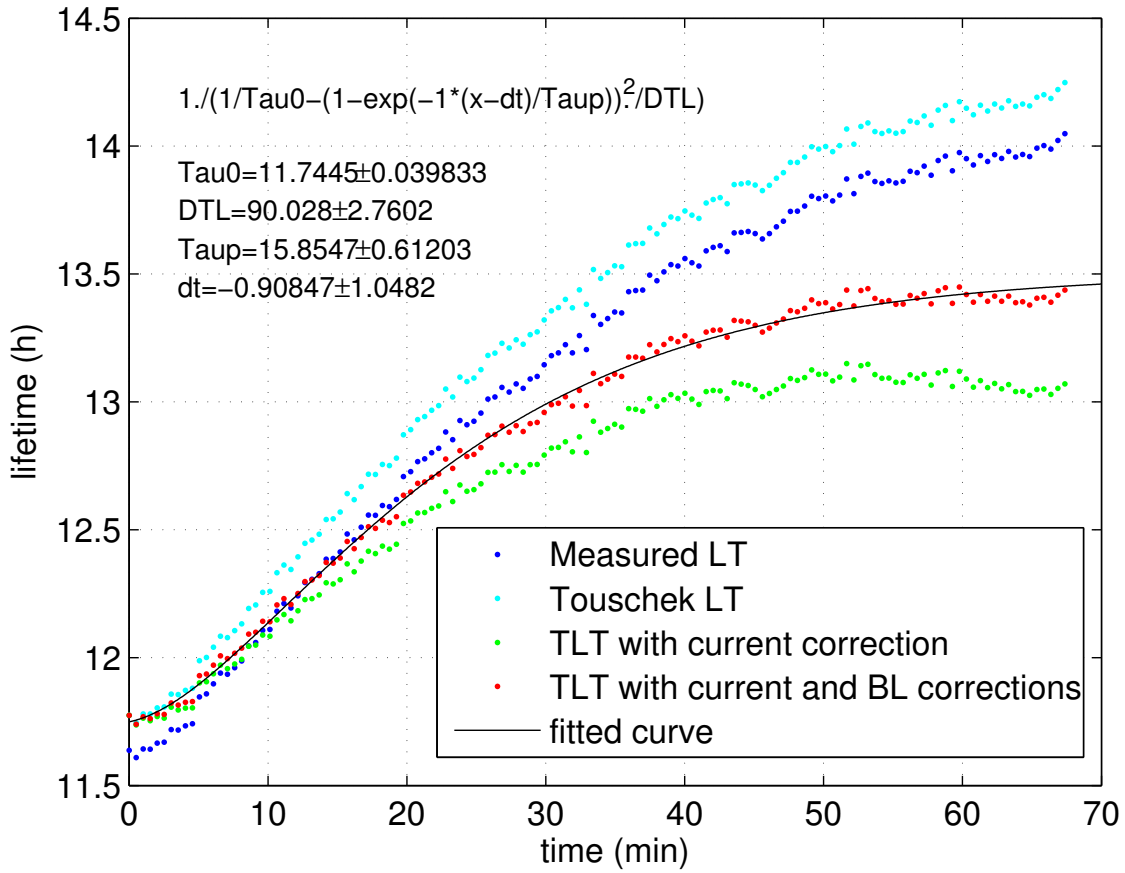

Figure 4.3: Total lifetime and Touschek lifetime variation in 67 min. The blue points are the measured total lifetimes; the cyan points are the Touschek lifetimes; the green points are the Touschek lifetimes rescaled to the initial current; the red points are the Touschek lifetimes rescaled to the initial current and bunch length.

The value of the polarization time obtained from the fit is compatible with the theoretical one, given in section 2.1, equation (2.47):

$$\tau_{p-theo} = 15.75\,\text{min} \tag{4.8}$$

The value of the increase of Touschek lifetime is compatible with a complete polarization, up to the Sokolov-Ternov level, and a constant momentum acceptance of 2.5 % (see table 2.1).

4.3 Touschek lifetime vs RF voltage

In April 02 2013, the Touschek lifetime at different RF-voltages, for three different beam current and vertical emittance has been measured.

The measurements have been done with the beam parameters of table 4.2.

Table 4.2: Beam parameters for Touschek lifetime measurements.

I_b (mA)	I_{tot} (mA)	N_b	ε_y(pm rad)
2.0	32	16	50
1.0	32	32	100
0.037	32	868	10

The total lifetime has been measured varying the RF voltage, from 9 MV to 5.4 MV. The vertical emittance has been increased with a white noise shaker. At each measurement, the beam has been depolarized with an oscillating horizontal magnetic field, as was described in section 4.2.

In figures 4.4, 4.5 and 5.7, the measured Touschek lifetime for the three different beam settings are shown, compared with the simulated values. In the horizontal axis, the readout value of the RF voltage is reported for both the measured and the simulated Touschek lifetime.

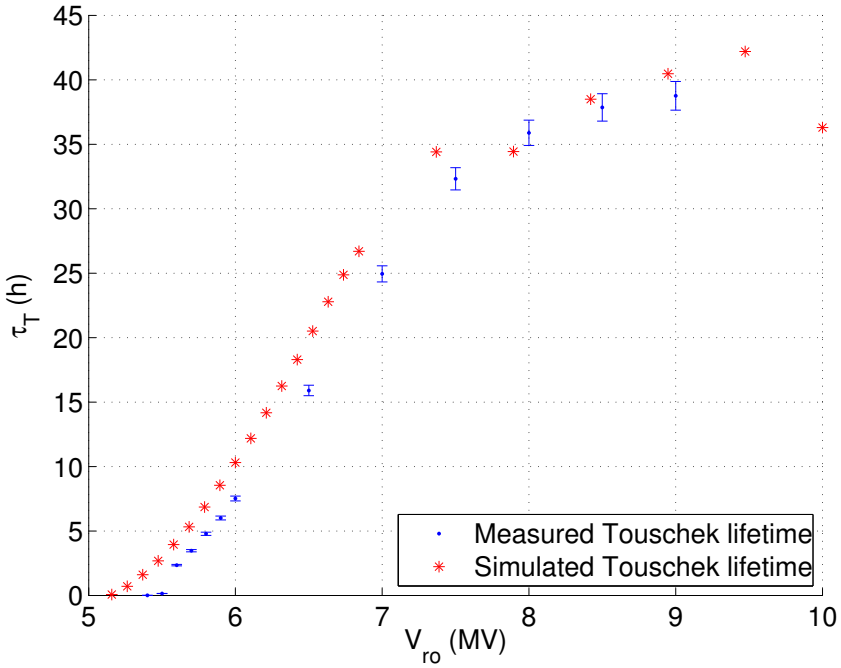

Figure 4.4: Measured and simulated Touschek lifetime with I_b = 2 mA, $\varepsilon_y = 50$ pm rad.

The simulation includes the bunch lengthening effect, due to the high current per bunch, and the RF-voltage calibration obtained from previous measurements, with a calibration factor $k = 0.95$.

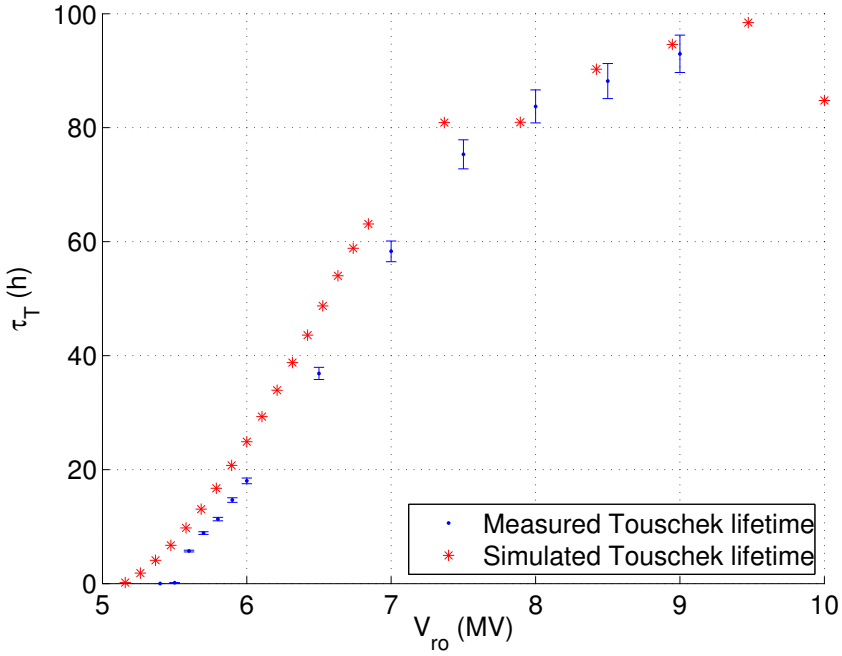

Figure 4.5: Measured and simulated Touschek lifetime with $I_b = 1\,\mathrm{mA}$, $\varepsilon_y = 100\,\mathrm{pm\,rad}$.

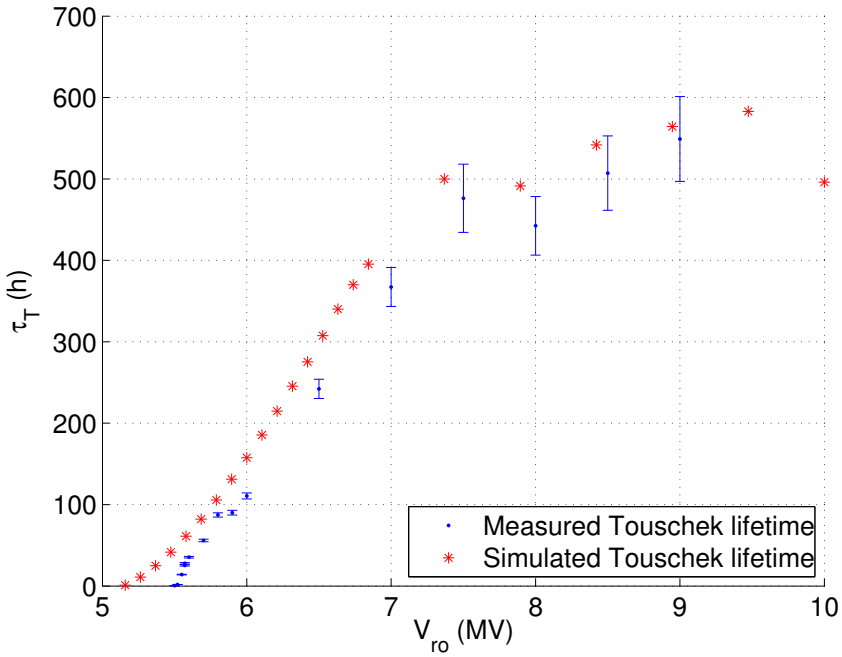

Figure 4.6: Measured and simulated Touschek lifetime with $I_b = 0.037\,\mathrm{mA}$, $\varepsilon_y = 10\,\mathrm{pm\,rad}$.

The measured values of the Touschek lifetime are obtained from the measurement of the total lifetime and the vacuum lifetime. The measurement is rescaled to the nominal value of current and vertical emittance, because during the measurement the current was not constant. Some injections have been done during the measurements, when the total current was reduced of about 10 %.

The measurements with many bunches have higher uncertainties, because the Touschek lifetime is long and the error on vacuum lifetime measurement is dominant.

We have a good agreement between measurements and simulations in the region with high RF voltage, we do not perfectly agree in the low voltage region, where the momentum acceptance is dominated by the RF acceptance.

4.4 Touschek lifetime with physical apertures

The effect of physical apertures on the Touschek lifetime has been studied at ESRF with simulations and experiments.

Some measurements of Touschek lifetime changing the horizontal scraper positions were done, in order to confirm the Touschek lifetime model with physical apertures.

The horizontal scrapers in the ESRF storage ring are near the injection septum, in the high β straight section. Internal and external scrapers can be closed independently.

The horizontal scrapers are usually used to kill the beam. When the scrapers position is about 1 mm from the beam trajectory, the lifetime is a few minutes.

Both the internal and the external scrapers have been moved from 20 mm to 2 mm from the center of the beam.

The measurements have been done with a high bunch current, 2 mA per bunch, in order to be in a Touschek dominated regime. The total current was 64 mA, in 32 bunches. During the measurement, several new injections have been performed, in order to kept the beam current between 60 mA and 64 mA. The vertical emittance have been increased up to $\varepsilon_y = 10$ pm rad with a white noise vertical shaker. The beam has been depolarized every two lifetime measurements.

The vacuum lifetime has been measured by increasing the vertical emittance with the white noise shaker before the Touschek lifetime measurements. The vacuum lifetime was more than 800 h.

In figures 4.7 and 4.8 the Touschek lifetimes versus the horizontal scraper position, external and internal, are shown.

A good agreement between the Touschek lifetime simulations and the measure-

ments has been obtained when the scraper is closer than 15 mm.

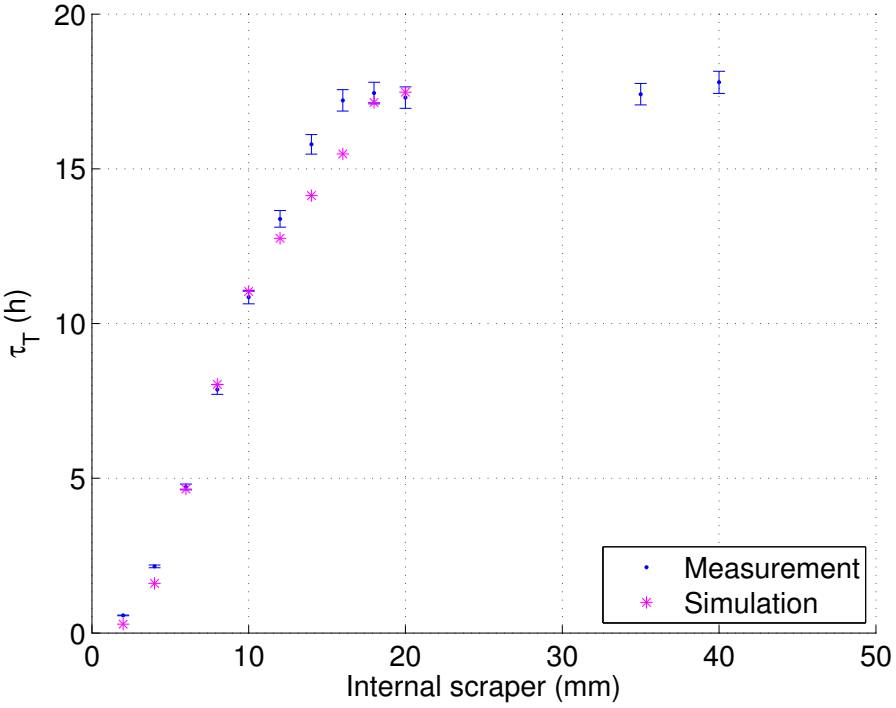

Figure 4.7: Measured and simulated Touschek lifetime versus internal scraper position.

In the ESRF storage ring, 64 beam loss monitors are installed. At each step of the measurements, the beam loss monitors signals has been stored.

In figure 4.9, the beam losses stored by the beam loss monitors during the Touschek lifetime measurements are shown for four different positions of the internal scraper.

The scrapers are in the injection cell (the number 4). When the scrapers are closed, the losses measured in beam loss monitor number 7, the one near the scrapers, are larger. More losses than the average value are measured in cells 16, 19 and 26. It is not clear why many losses are concentrated in those cells. When the scrapers are closed, the losses are mostly in cell 4.

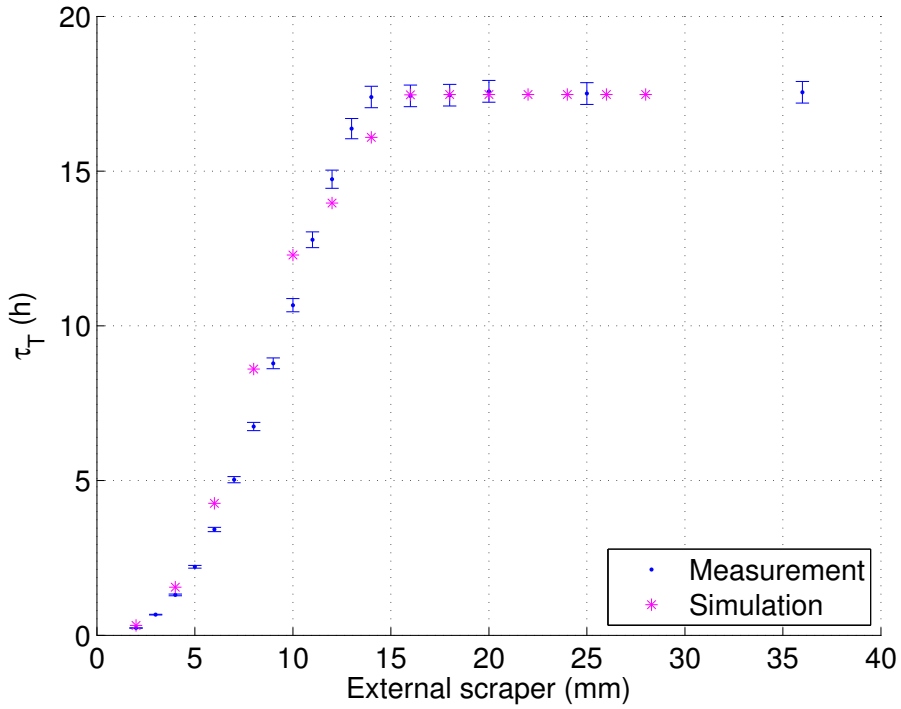

Figure 4.8: Measured and simulated Touschek lifetime versus external scraper position.

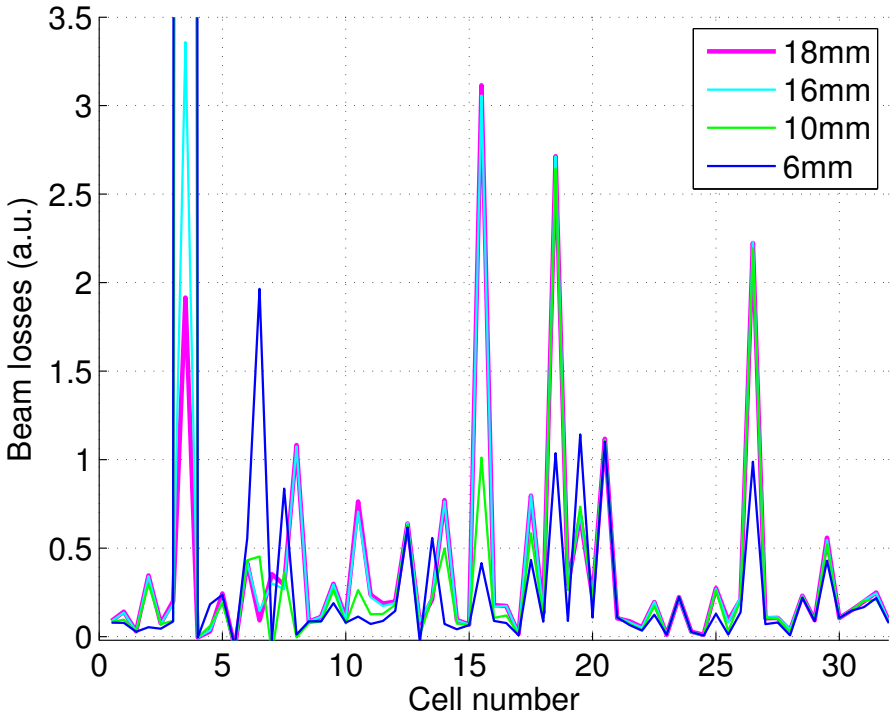

Figure 4.9: Beam losses stored by the beam loss monitors during the Touschek lifetime measurements for different internal scraper positions.

Chapter 5

Optimization and testing of alternate sextupole setting

In previous chapters, the model used to predict the Touschek lifetime has been presented, together with the measurements done to confirm the model. The agreement between measurements and simulations of Touschek lifetime, varying some beam parameters, RF voltage, physical apertures, beam current and vertical emittance, is seen to be quite good for the nominal sextupole setting, after all effects are taken into account.

Once the model can predict the Touschek lifetime of the beam, a new sextupole setting, giving a longer Touschek lifetime, maintaining a sufficiently large injection efficiency, has been searched for.

The momentum acceptance simulation needs several hours of computer time, therefore a direct optimization of the momentum acceptance needs a very large computer power.

At ESRF there is a cluster with 850 processor cores that have been used for this purpose. The multi-objective optimizer `geneticOptimizer`, distributed with `elegant`, has been used [34].

In order to maintain a large injection efficiency, the dynamic aperture must be sufficiently large. Thus, in addition to optimizing the momentum acceptance, the dynamic aperture is also optimized.

The dynamic aperture is defined as the area in $x - y$ plane where a particle without transverse momentum can be injected and stored in the storage ring.

The dynamic aperture can be computed by tracking particles at different $x - y$ coordinates, without transverse momentum, for many turns.

Particles are tracked starting from many points in n lines from the origin $(0, 0)$ to $(x_{max} \cos\theta_n, y_{max} \sin\theta_n)$. Where x_{max} and y_{max} are chosen by the user and $-\pi/2 \leq$

$\theta_n \leq \pi/2$.

Usually, in the ESRF lattice, the RF cavity is not necessary in the dynamic aperture computations. However, in particular in the ESRF upgrade lattice, the effect of the cavity is not always negligible, because off axis particles arrived to the cavity with a slightly wrong phase and get a different acceleration. This effect is explained in the appendix D.

In figure 5.1, the dynamic aperture of the nominal ESRF storage ring lattice, in the injection straight section, computed with `elegant`, including longitudinal motion and synchrotron radiation, is shown.

The dynamic aperture is limited by the injection septum, at $x = -1.95\,\mathrm{cm}$.

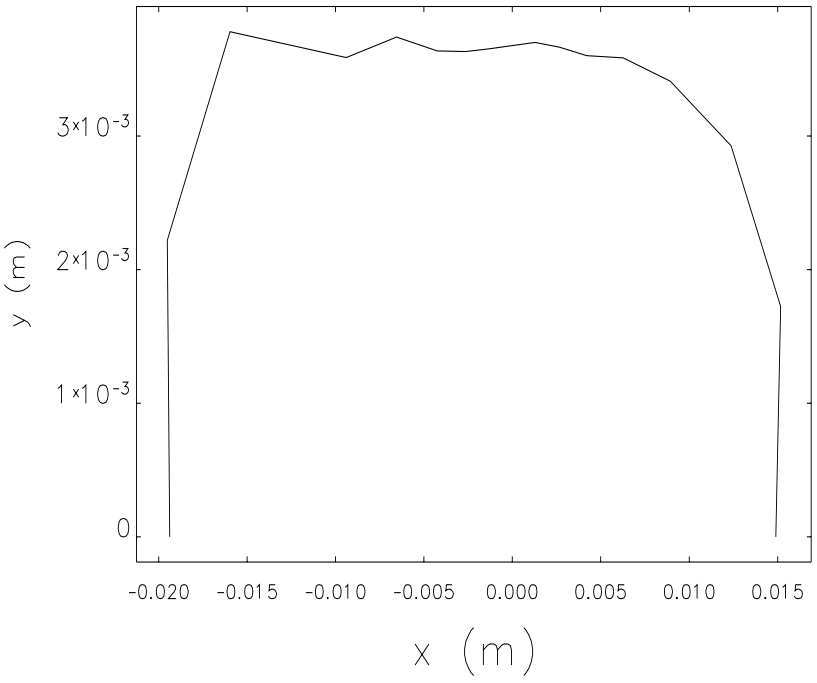

Figure 5.1: Dynamic aperture of the nominal ESRF lattice, calculated tracking particles in 17 lines, for 512 turns.

In this chapter, the algorithm used to optimize the sextupole setting, the results of the optimizations and the test measurements are presented.

5.1 Optimization algorithm

The script `geneticOptimizer` is a multi-objective optimizer, is distributed with `elegant` and it is written in `Tcl` script language.

The algorithm changes some magnet strengths in the lattice, satisfying some constraints, and it runs `elegant` in order to compute some quantities to be minimized or maximized.

The optimizer has been used in this thesis work in order to find a sextupole setting that gives a longer Touschek lifetime and a larger dynamic aperture. The Touschek lifetime and the dynamic aperture need a few hours of computer time to be computed and the optimizer generates some thousands of different sextupole settings, therefore a large computer power is needed for the optimization.

The algorithm generates a number of initial different sextupole settings (N) varying the magnets strengths randomly in a gaussian distribution around a given initial sextupole setting. The standard deviation of the gaussian distributions can be set by the user. The script submits N jobs to the cluster in order to evaluate the Touschek lifetime and the dynamic aperture of the N sextupole settings with `elegant`.

The script choses the best P sextupole settings, which are called *parents*, computes new sextupole settings and submits new jobs to the cluster. The new sextupole settings are computed mixing the sextupole strengths of the *parents* and adding some random variations.

In the multi-objective optimization problems, a solution that maximize all the objective functions may not exist. A solution is called non-dominated, or Pareto optimal, if none of the objective functions can be increased without decreasing some of the others. The *parents* are chosen from the non-dominated solutions of the optimization.

The algorithm never stops. During the run, the user can view the status of the optimization and can stop the optimization.

Some constraints can be defined, such as the values of the horizontal and vertical chromaticity. The chromaticities can be set to the desired values changing two sextupole strengths.

5.2 Results of optimization

In the ESRF cells, there are 7 sextupoles and two of them are used to change the chromaticity. In cells 15, 16, 22, 23, 29 and 30 there are some sextupoles with individual power supplies.

The variables changed during the optimization are the strengths of the harmonic sextupoles: the ones in the standard cells and the independent ones. The chromaticity sextupoles have been used to set the horizontal and vertical chromaticities to the

nominal values. A multi-objective optimization, with two objectives, has been performed. The two chosen quantities to be maximized have been the dynamic aperture area and the Touschek lifetime.

The optimization procedure has generated about 2500 different sextupole settings, running 100 parallel jobs for a few days.

In figure 5.2, the dynamic aperture and the Touschek lifetime for a fraction of all the sextupole settings found in the optimization are shown. The Pareto optimal solutions are the blue points.

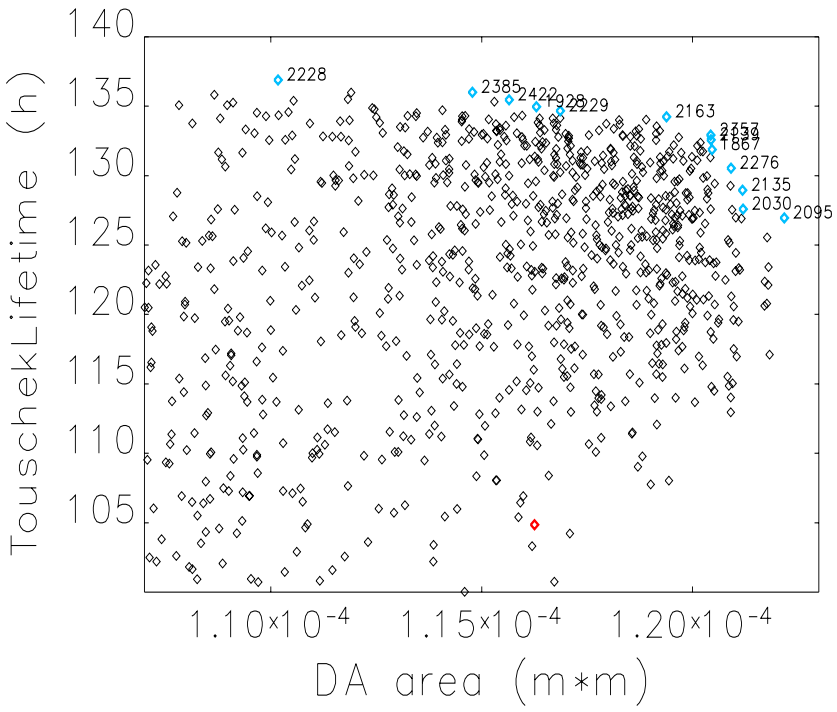

Figure 5.2: Touschek lifetime and dynamic aperture for many different sextupole settings found in the optimization. The red point is the original lattice value, the blue points are the non-dominated, or Pareto optimal, solutions. Touschek lifetime is computed in low current per bunch mode, with low vertical emittance.

The sextupole setting number 2163 has been chosen, because it produce a longer lifetime in the simulation and a slightly larger dynamic aperture, and therefore a larger injection efficiency.

The sextupole strengths of the 2163 lattice, compered with the nominal strengths, are shown in table 5.1.

The momentum acceptance, used for the Touschek lifetime computation, and the

Table 5.1: Sextupole strengths of nominal lattice and optimized lattice number 2163.

Sextupole name	nominal lattice $K_2\,[\mathrm{m}^{-3}]$	optimized lattice $K_2\,[\mathrm{m}^{-3}]$
S4	6.3558	6.6107
S6	-8.4172	-8.8501
S13	-4.5315	-3.7767
S19	22.1320	21.7148
S20	-20.8919	-20.9639
S22	-4.9234	-5.0428
S24	6.7633	6.7367
S4 (cells 15, 16, 29, 30)	12.3622	13.1149
S22 (cells 22, 23)	-5.6013	-6.3673
S24 (cells 22, 23)	13.8812	16.7559

dynamic apertures are computed with `elegant`, using the β-functions modulations measured during the machine dedicated time of April 02 2013.

In figures 5.3 and 5.4, the Touschek lifetime for the nominal lattice and for the optimized one are shown for different RF voltages.

The Touschek lifetime of the optimized lattice, including the physical apertures, is longer than the one of the nominal lattice by a factor of $20 - 25\%$. The same increased lifetime has been obtained using different β-function modulations, as can be seen in figures 5.5 and 5.6.

We note in particular that the physical apertures play a very important role in determining the lifetime in these calculations. To illustrate this point, we show the value of the computed lifetime with the same sextupole settings, but without physical apertures. In particular, we find that without physical apertures, the lifetime of the optimized lattice is not much longer than the one of the nominal lattice.

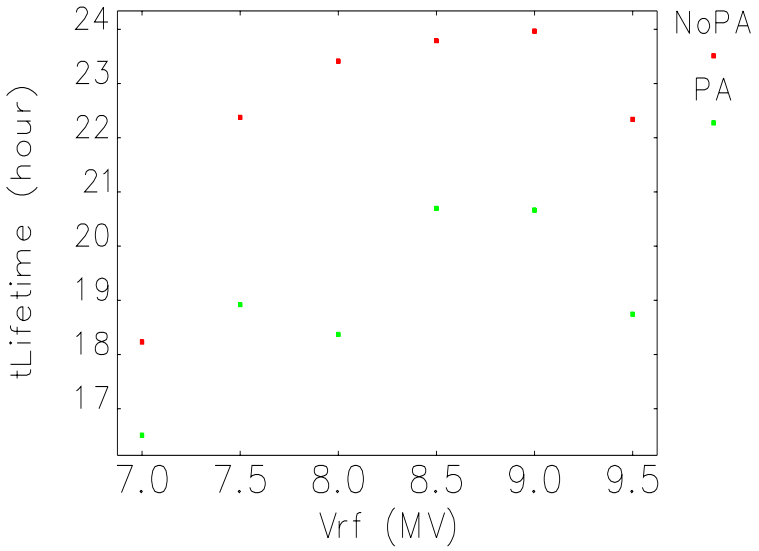

Figure 5.3: Touschek lifetime versus RF voltage for nominal sextupole setting. In red, the Touschek lifetime is computed removing the physical apertures from the lattice. β-functions modulations measured in April 02 2013.

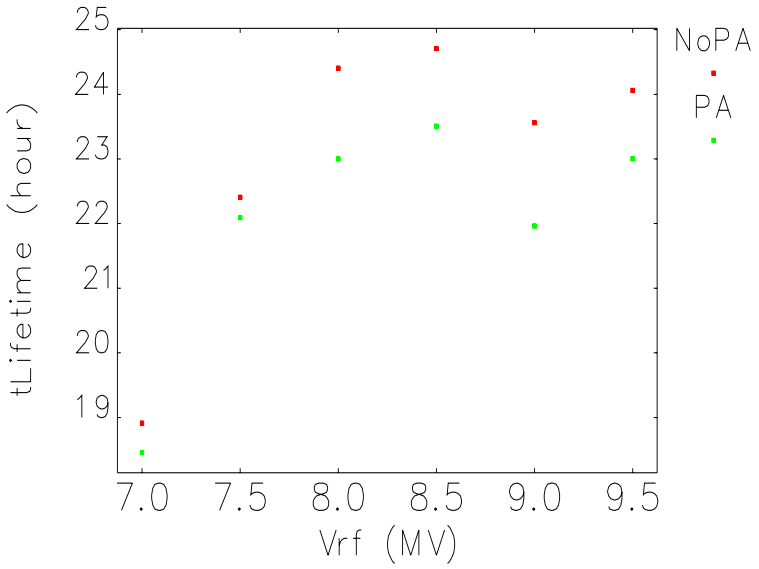

Figure 5.4: Touschek lifetime versus RF voltage for optimized sextupole setting number 2163. In red, the Touschek lifetime is computed removing the physical apertures from the lattice. β-functions modulations measured in April 02 2013.

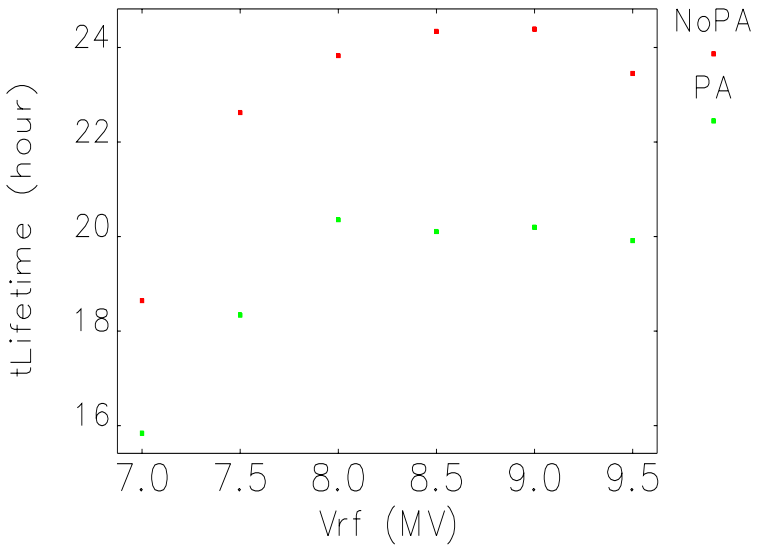

Figure 5.5: Touschek lifetime versus RF voltage for nominal sextupole setting. In red, the Touschek lifetime is computed removing the physical apertures from the lattice. β-functions modulations measured in July 02 2013.

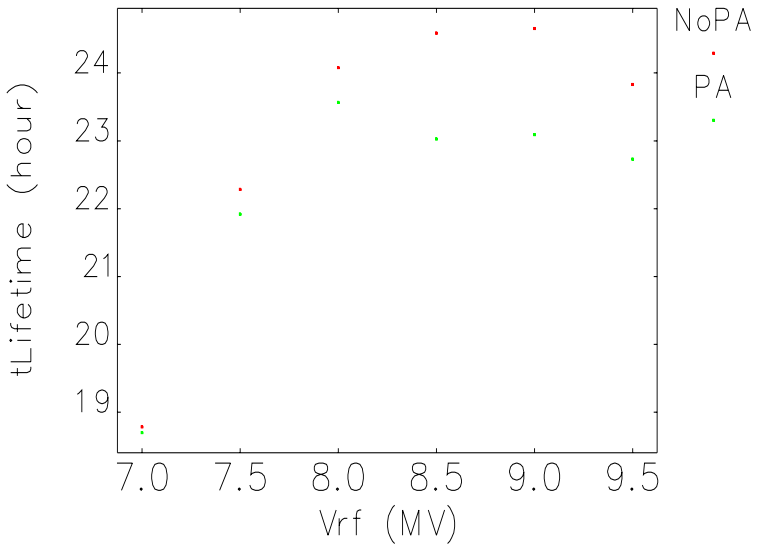

Figure 5.6: Touschek lifetime versus RF voltage for optimized sextupole setting number 2163. In red, the Touschek lifetime is computed removing the physical apertures from the lattice. β-functions modulations measured in July 02 2013.

Lifetime measurement with different sextupole setting

In July 2013, the optimized lattice number 2163 has been tried in the ESRF storage ring.

The measurements have been performed at 2 mA per bunch. The lifetime measurements have been been done as described in chapter 4.

The lifetime of the nominal lattice has been measured for different RF voltages and then the sextupole currents have been changed and the lifetime has been measured again.

At low RF voltages, the Touschek lifetime is the same for the two lattices, because the momentum acceptance is limited by the RF acceptance and not by the dynamic acceptance.

At 8 MV, the lifetimes of the two sextupole settings are different, but with the nominal lattice the lifetime results longer than with the optimized lattice.

It's not clear from the model why the lifetime results shorter with the new sextupole setting. Possibly the coupling between horizontal and vertical motion is not perfectly modeled, therefore the effect of the vertical apertures is not well taken into account. Without the physical apertures, the lifetimes of the two sextupole settings are very similar.

A measurement of the Touschek lifetime versus vertical scraper position could be done to understand the vertical apertures model.

As a side note, the injection efficiency with the new sextupole settings was significantly larger than the one of the nominal lattice, also at first injection, without orbit corrections.

Clearly, further modeling work and measurements are necessary to find sextupole settings that improve the ESRF lifetime.

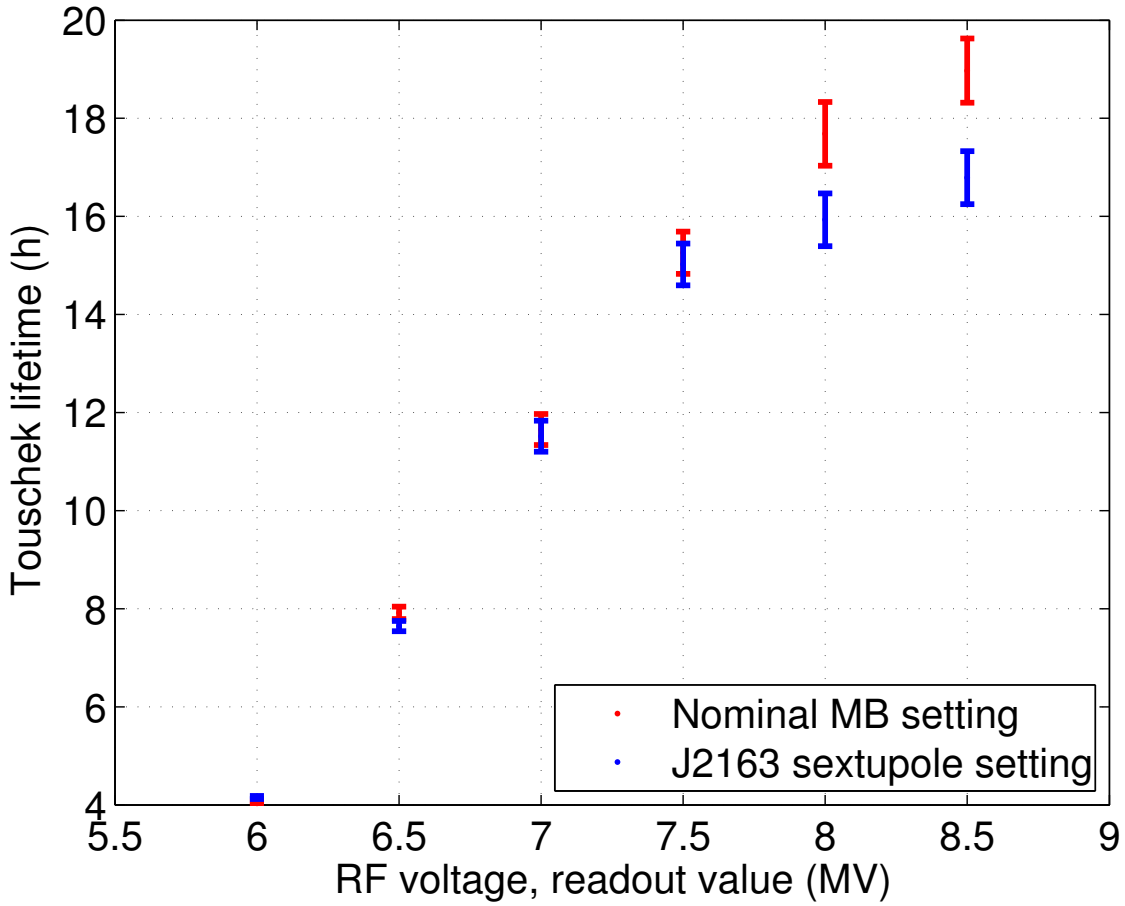

Figure 5.7: Measured Touschek lifetimes for nominal multi-bunch sextupole setting and for the new J2163 sextupole setting.

Chapter 6

Bunch lengthening and intrabeam scattering for the ESRF low emittance upgrade lattice

As discussed in chapter 1, an upgraded lattice for ESRF is currently under study. We would like to apply the same modeling work used on the current ESRF lattice to this upgraded lattice. In addition, we find that due to the lower emittance, the effect of intrabeam scattering must also be included.

In this chapter, the bunch lengthening due to the potential well effect and the Intrabeam scattering are studied for the ESRF upgrade low emittance lattice, in order to know the bunch lengths and the emittances for Touschek lifetime studies.

Bunch length varies with current mostly due to the potential well effect and partially due to the Intrabeam scattering. Emittances vary with current due to Intrabeam scattering. The values of bunch length and emittances for different RF voltages and bunch current, which varies for different operation modes, will be estimated.

The operation modes of the ESRF upgraded lattice are assumed to be the same as the present ESRF storage ring (table 1.1).

6.1 Bunch lengthening

An estimation of the impedance of the new lattice has not been done, so here the same value of impedance found in section 3.2 for the present ESRF storage ring, $Z_n = 0.7\,\Omega$, is assumed.

As written in section A.3.1, the bunch lengthening effect can be approximated,

in case of purely inductive impedance, by this equation:

$$\left(\frac{\sigma_z}{\sigma_{z_0}}\right) = \frac{\sqrt[3]{\sqrt{3}\sqrt{27Q^2-4}+9Q}}{\sqrt[3]{18}} + \frac{\sqrt[3]{\frac{2}{3}}}{\sqrt[3]{\sqrt{3}\sqrt{27Q^2-4}+9Q}} \tag{6.1}$$

with $Q = \frac{\Delta}{4\sqrt{\pi}}$ and

$$\Delta = \frac{\alpha e I_b}{E_0 \nu_s^2}\left(\frac{c}{\omega_0 \sigma_{z0}}\right)^3 Z_n \tag{6.2}$$

where α is the momentum compaction factor, e is the electron charge, I_b is the bunch current, E_0 is the beam energy, ν_s is the synchrotron tune, c is the speed of light, ω_0 is the revolution angular frequency ($\omega_0 = 2\pi\frac{c}{C}$), σ_{z0} is the zero current bunch length, Z_n is the impedance.

In figure 6.1 the bunch lengthening in the ESRF storage ring and in the new lattice are shown. The RF voltage is assumed to be 8 MV for the ESRF storage ring and 4, 5 or 6 MV for the new lattice.

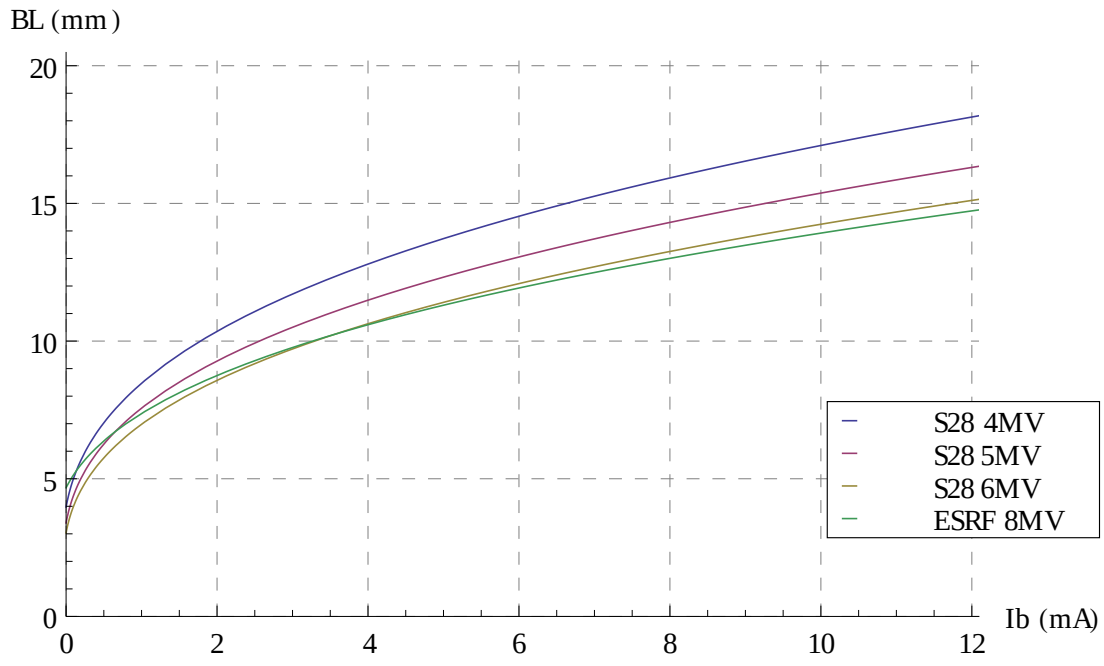

Figure 6.1: Bunch lengthening due to the potential well effect, assuming a purely inductive impedance $Z_n = 0.7\,\Omega$, for present ESRF storage ring and for S28 version of new low emittance lattice.

We notice that the lengthening effect is higher in the new lattice, compared with the present machine, however, the zero current bunch length is smaller than in the present machine.

6.2 Intrabeam scattering

Let us now consider the effect of intrabeam scattering (IBS) on the beam emittances. We start by examining how the IBS scattering rate varies around the ring.

As an example, we take $Q_b = 16.2\,\mathrm{nC}$, which gives a bunch length from potential well effect of about $\sigma_z = 14\,\mathrm{mm}$, we take a vertical emittance of $\varepsilon_{y0} = 7.3\,\mathrm{pm}$, assuming this comes only from coupling, this implies a horizontal emittance of $\varepsilon_{x0} = 146\,\mathrm{pm}$.

Using the `IBSEmittance` code, we find a final horizontal emittance of $\varepsilon_x = 170.1\,\mathrm{pm}$ and a growth rate of $\frac{1}{T_x} = 32.8\,\mathrm{s}^{-1}$. We can see that equation (A.89) is satisfied. In figure (6.2) the growth rates are plotted around the ring.

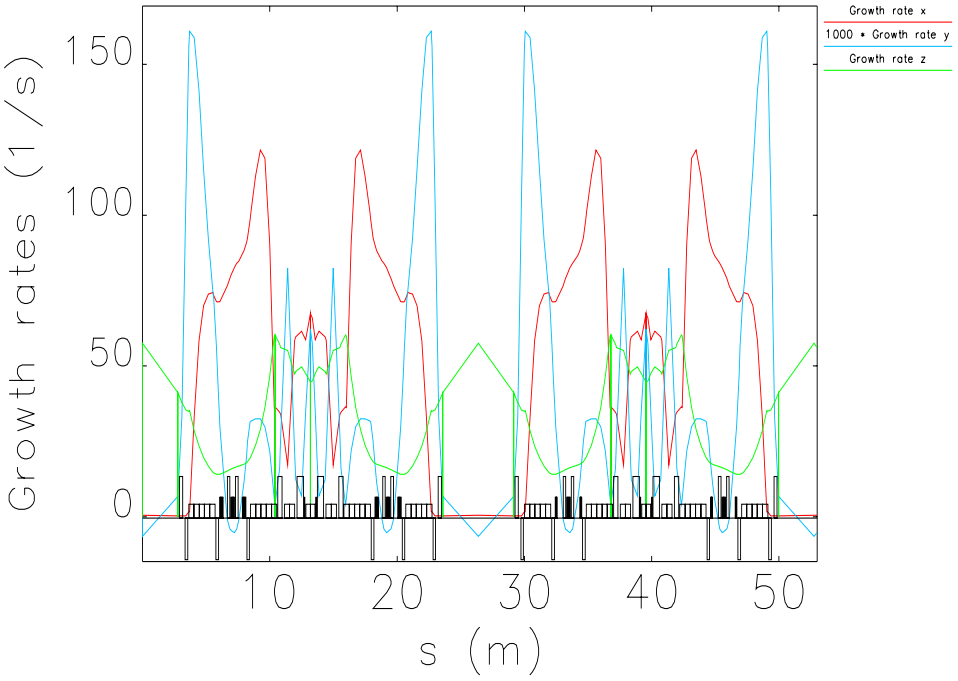

Figure 6.2: IBS emittance growth rates around the ring computed by `IBSEmittance`.

Figures 6.3 and 6.4 show the results of the IBS computations. In the first the equilibrium horizontal emittance growth computed via the `Elegant` module is shown, for the second figure, the code of T. Demma has been used. We show the results for several different vertical emittance values. We note quite good agreement for the larger emittances, but less good for the smaller values, between the two codes. This is expected given the approximation used in Demma's code.

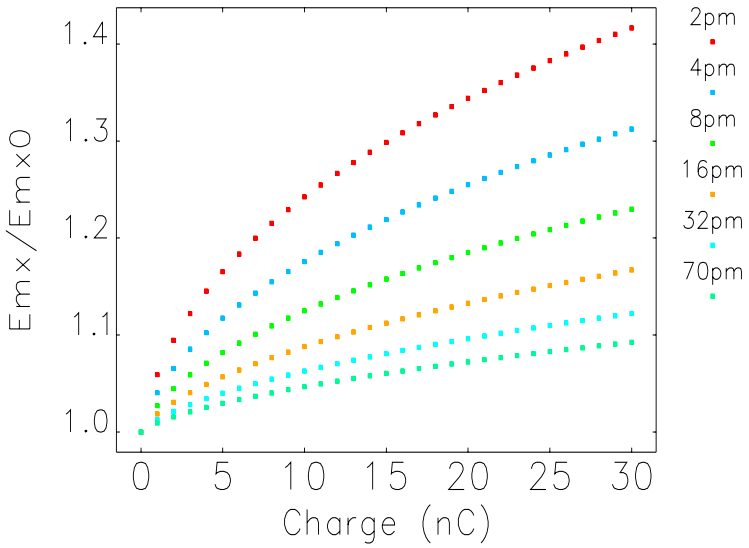

Figure 6.3: Horizontal emittance growth with Elegant.

In figure 6.5, the equilibrium bunch length is shown as a function of bunch charge, for different vertical emittances. We can see that the impedance effect is dominant, with only a small additional growth coming from the IBS.

In figure 6.6 we show the time evolution of the horizontal emittance for different initial values. This is simply to check the code and also to understand the time scale over which IBS equilibrium is established.

For these studies we have assumed that the vertical emittance comes entirely from coupling, i.e. the vertical dispersion is zero. Further we assume the case with the tunes near a difference resonance, where $\varepsilon = \varepsilon_x + \varepsilon_y$ is constant as the coupling

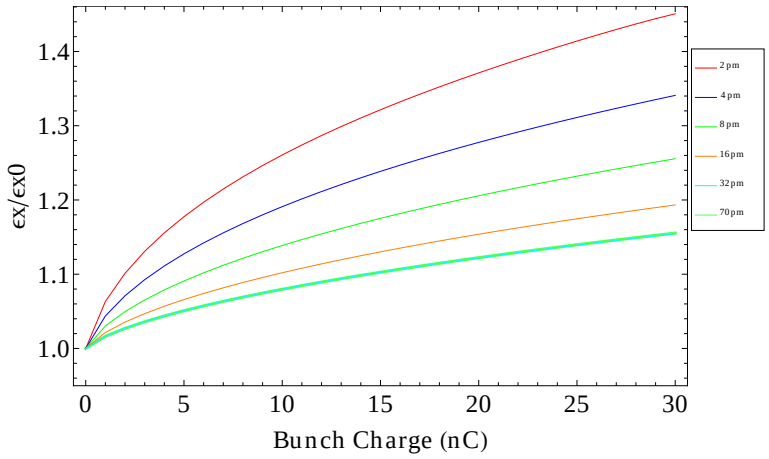

Figure 6.4: Horizontal emittance growth with Demma's code.

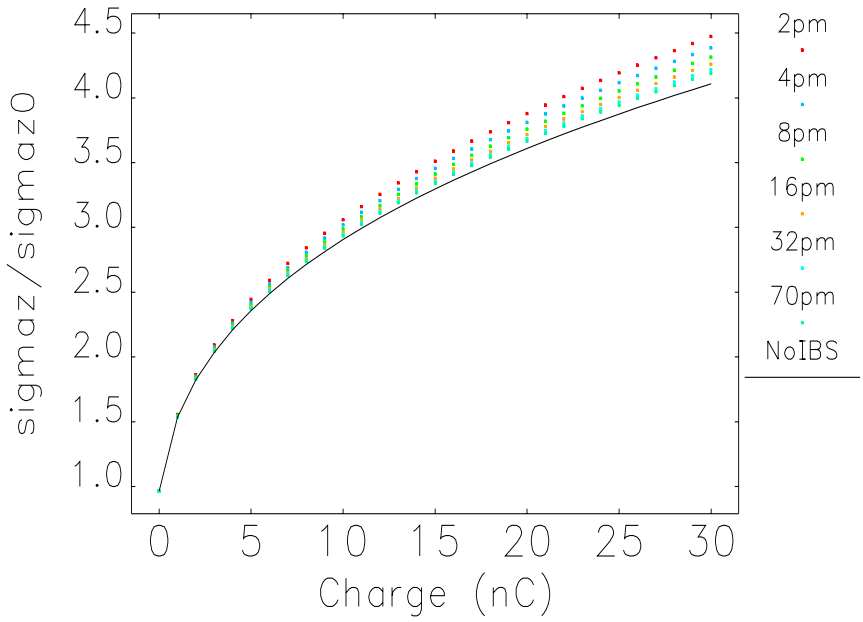

Figure 6.5: Bunch length due to impedance and IBS as a function of bunch current for some different values of vertical emittance.

is varied.

Reference [36] gives a factor $r_\varepsilon = \frac{\varepsilon_{y0,k}}{\varepsilon_{y0}}$ which determines how much vertical emittance comes from coupling. `Elegant` forces $r_\varepsilon = 1$, Demma's code allows the value to be set. The factor r_ε has been set $r_\varepsilon = 1$ in these calculations, which implies that the vertical emittance growth is equal to the horizontal emittance growth.

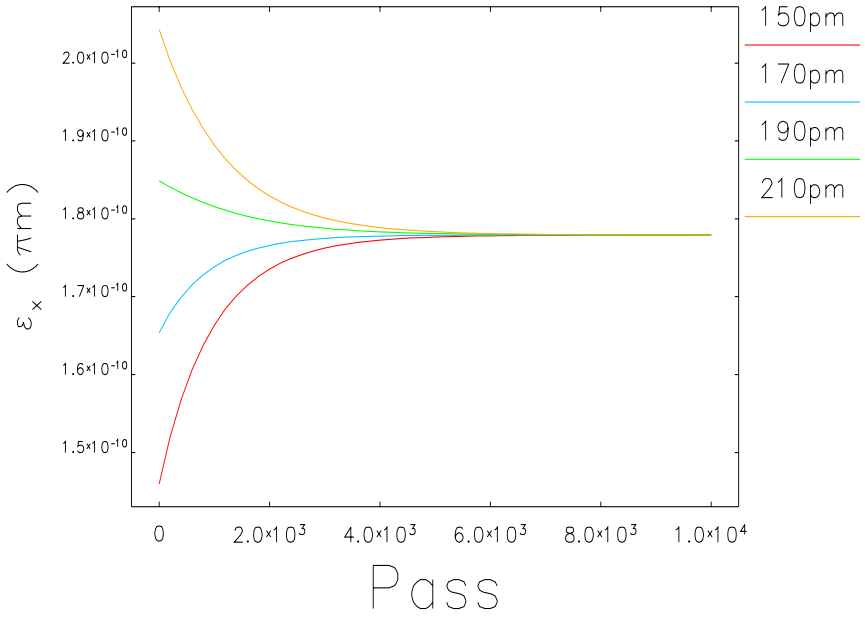

Figure 6.6: Emittance evolution to the equilibrium, computed with `IBSEmittance` module of `elegant`.

For Touschek lifetime computation, we now assume we will be able to reduce the vertical emittance down to 5 pm, by reducing the coupling with skew quadrupole correctors. The emittance growths for different vertical emittance is computed for the four different bunch currents with `elegant`. The results of the computation is shown in figure 6.7. The bunch length including the potential well effect is included in the computation and is computed assuming 5 MV RF voltage.

In figure 6.8, the equilibrium horizontal emittance after IBS versus the vertical equilibrium emittance after IBS is shown for the higher current per bunch mode, for three different RF voltages: 4 MV, 5 MV and 6 MV

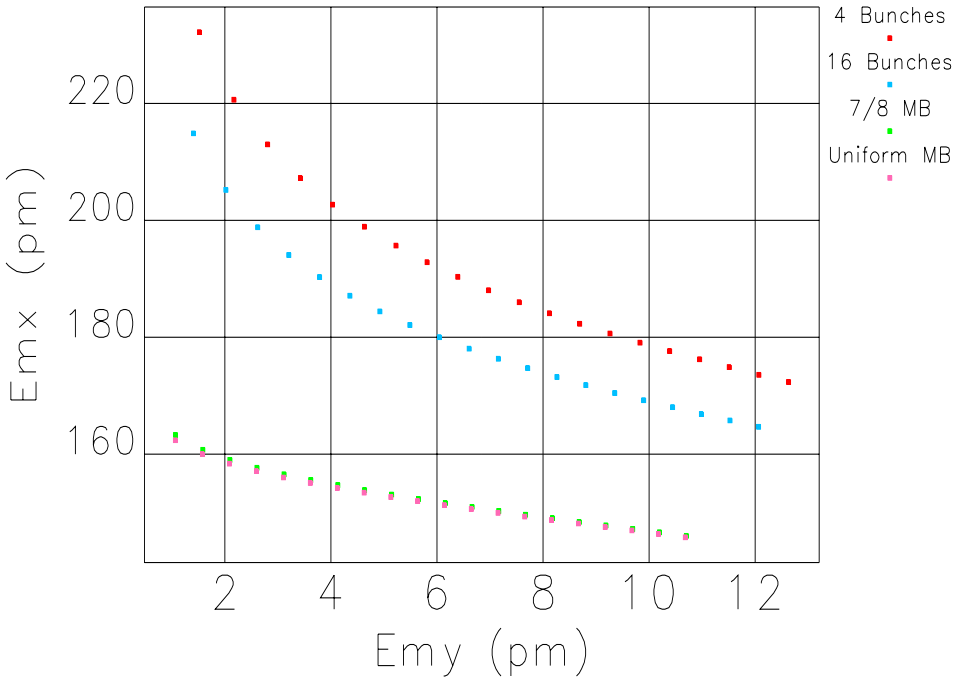

Figure 6.7: Horizontal emittance after IBS versus vertical emittance after IBS, computed with `IBSEmittance` module of `elegant`.

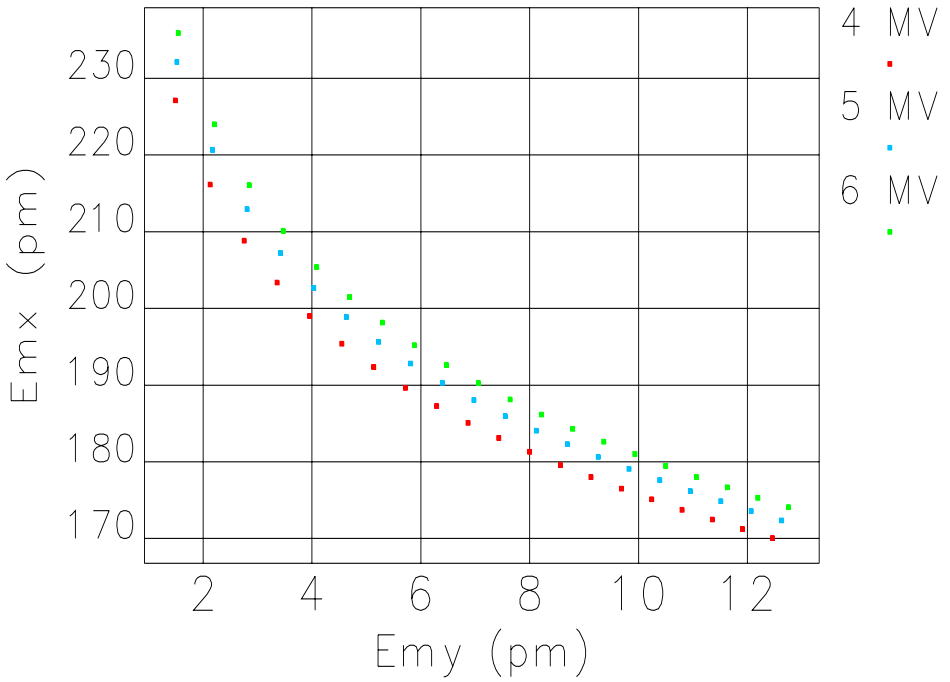

Figure 6.8: Horizontal emittance after IBS versus vertical emittance after IBS, for 10 mA per bunch mode, for three different RF voltages.

Chapter 7

Touschek lifetime for the new lattice

In chapter 6, the bunch length and the emittance growths have been computed for the new low emittance ESRF upgrade lattice. In this chapter, those results are used to compute the lifetime of the lattice for the four different filling modes.

If figure 7.1, the RF acceptance versus RF voltage for the present and new lattice is shown.

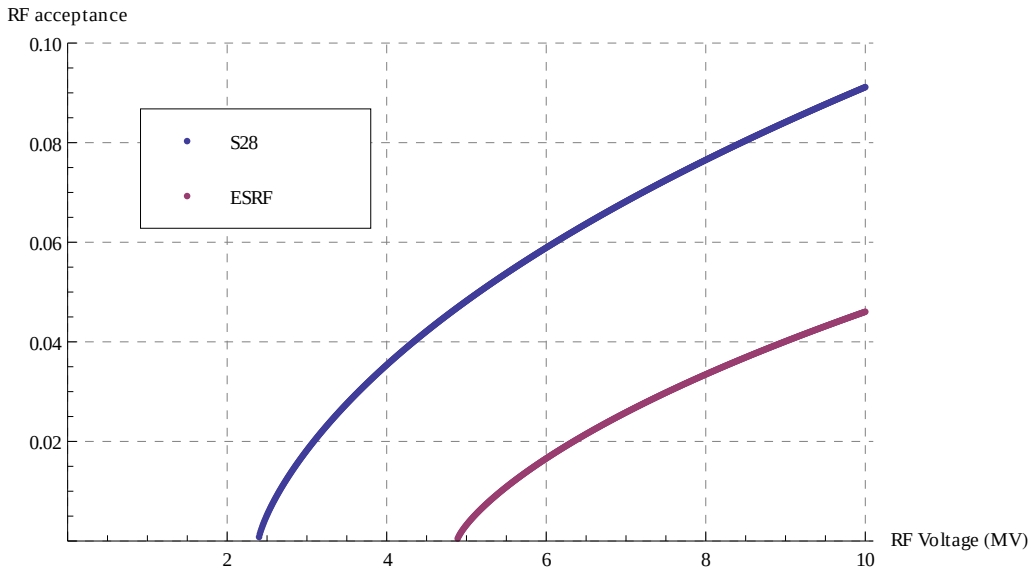

Figure 7.1: Momentum acceptance due to RF cavity for present ESRF lattice and for version S28 of the ESRF upgrade lattice.

The momentum acceptance of the perfect lattice, including the injection section with the high horizontal β-function, has been computed with the 6D particle tracking code `AT`, for some different RF voltages. The synchrotron radiation has been included. In figure 7.2 the momentum acceptance is shown.

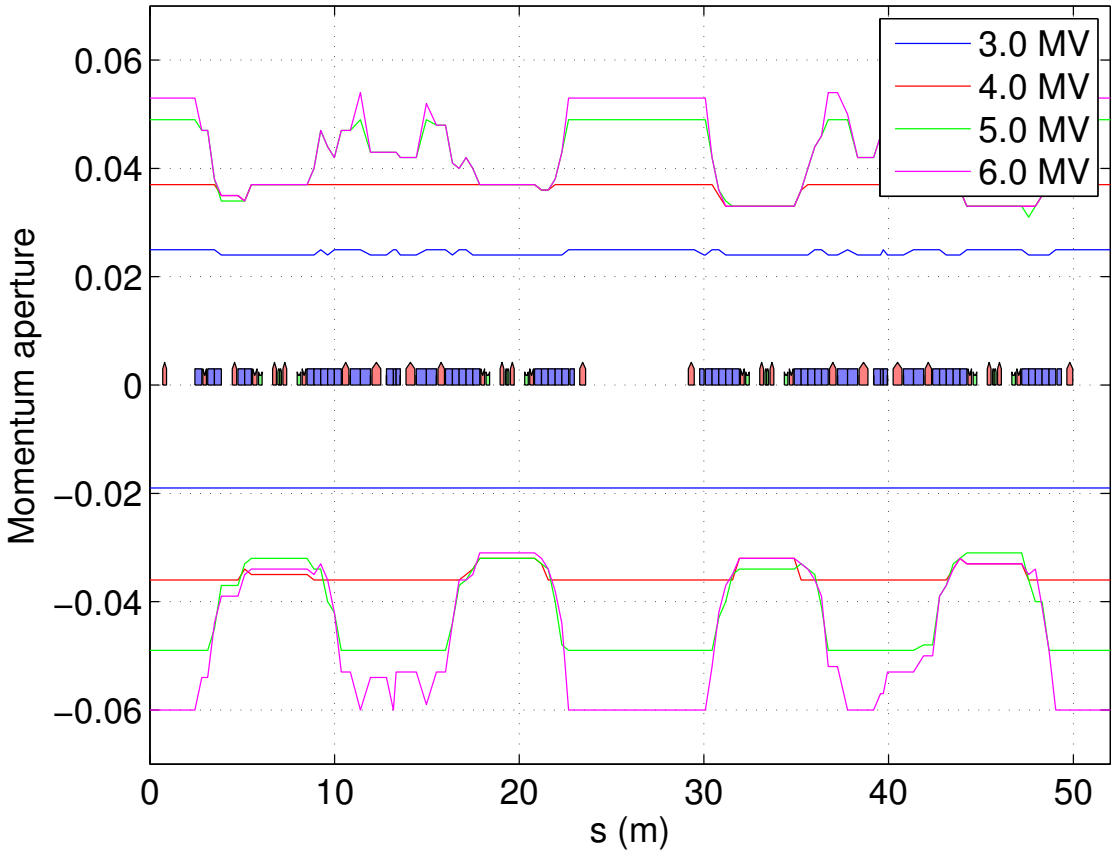

Figure 7.2: Momentum acceptance computed with 6D particle tracking, using `AT`, with different RF voltages. The momentum acceptance has been computed after all elements with non-zero length. Version S28 of the new low emittance lattice, without errors, has been used.

The impact of magnet field errors and misalignments on the momentum acceptance and on the Touschek lifetime has also been studied. Four lattices with random misalignments of quadrupoles and sextupoles and random field errors of quadrupoles and sextupoles have been produced [37] and they are used for the Touschek lifetime studies.

In figure 7.3, the momentum acceptance for the lattice with injection section and with errors is shown.

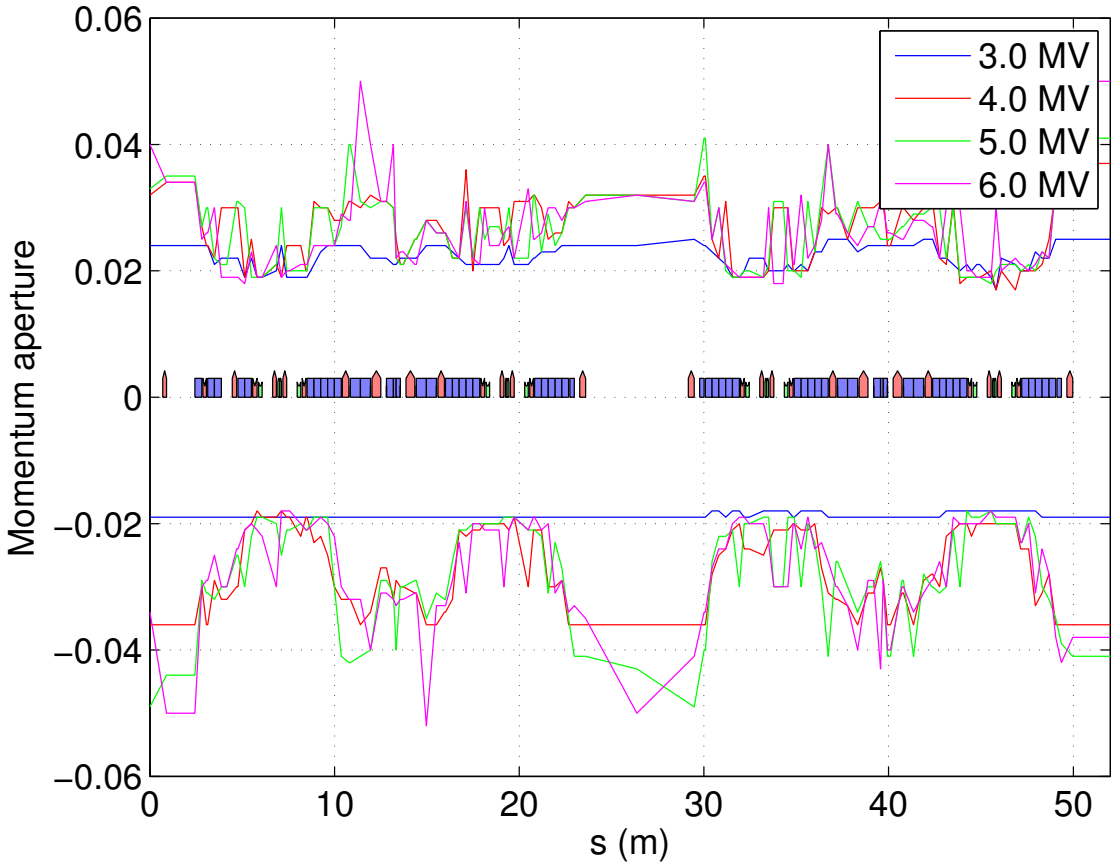

Figure 7.3: Momentum acceptance computed with 6D particle tracking, using `AT`, with different RF voltages. The momentum acceptance has been computed in all elements with non zero length. Version S28 of the new low emittance lattice, with quadrupoles and sextupoles misalignments and field errors has been used. The scattering rate is the probability of Touschek scattering and it is the inverse of the beam size, in arbitrary units.

The Touschek lifetime for three different filling modes, for a range of RF voltages, from 2.5 MV to 7.0 MV, have been computed, including the bunch lengthening due to the potential well effect[1] and including the horizontal emittance growth due to intrabeam scattering. The vertical emittance is fixed to 5 pm. The momentum acceptance has been computed for the perfect machine and for the lattice with quadrupoles and sextupoles random field errors and misalignments, with four different seeds.

In figures 7.4, 7.5 and 7.6, the Touschek lifetimes versus RF voltage are shown for the perfect machine and for the machine with four different set of errors.

From the Touschek lifetime versus RF voltage plots, we can see that in the

[1]Recall that the bunch lengthening is dependent on the longitudinal impedance Z_n. If this value is different, this will effect the lifetime results.

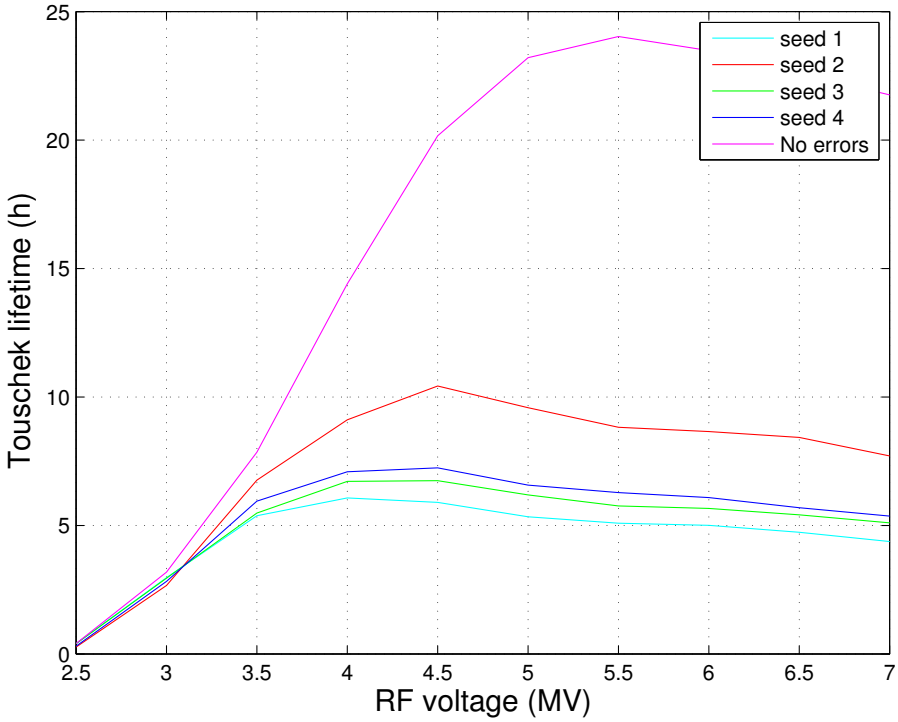

Figure 7.4: Touschek lifetime versus RF voltage in uniform multi-bunch mode, with 0.230 mA per bunch.

machine with errors the maximum lifetime is achieved with an RF voltage between 4 MV and 4.5 MV.

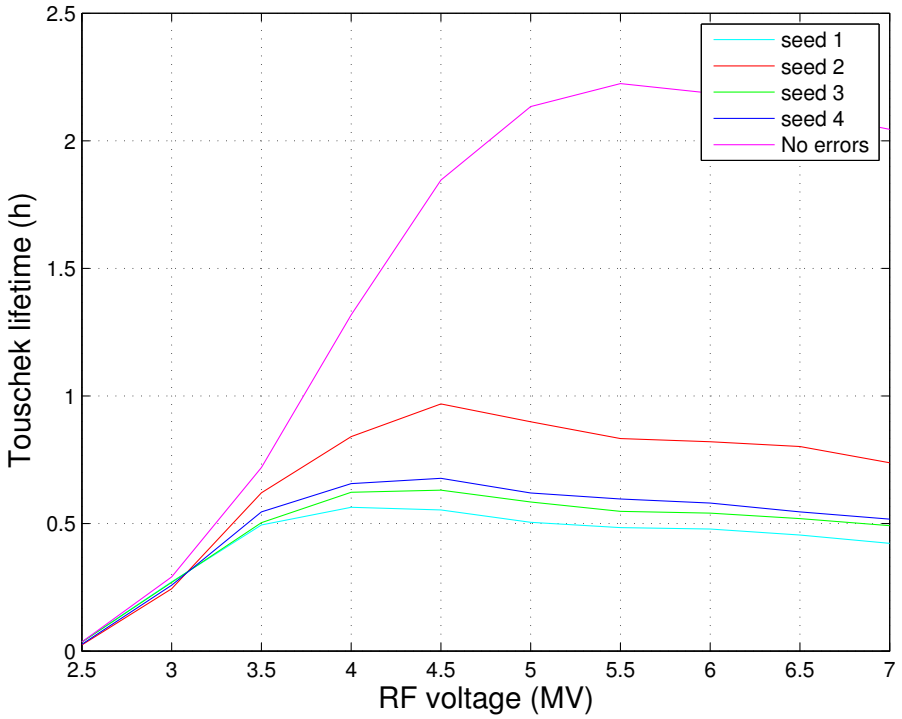

Figure 7.5: Touschek lifetime versus RF voltage in uniform multi-bunch mode, with 5.62 mA per bunch.

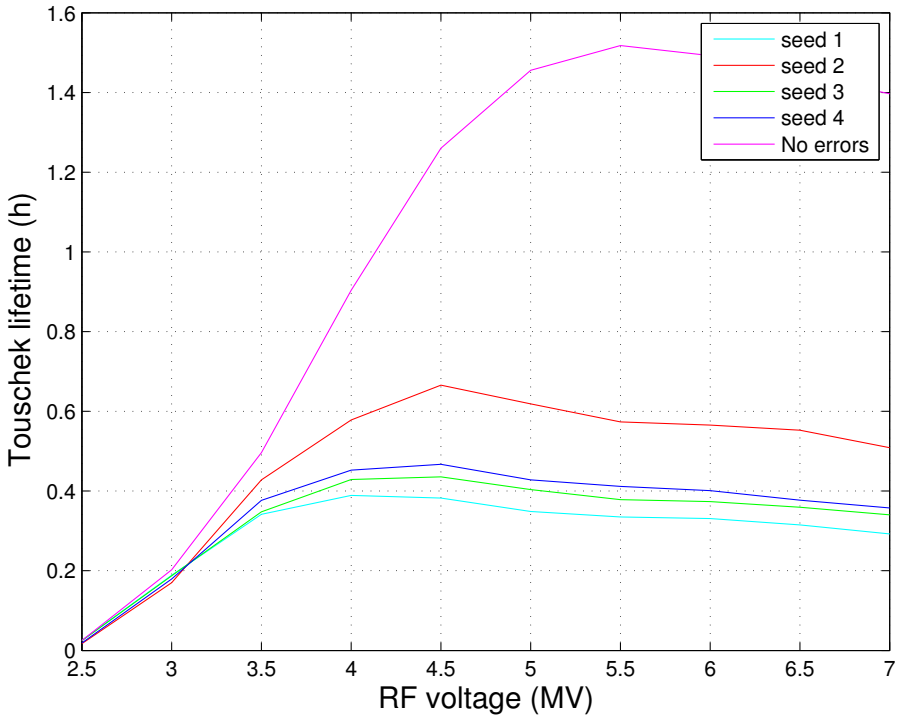

Figure 7.6: Touschek lifetime versus RF voltage in uniform multi-bunch mode, with 10 mA per bunch.

As a final parametric study, we compute the Touschek lifetime as a function of horizontal emittance. The results are shown in figure 7.7. The Touschek lifetime for various horizontal emittances has been computed, using the momentum acceptance of the S28 lattice with errors.

We are in the regime where the horizontal emittance growth increases the Touschek lifetime.

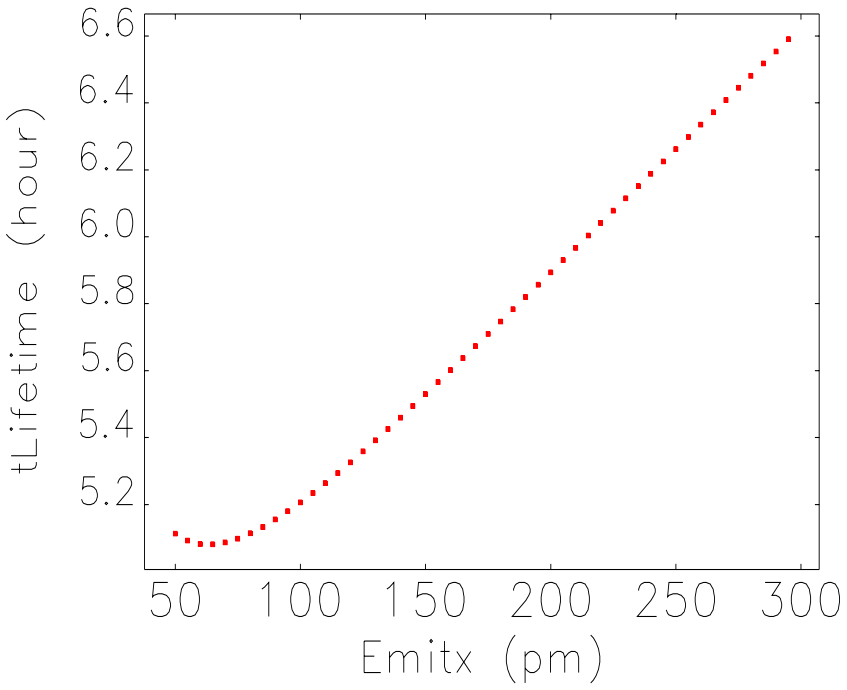

Figure 7.7: Touschek lifetime versus horizontal emittance, with constant vertical emittance of 5 pm. The minimum value is at 65 pm.

Conclusions

In this thesis a model able to predict the Touschek lifetime of the ESRF storage ring, including the momentum acceptance computation by particle tracking, has been presented.

In order to predict the Touschek lifetime, the RF voltage must be known within a small uncertainty. The calibration factor between the read-out value of the RF voltage and the real accelerating voltage given to the cavity has been measured, by measuring the synchrotron tune and the synchronous phase for various RF voltages. It was found to be approximately 0.95, although it was not consistent for all measurements.

From the synchrotron tune measurements, we have an indication that the momentum compaction factor of the machine is smaller than the value of the perfect machine, due to the effect of magnets alignment errors. Two possible measurements of the momentum compaction factor are presented and will be performed in next future.

The bunch length measurements, done for different RF voltages and currents, have been processed, in order to deduce the impedance of the vacuum chamber. A purely inductive impedance model (which may be derived from a broad-band resonator model), with an impedance $Z_n = 0.7\,\Omega$, agrees with bunch length measurements and it is used for the Touschek lifetime modeling.

The momentum acceptance simulation procedure has been defined. The size of the vacuum chamber is taken in account in the simulation. This is seen to be an important consideration which substantially impacts the momentum acceptance results.

The vacuum lifetime measurement procedure has been defined. The vacuum lifetime must be measured before all the Touschek lifetime measurements.

The effect of the spin polarization on the Touschek lifetime at ESRF has been studied. The polarization time has been measured ($\tau_p = 15.9 \pm 0.6\,\mathrm{min}$) and it agrees with the theoretical value. A depolarization procedure has been defined and it is now used before all Touschek lifetime measurements.

The spin depolarization has been studied also with a dedicated software, developed during the thesis work. Some measurements of the spin depolarization resonances, in order to measure the beam energy and the momentum compaction factor, have been tried and will be done in the future.

The Touschek lifetime for different currents and RF voltages has been measured and a good agreement between the simulations and the measurements has been found.

In order to confirm the momentum acceptance model with physical apertures, the Touschek lifetime varying the scrapers positions has been measured. A good agreement between the simulations and the measurements has been found.

An optimization of the sextupole setting, based on Touschek lifetime and dynamic aperture computation with tracking, has been performed. The algorithm used found a sextupole setting with both longer Touschek lifetime and larger dynamic aperture, and therefore a higher injection efficiency. With the sextupole setting found, the observed injection efficiency has been larger than the one with the nominal sextupole setting. The measured Touschek lifetime with the optimized sextupole setting disagreed with the simulation and it was slightly shorter than the one measured with the nominal setting. The reason of the disagreement is not clear, but probably the physical apertures model in the vertical plane and the linear and non-linear coupling are not perfect. A measurement of Touschek lifetime changing vertical scraper positions can be done in future. Other sextupole settings, more similar to the nominal one, can also be tried in the future.

In last chapters of the thesis, the Touschek lifetime of the new low emittance ESRF upgraded lattice has been studied. The bunch lengthening due to impedance has been computed for different operation modes and emittance growth due to intrabeam scattering has been studied. Touschek lifetimes for the four different modes that will be provided with the upgrade lattice have been studied, for different RF voltages, including emittance growth due to intrabeam scattering and bunch length due to impedance. It is found that an RF voltage between 4 MV and 4.5 MV may be optimal as far as lifetime considerations are concerned.

Appendix A

Overview of beam physics in electron storage rings

The motion of a charged particle in an electro-magnetic field is determined by the Lorentz force:

$$\frac{\mathrm{d}\vec{p}}{\mathrm{d}t} = e\left(\vec{E} + \vec{v} \times \vec{B}\right) \tag{A.1}$$

where $\vec{p}$ is the electron momentum, e is the electron charge, $\vec{E}$ is the electric field, $\vec{v}$ is the electron velocity and $\vec{B}$ is the magnetic field.

In circular electron storage rings, the magnetic field is used to guide the particles in the desired path, whereas the electric field is used to provide to the electrons the energy lost due to synchrotron radiation.

The reference trajectory of the electrons is defined by a succession of bending magnets and straight sections. In the bending magnets the magnetic field is uniform, aligned with the vertical direction. The motion of the electrons in the bending magnets is along an arc of a helix.

A particle with the exact momentum $\vec{p_0}$ travels along the reference trajectory, losing energy in dipoles and regaining it in the RF cavity. An electron storage ring is designed so that the particle motion is a small deviation from the reference trajectory.

A particle traveling in the reference trajectory is called the reference particle.

The phase space coordinate of a particle in a storage ring can be expressed with a 6 dimensional vector:

$$(x,\, x',\, y,\, y',\, ct,\, \delta) \tag{A.2}$$

where x and y are the horizontal and vertical deviation from the reference trajectory, $x' = \frac{\mathrm{d}x}{\mathrm{d}s}$ and $y' = \frac{\mathrm{d}y}{\mathrm{d}s}$ are the horizontal and vertical slopes with respect to the reference trajectory, s is the curvilinear coordinate along the reference trajectory, c

is the speed of light, t is the difference between the travel time of the particle and the one of the reference particle and $\delta = \mathrm{d}p/p_0$ is the fractional momentum deviation.

In this chapter, some basic concepts of particle accelerator physics are described.

In the first section, the linear and nonlinear dynamics of electrons in a storage ring, assuming no synchrotron radiation, are described. In the second section, the effects of synchrotron radiation and accelerating cavity are presented. In the third section, some relevant current dependent effects are shown: the bunch lengthening with current, the Touschek scattering and the intrabeam scattering. These phenomena are treated with more details in references [38], [7] and [11].

A.1 Linear and nonlinear dynamics

In a storage ring, the particle focusing is provided by quadrupole magnets. The magnetic field of a perfect quadrupole magnet is:

$$B_y(x) = g\,x \qquad\qquad B_x(y) = g\,y \tag{A.3}$$

where g is the quadrupole gradient. The quadrupole gradient is defined by:

$$g \equiv \frac{\partial B_y}{\partial x} = \frac{\partial B_x}{\partial y} \tag{A.4}$$

The quadrupole gradient can be normalized to the strength of the bending magnet field and therefore to the beam momentum. The quantity K_1 can be defined:

$$K_1 = \frac{g}{B\rho} \tag{A.5}$$

where $B\rho$ is the beam magnetic rigidity and it is given by:

$$B\rho\ [\mathrm{T\,m}] = \frac{p_0}{e} \simeq 3.33564 \cdot E_0\ [\mathrm{GeV}] \tag{A.6}$$

The basic structure of a storage ring is a sequence of dipoles, that are used to bend the trajectory, and quadrupoles, that are used to focus the beam. The sequence of dipoles and quadrupoles is the linear lattice of an accelerator.

The trajectory of a particle with exact nominal momentum in a storage ring with a periodic linear lattice is described by the equation of motion:

$$\frac{\mathrm{d}^2 w}{\mathrm{d}s^2} + K_w(s)\,w = 0 \tag{A.7}$$

where w is x or y, $K_w(s)$ is the focusing strength given by the quadrupoles and the dipoles and it is a function of the position around the ring. The periodicity of $K_w(s)$ is the length of the ring. $K_x(s)$ and $K_y(s)$ are given by:

$$K_x(s) = -\frac{1}{\rho^2(s)} - K_1(s) \tag{A.8}$$

$$K_y(s) = K_1(s) \tag{A.9}$$

The solution of the equation (A.7) is given by:

$$w(s) = a\sqrt{\beta_w(s)}\cos\left(\psi_w(s) + \psi_0\right) \tag{A.10}$$

where a and ψ_0 are constant given by the initial particle conditions. This is a pseudo-harmonic oscillation, called betatron oscillation, with varying amplitude $\sqrt{\beta_w}$. β also determines the wavelength of betatron oscillation.

$$\psi_w(s) = \int_{s_0}^{s} \frac{\mathrm{d}s}{\beta_w(s)} \tag{A.11}$$

The integral of the phase advance of the betatron oscillation in a complete turn around the ring is the betatron tune (ν_x and ν_y) of the ring.

$$\nu_w = \oint \frac{\mathrm{d}s}{\beta_w(s)} \tag{A.12}$$

β functions are defined by the linear lattice. Two other functions can be defined from the β: α and γ:

$$\alpha_w(s) = -\frac{1}{2}\frac{\mathrm{d}\beta_w(s)}{\mathrm{d}s} \qquad\qquad \gamma_w(s) = \frac{1+\alpha_w^2(s)}{\beta_w(s)} \tag{A.13}$$

Given a position in the ring, the phase space trajectory of a particle is an ellipse defined by:

$$\gamma_x x^2 + 2\alpha_x x x' + \beta_x x'^2 = 2J_x \tag{A.14}$$

$$\gamma_y y^2 + 2\alpha_y y y' + \beta_x y'^2 = 2J_y \tag{A.15}$$

where J_x and J_y are the horizontal action and the vertical action. For linear uncoupled motion, these quantities are invariant around the ring.

In figure A.1, the horizontal phase space ellipse is shown.

Two important quantities in electron storage rings can now be defined: the

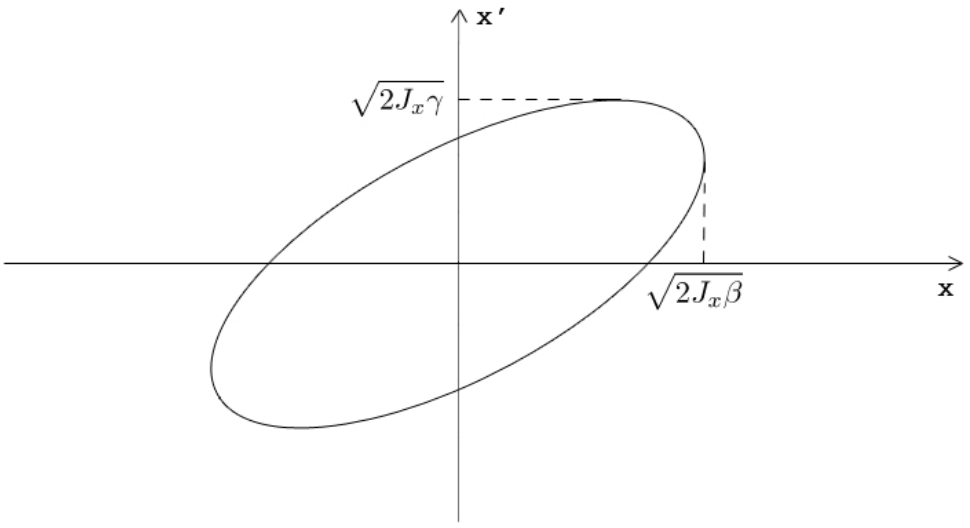

Figure A.1: Horizontal phase space ellipse.

horizontal and vertical emittances (ε_x and ε_y):

$$\varepsilon_x = \langle J_x \rangle \qquad\qquad \varepsilon_y = \langle J_y \rangle \tag{A.16}$$

where the average is on the particles of the beam. In this section, the horizontal and vertical motion are assumed to be uncoupled, so the averages are just over horizontal or vertical phase space, e.g.:

$$\langle J_x \rangle = \int \mathrm{d}x\mathrm{d}x' J_x\left(x, x'\right) \rho\left(x, x'\right) \tag{A.17}$$

where $\rho\left(x, x'\right)$ is the distribution of the electrons. The radiation damping and diffusion effects lead to a gaussian distribution, which is given by:

$$\rho(x, x') = \frac{1}{2\pi\varepsilon} \exp\left(-\frac{J_x}{\varepsilon}\right) = \frac{1}{2\pi\varepsilon} \exp\left(-\frac{\gamma x^2 + \alpha x x' + \beta x'^2}{2\varepsilon}\right) \tag{A.18}$$

Chromatic effects

Now the effect of a slightly different momentum of a particle is described. The particle beams in storage rings are not exactly monochromatic. This has several consequences.

First, the deflection of an electron with a different momentum in a magnetic field is different from the one of a particle with the nominal momentum.

This effect is captured by the dispersion function $D(s)$, which is defined by the

linear lattice. The function $\delta D(s)$ is the offset of the trajectory of a particle with relative momentum displacement δ from the reference path of particles with nominal momentum.

Second, the quadrupoles focusing effect for particles with wrong energy is also different. A particle with a higher energy will get a weaker focusing and so a smaller tune. The chromaticity is defined as the tune change per unit relative momentum change.

$$\xi_x = \frac{\mathrm{d}\nu_x}{\mathrm{d}\delta} \qquad\qquad \xi_y = \frac{\mathrm{d}\nu_y}{\mathrm{d}\delta} \tag{A.19}$$

The natural chromaticity is the chromaticity of the linear lattice, without corrections, and it is always negative for both horizontal and vertical planes. It can be computed with an integral around the ring:

$$\xi_{x,nat} = \frac{1}{4\pi} \oint \beta_x(s) K_x(s) \mathrm{d}s \tag{A.20}$$

$$\xi_{y,nat} = \frac{1}{4\pi} \oint \beta_y(s) K_y(s) \mathrm{d}s \tag{A.21}$$

To perform a chromaticity correction, a magnet with a focusing gradient which is a linear function of δ is needed. This can be achieved by using a sextupole magnet in a dispersive region.

The magnetic field of a perfect sextupole magnet is:

$$B_y(x,y) = \frac{1}{2} m \left(x^2 - y^2\right) \qquad\qquad B_x(x,y) = m\, x\, y \tag{A.22}$$

where m is the sextupole gradient, that is defined by:

$$m = \frac{\partial^2 B_y}{\partial x^2} \tag{A.23}$$

The sextupole gradient can be normalized to the magnetic rigidity of the beam. The quantity K_2 can be defined:

$$K_2 = \frac{m}{B\rho} \tag{A.24}$$

The quadrupole gradient of a perfect sextupole, as a function of horizontal position, is given by:

$$g(x) = \frac{\partial B_y}{\partial x} = m\, x \tag{A.25}$$

The horizontal position of a particle with a relative momentum displacement δ

is:

$$x(s,\delta) = x_\beta(s) + D(s)\delta \tag{A.26}$$

$$x'(s,\delta) = x'_\beta(s) + D'(s)\delta \tag{A.27}$$

where x_β is the betatron displacement of the particle, x'_β is the betatron slope of the particle and $D'(s)$ is the derivative of the dispersion function with respect to the position along the ring.

The focusing effect of a sextupole placed in a dispersive region, as a function of δ, is:

$$\Delta K_x(s) = K_2(s)D(s)\delta \qquad\qquad \Delta K_y(s) = -K_2(s)D(s)\delta \tag{A.28}$$

and so the value of the chromaticity with the correction can be computed with the integrals:

$$\xi_x = \frac{1}{4\pi}\oint \beta_x(s)\left[K_x(s) + K_2(s)D(s)\delta\right]\mathrm{d}s \tag{A.29}$$

$$\xi_y = \frac{1}{4\pi}\oint \beta_y(s)\left[K_y(s) - K_2(s)D(s)\delta\right]\mathrm{d}s \tag{A.30}$$

The horizontal and vertical actions can be written considering independently the betatron coordinate and the dispersive coordinate, using equations (A.14), (A.15), (A.26) and (A.27).

$$2J_x = \gamma_x x_\beta^2 + 2\alpha_x x_\beta x'_\beta + \beta_x x'^2_\beta + \mathcal{H}_x\delta^2 \tag{A.31}$$

where $\mathcal{H}_x$ is called the curly-H function. Its value is given by:

$$\mathcal{H}_x(s) = \gamma_x(s)D_x^2(s) + 2\alpha_x(s)D_x(s)D'_x(s) + \beta_x(s)D'^2_x(s) \tag{A.32}$$

Longitudinal motion

An ultrarelativistic electron in a storage ring emits synchrotron radiation. The instantaneous radiated power is given by:

$$P_\gamma = \frac{2}{3}r_e m_e c^3 \frac{\beta^4\gamma^4}{\rho^2} \tag{A.33}$$

where r_e is the classical electron radius, m_e is the electron mass, c is the speed of light, β and γ are the relativistic factors, ρ is the bending radius.

The integral of the instantaneous radiated power in a revolution time is the

energy loss per turn. Its value is given by:

$$U_0 = \oint P_\gamma \mathrm{d}t = \frac{2}{3} r_e m_e c^2 \beta^3 \gamma^4 \oint \frac{\mathrm{d}s}{\rho^2} \tag{A.34}$$

The energy loss must be compensated by an accelerating element: the radio frequency cavity. The frequency of the cavity must be a harmonic of the beam revolution frequency. The voltage applied to the cavity is:

$$V = V_{RF} \sin\left(h\omega_0 t + \phi_s\right) \tag{A.35}$$

where V_{RF} is the peak value of the RF cavity voltage, h is the harmonic number, $\omega_0 = 2\pi f_0 = 2\pi \frac{\beta c}{C}$ is the revolution angular frequency, C is the ring length, ϕ_s is the synchronous phase and t is the difference between the travel time of the particle and the one of the reference particle.

The synchronous phase has the value such that the average energy given to the beam is the energy loss per turn:

$$\Delta E = e V_{RF} \sin \phi_s = U_0 \tag{A.36}$$

where e is the electron charge.

Two quantities are useful to understand the longitudinal motion of the electrons in a storage ring: the momentum compaction factor α and the phase-slip factor η.

The momentum compaction factor is the variation of path length with relative momentum deviation and it is given by:

$$\alpha = \frac{\mathrm{d}C/C}{\delta} \tag{A.37}$$

The momentum compaction factor is a geometric factor, related with the dispersion function:

$$\alpha = \frac{1}{C} I_1 \tag{A.38}$$

where I_1 is the first synchrotron radiation integral:

$$I_1 = \oint \frac{D(s)}{\rho} \mathrm{d}s \tag{A.39}$$

The phase-slip factor η is the relation between the revolution period of a particle and its relative momentum variation. The revolution time changes due to the lengthening of the trajectory when the momentum is increased and due to the change in

the particle velocity. The second effect is negligible in an ultrarelativistic regime.

$$\eta = \frac{\mathrm{d}f/f}{\delta} = \frac{1}{\gamma^2} - \alpha \tag{A.40}$$

The momentum compaction factor is usually positive. The phase-slip factor can be negative or positive. In an ultrarelativistic electron storage ring, it is negative, because the change in electron velocity is negligible. The transition energy is the energy such that the phase-slip factor changes the sign:

$$\gamma_t = \frac{1}{\sqrt{\alpha}} \tag{A.41}$$

A particle with a slightly larger momentum will do a revolution in a longer time (or shorter if $\gamma < \gamma_t$) than the nominal revolution period. This particle will arrive later to the cavity and will receive a smaller acceleration. This effect causes an oscillation in momentum and in phase respect to the cavity. The longitudinal oscillation is called synchrotron oscillation.

$$\ddot{\phi} + \Omega_s^2 \phi = 0 \tag{A.42}$$

where Ω_s is the synchrotron frequency and ϕ is the phase distance with the synchronous phase. Its value is given by:

$$\phi = h\,\omega_0\,t \tag{A.43}$$

The synchrotron angular frequency has this value:

$$\Omega_s = \omega_0\,\nu_s = \omega_0 \sqrt{\frac{heV_{RF}\eta\cos\phi_s}{2\pi\beta^2 E_0}} \tag{A.44}$$

where h is the harmonic number, e is the electron charge, η is the phase-slip factor, ϕ_s is the synchronous phase, β is the relativistic factor, E_0 is the electron energy. ν_s is called synchrotron tune.

In analogy with the transverse case, a longitudinal β function can be defined:

$$\beta_z = \frac{C\,\alpha}{2\pi\nu_s} \tag{A.45}$$

where C is the ring circumference, α is the momentum compaction factor and ν_s is the synchrotron tune.

The longitudinal action J_z and the longitudinal emittance ε_z can also be defined:

$$2J_z = \frac{1}{\beta_z}(ct)^2 + \beta_z \delta^2 \tag{A.46}$$

$$\varepsilon_z = \langle J_z \rangle \tag{A.47}$$

Also in the longitudinal direction, the beam is gaussian (ignoring potential well effects, considered later) in the same form of equation (A.18).

A.2 Equilibrium beam sizes with radiation

As written in the previous section, electrons perform longitudinal (or synchrotron) oscillations and transverse (or betatron) oscillations. In this section, the damping and diffusion effects from radiation are presented. These effects cause the achievement of the equilibrium emittances.

The derivative of the emittances with respect to the time has two components: the damping and the diffusion. A general equation can be written:

$$\frac{\mathrm{d}\varepsilon_w}{\mathrm{d}t} = -\frac{2}{\tau_w}\varepsilon_w + d_w \tag{A.48}$$

where w can be x, y or z, τ_w are the horizontal, vertical and longitudinal damping times and d_w are the diffusion terms.

The equilibrium emittance is obtained when the damping effect is opposite to the diffusion effect, i.e. when the emittance variation is zero:

$$\varepsilon_w = d_w \frac{\tau_w}{2} \tag{A.49}$$

In first part of this section, the longitudinal damping time and diffusion term will be derived. In the next part of this section the transverse damping and diffusion will be treated.

Electrons lose energy due to synchrotron radiation and the energy is restored by the RF cavity. The energy loss per turn is larger for higher energy particles in the bunch. This effect causes a damping of the longitudinal oscillations. The damping time is proportional to the derivative of the energy loss per turn with respect to the particle energy:

$$\tau_z^{-1} = \frac{1}{2T_0}\frac{\mathrm{d}U_0}{\mathrm{d}E}\bigg|_{E=E_0} \tag{A.50}$$

where T_0 is the revolution time period, U_0 is the energy loss in one turn, given in equation (A.34), E is the energy of the particle, E_0 is the nominal energy of the

particle.

In order to compute the derivative of the energy loss per turn with respect to the electron energy, one can integrate the radiative power of equation (A.33) with respect to the time, considering the path lengthening with energy deviation.

The longitudinal damping time can be expressed by:

$$\tau_z = \frac{2}{j_z}\frac{E_0}{U_0}T_0 \tag{A.51}$$

where j_z is the longitudinal damping partition number, and it is given by:

$$j_z = 2 + \frac{I_4}{I_2} \tag{A.52}$$

where I_2 and I_4 are the second and fourth synchrotron radiation integrals:

$$I_2 = \oint \frac{1}{\rho^2(s)}\mathrm{d}s \qquad\qquad I_4 = \oint \frac{D_x(s)}{\rho(s)}\left(\frac{1}{\rho^2(s)} + 2k_1(s)\right)\mathrm{d}s \tag{A.53}$$

If the synchrotron radiation were a classical process, the longitudinal action of the electrons, and therefore the longitudinal emittance, would damp to zero.

The radiation is a quantum effect. The energy of the emitted photons is some orders of magnitude smaller than the electrons energy. The photon emission is a random process and the number of photons per unit time satisfies a Poisson distribution.

The quantization of the photons gives a noise to the beam energy. The effect of the noise is to increase the energy spread.

The emission of a photon with energy u changes the longitudinal action of the electron:

$$\Delta J_z = \frac{\beta_z}{2}\left(u^2 - 2u\delta\right) \tag{A.54}$$

Considering that the photon emission is a random effect, during the emission, δ, and therefore ΔJ_z, can be positive or negative. The average in a bunch of the variation of J_z in a turn is positive. The longitudinal emittance increases with time due to this effect.

The longitudinal emittance variation with respect to the time due to quantum excitation is given by:

$$\left.\frac{\mathrm{d}\varepsilon_z}{\mathrm{d}t}\right|_{qe} = \beta_z \frac{55}{32\sqrt{3}}\frac{\hbar}{m_e c}\gamma^2 \frac{2}{j_z \tau_z}\frac{I_3}{I_2} \tag{A.55}$$

where I_3 is the third synchrotron radiation integral and it is given by:

$$I_3 = \oint \frac{1}{|\rho^3(s)|} \mathrm{d}s \tag{A.56}$$

The longitudinal emittance reaches an equilibrium when damping and diffusion due to quantum excitation have the same value, with opposite sign.

$$\frac{\mathrm{d}\varepsilon_z}{\mathrm{d}t} = \left.\frac{\mathrm{d}\varepsilon_z}{\mathrm{d}t}\right|_{qe} - \frac{2}{\tau_z}\varepsilon_z = 0 \tag{A.57}$$

$$\varepsilon_z = \left.\frac{\mathrm{d}\varepsilon_z}{\mathrm{d}t}\right|_{qe} \cdot \frac{\tau_z}{2} = \beta_z \frac{55}{32\sqrt{3}} \frac{\hbar}{m_e c} \gamma^2 \frac{I_3}{j_z I_2} \tag{A.58}$$

The equilibrium energy spread is given by:

$$\sigma_\delta^2 = \frac{\varepsilon_z}{\beta_z} = \frac{55}{32\sqrt{3}} \frac{\hbar}{m_e c} \gamma^2 \frac{I_3}{j_z I_2} \tag{A.59}$$

The bunch length is related to the energy spread and it is given by:

$$\sigma_z = \frac{C\alpha}{2\pi\nu_s}\sigma_\delta \tag{A.60}$$

The synchrotron radiation and the RF cavity cause also a damping of the betatron oscillations.

The radiation is emitted in a cone with a small angle $1/\gamma$ with respect to the velocity. The electric field of the accelerating cavity is longitudinal. A fraction of the transverse momentum is given to the emitted photon and the cavity provide to the electrons only longitudinal momentum.

At each emitted photon, the vertical electron action is reduced. The effect on the horizontal action is more complicated, because horizontal motion is strongly coupled with longitudinal motion due to the dispersion.

The vertical damping time is given by:

$$\tau_y = 2\frac{E_0}{U_0} T_0 \tag{A.61}$$

The horizontal damping time is given by:

$$\tau_x = \frac{2}{j_x}\frac{E_0}{U_0} T_0 \tag{A.62}$$

where j_x is the horizontal damping partition number and it is given by:

$$j_x = 2 - \frac{I_4}{I_2} \tag{A.63}$$

The diffusion of longitudinal emittance due to quantum excitation causes a diffusion of transverse emittances, because the longitudinal motion is coupled with the transverse motion.

The horizontal diffusion term is given by:

$$d_x = \frac{2}{j_x \tau_x} \frac{55}{32\sqrt{3}} \frac{\hbar}{m_e c} \gamma^2 \frac{I_5}{I_2} \tag{A.64}$$

and the derivative of the horizontal emittance with respect to the time is given by:

$$\frac{\mathrm{d}\varepsilon_x}{\mathrm{d}t} = -\frac{2}{\tau_x}\varepsilon_x + d_x \tag{A.65}$$

where τ_x is the horizontal damping time, j_x is the horizontal damping partition number, $\hbar$ is the reduced planck constant, m_e is the electron mass, c is the speed of light, γ is the Lorentz relativistic factor, I_2 and I_5 are the second and the fifth synchrotron radiation integrals. I_5 is given by:

$$I_5 = \oint \frac{\mathcal{H}_x(s)}{|\rho^3(s)|} \mathrm{d}s \tag{A.66}$$

$\mathcal{H}_x(s)$ is the horizontal curly-H function, defined in equation (A.32).

The equilibrium is reached when the damping effect is equal to the quantum excitation:

$$\varepsilon_x = \frac{1}{j_x} \frac{55}{32\sqrt{3}} \frac{\hbar}{m_e c} \gamma^2 \frac{I_5}{I_2} \tag{A.67}$$

A small horizontal emittance can be achieved with a lattice where I_5 is minimized, i.e. where the curly-H function is small in the bending magnets.

In a planar storage rings, without vertical bending magnets, the vertical dispersion function is zero. Nevertheless, in real storage rings, the vertical dispersion function is not zero, because vertical misalignments of quadrupoles give vertical kicks to the beam and vertical dispersion. A vertical curly-H function can be defined and the equilibrium vertical emittance can be computed. Vertical emittance is typically some orders of magnitude smaller than the horizontal one.

We have treated the uncoupled case in this section. The effect of x-y coupling is to make the invariant action a combination of horizontal and vertical. We note, however, that an emittance evolution equation of the form of (A.49) still holds.

A.3 Current dependent effects

When the current of the beam is increased, some collective effects are no longer negligible, which can change the beam sizes from those given in previous section.

Here two effects are presented: the interactions of the electrons with the beam pipe (bunch length through the impedance) and the intrabeam scattering. Another collective effect, the Touschek scattering, is presented in chapter 1.

A relativistic particle inside a conductive vacuum chamber creates a longitudinal electric field, the longitudinal wakefield, that accelerates other particles of the beam. This effect causes the lengthening of the bunch and it may also cause instabilities and other bunch distortions. The intrabeam scattering is a multi-particle scattering that increases the size of the bunch transversally and longitudinally.

A.3.1 Longitudinal wakefield and bunch lengthening

Considering a particle traveling in the accelerator, the longitudinal accelerating voltage seen by a test charge at a fixed distance to the particle with charge q, per unit of charge, can be written:

$$W_{\parallel} = -\frac{1}{q}\oint E_{\parallel}\left(s, t = \frac{s}{\beta c} + \tau\right) \mathrm{d}s \tag{A.68}$$

where $E_{\parallel}$ cannot be computed analytically, but it can be estimated numerically with dedicated software. This is called wake function. The value depends on the shape and material of the vacuum chamber and other elements the beam encounters on its circuit.

The total accelerating voltage seen by a particle in the bunch can be obtained convolving the single particle wake function with the bunch linear density $\lambda(\tau)$:

$$V(\tau) = -Q\int_{-\infty}^{+\infty} W\left(\tau - \tau'\right)\lambda\left(\tau'\right)\mathrm{d}\tau' \tag{A.69}$$

where Q is the total bunch charge and the bunch linear density is normalized to 1:

$$\int_{-\infty}^{+\infty} \lambda(t)\mathrm{d}t = 1 \tag{A.70}$$

The Fourier transformations of $W_{\parallel}(\tau)$ and $\lambda(\tau)$ are given by:

$$Z_{\parallel}(\omega) = \int_{-\infty}^{+\infty} W_{\parallel}(\tau)e^{-i\omega\tau}\mathrm{d}\tau \tag{A.71}$$

and

$$I(\omega) = Q \int_{-\infty}^{+\infty} \lambda(\tau) e^{-i\omega\tau} \mathrm{d}\tau \tag{A.72}$$

In frequency domain, the convolution become a product:

$$V(\omega) = -I(\omega)\, Z_{\parallel}(\omega) \tag{A.73}$$

$Z_{\parallel}(\omega)$ is called the longitudinal impedance.

A model often used to describe the impedance of an accelerator is a broad band resonator with low quality factor Q, typically $Q = 1$. The impedance can be expressed as a function of the shunt impedance R_S, the resonance frequency ω_r and the quality factor Q.

$$Z_{\parallel}(\omega) = \frac{R_S}{1 + iQ\,(\omega_r/\omega - \omega/\omega_r)} \tag{A.74}$$

A quantity of interest for the longitudinal instabilities is $Z_{\parallel}(\omega)/\omega$, and in particular its limit when $\omega \to 0$.

$$Z_n = -\mathrm{Im}\left[\lim_{\omega\to 0} \frac{Z_{\parallel}(\omega)}{\omega}\right] = \frac{R_S}{\omega_r\, Q} \tag{A.75}$$

A simpler model used to compute the bunch lengthening effect is a purely inductive impedance.

Given a wakefield, the Haissinski equation describes the bunch lengthening. The Haissinki equation is given by [11]:

$$\lambda(\tau) = K \exp\left[-U_0(\tau) - \xi \int_{-\infty}^{\tau} \mathrm{d}t\, V(t)\right] \tag{A.76}$$

where K is a normalization constant defined in order to have:

$$\int_{-\infty}^{+\infty} \lambda(t)\mathrm{d}t = 1 \tag{A.77}$$

$U_0(\tau)$ is the parabolic potential due to the linearization of the RF accelerating voltage:

$$U_0(\tau) = \frac{\tau^2}{2\sigma_z^2} \tag{A.78}$$

ξ is a constant defined by:

$$\xi = \frac{2\pi I_b}{h V_{RF} \cos\phi_s} \tag{A.79}$$

The effect of an impedance can be computed solving numerically the Haissinski equation [39]. This is done for example in the `haissinski` module of `elegant` [31].

An impedance model is required for the input to compute the distribution.

An example of the bunch lengthening effect from this code is shown in figure A.2, with the resultant bunch density and wake function for bunch current of 5.75 mA and an inductive impedance of $Z_n = 1.4\,\Omega$.

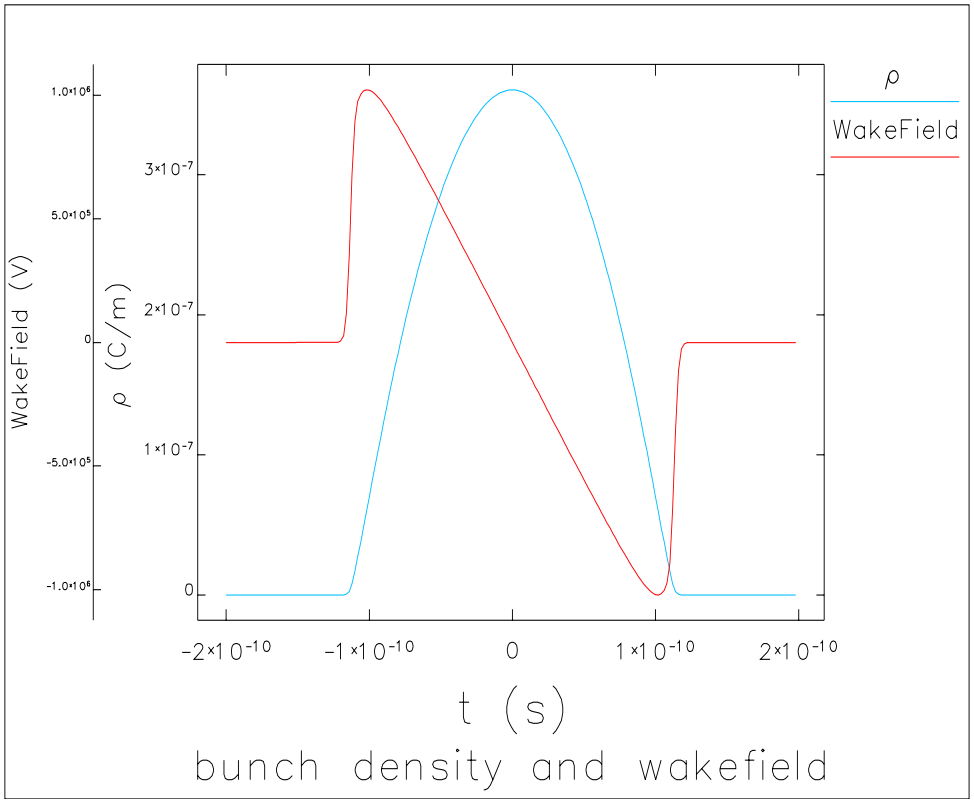

Figure A.2: Equilbrium bunch density and wake function from `haissinski` module using a purely inductive impedance.

In addition to fully solving the Haissinski equation, a simple analytical expression exists when the impedance is inductive. In particular, the bunch length is given by this formula [40] [29]:

$$\left(\frac{\sigma_z}{\sigma_{z_0}}\right)^3 - \left(\frac{\sigma_z}{\sigma_{z_0}}\right) = \frac{\Delta}{4\sqrt{\pi}} \tag{A.80}$$

Here σ_z is the increased bunch length and σ_{z_0} is the zero current bunch length. The parameter Δ is given by:

$$\Delta = -\frac{2\pi I_b Z_n}{V_{RF} h \cos\phi_s \left(\frac{\alpha\sigma_\delta}{\nu_s}\right)^3} \tag{A.81}$$

where I_b is the bunch current, Z_n is the inductive impedance, V_{RF} is the maximum RF voltage, h is the harmonic number, ϕ_s is the synchronous phase, α is the momentum compaction factor, σ_δ is the energy spread and ν_s is the synchrotron

tune.

The synchronous phase is given by:

$$\phi_s = \pi - \arcsin\left(\frac{U_0}{eV_{RF}}\right) \tag{A.82}$$

where U_0 is the energy loss per turn and e is the charge of an electron.

The zero current synchrotron tune is given by (see equation A.44):

$$\nu_s = \sqrt{-\frac{eV_{rf}}{E_0}\frac{h\alpha}{2\pi}\cos\phi_s} \tag{A.83}$$

where E_0 is the electron energy.

The zero current bunch length may be related to the energy spread via equation A.60:

$$\sigma_{z_0} = \frac{C\alpha}{2\pi\nu_s}\sigma_\delta \tag{A.84}$$

where C is the machine circumference.

Given these expressions, one can show that Δ may also be written (as given in [40])

$$\Delta = \frac{\alpha e I_b}{E_0\nu_s^2}\left(\frac{c}{\omega_0\sigma_{z0}}\right)^3 Z_n \tag{A.85}$$

where c is the speed of light and ω_0 is the revolution angular frequency ($\omega_0 = 2\pi\frac{c}{C}$).

The cubic equation (A.80) has three solutions, one of which is real, and is as follows:

$$\left(\frac{\sigma_z}{\sigma_{z_0}}\right) = \frac{\sqrt[3]{\sqrt{3}\sqrt{27Q^2-4}+9Q}}{\sqrt[3]{18}} + \frac{\sqrt[3]{\frac{2}{3}}}{\sqrt[3]{\sqrt{3}\sqrt{27Q^2-4}+9Q}} \tag{A.86}$$

with $Q = \frac{\Delta}{4\sqrt{\pi}}$.

A plot of this solution is given in figure A.3.

A.3.2 Intrabeam scattering

The next effect considered is the intrabeam scattering, in which multiple scattering of the electrons off each other result in a growth of the beam sizes.

The IBS growth rate is defined as:

$$\frac{1}{T_a} = \frac{1}{\varepsilon_a}\left(\frac{\mathrm{d}\varepsilon_a}{\mathrm{d}t}\right)_{\text{IBS}} \tag{A.87}$$

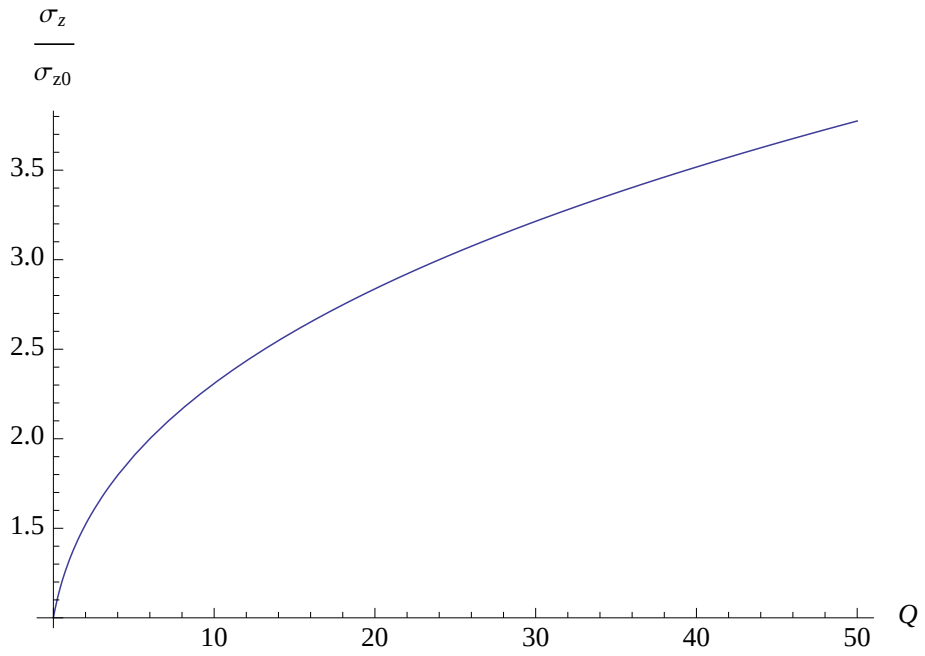

Figure A.3: Growth in bunch length versus Q. For $V_{rf} = 8\,\mathrm{MV}$, $Z_n = 0.7\,\Omega$ and the beam parameters of the ESRF storage ring, $Q = 2.347 \cdot I_b[\mathrm{mA}]$.

where the ε_a $(a = 1, 2, 3)$ are the horizontal, vertical and longitudinal emittances.

Given the beam distribution, one may compute the IBS growth rates. The damping and diffusion from synchrotron radiation will push the beam towards its equilibrium values, and a new equilibrium will be established. In particular, the emittance evolves in time according to

$$\frac{d\varepsilon_a}{dt} = -\frac{2}{\tau_a}(\varepsilon_a - \varepsilon_{a0}) + \frac{\varepsilon_a}{T_a} \tag{A.88}$$

where the τ_a are the synchrotron radiation damping times, the ε_{a0} are the equilibrium eigenemittances due only to radiation damping and diffusion.

We solve equation (A.88) using two different codes: `IBSEmittance` module associated with the `Elegant` code and a `mathematica` code written by T. Demma [41]. `Elegant` computes the growth rates using the formulae of Bjorken and Mtingwa [42]. The code of T. Demma uses a simplified version of Bane's high energy approximation (see [43]).

Equation (A.88) implies that at the equilibrium the growth rates are related to the emittance change by:

$$\frac{1}{T_a} = \frac{2}{\tau_a}\frac{\Delta\varepsilon_a}{\varepsilon_a} \tag{A.89}$$

Appendix B

Spin depolarization code

A simple code able to simulate the process of spin depolarization in an electron storage ring has been written. The code is written in `matlab` and it is interfaced to the user with a `python` script.

The code can track the spin vector of many particles for a given number of turns. A kicker in a certain position of the ring can be placed and the depolarization of the bunch can be simulated, varying the signal given to the kicker.

Since the depolarization time can be order of few seconds, i.e. million of turns in the ESRF storage ring, and since the particles to be simulated are order of 100, the code must be used in a cluster where some hundreds of processor's cores can be used.

The spin of a single electron is modeled as a point in a sphere, with two angle coordinates: θ and ϕ.

The effect on the spin of a single particle of a turn in the storage ring is modeled as a rotation of the spin vector around the vertical axis by an angle θ_z:

$$\theta_z = 2\pi\,\nu_{spin} \tag{B.1}$$

where $\nu_{spin} = a\gamma$ is the spin tune and a is the anomalous electron magnetic moment (see section 2.1). The effect on the spin of a vertical kicker, from a horizontal magnetic field, is modeled as a rotation around horizontal direction of an angle θ_x:

$$\theta_x = 2\pi\nu_{spin}\theta_{kicker} \tag{B.2}$$

where θ_{kicker} is the kick angle given to the electron from the kicker.

The transverse phase space coordinates of the electrons are not tracked in this code. The energy of the electron, which determines the spin tune, performs the synchrotron oscillations.

The signal given to the kicker can be chosen between a single sinusoid or a frequency modulated signal, between a given range of frequencies.

The value of the vertical polarization is defined as the average of the vertical component of the spins of the bunch of electrons. The number of particles to be simulated can be chosen by the user. After some tests, 100 particles have been chosen.

The code allows to switch on and off the synchrotron oscillations and the energy spread of the particles.

The initial value of the vertical polarization P can be chosen. The spin distribution can be chosen between two:

- the spins are all up or down, without horizontal and longitudinal component, and the average of the vectors is P;
- the vertical component of the spin is P for each electrons and the azimuthal angle is randomly distributed between 0 and 2π.

The vertical polarization as a function of time and of frequency of the signal given to the kicker can be produced by the simulation code.

In figure B.1 the depolarization resonance is shown, in case with synchrotron oscillations. The kicker signal is a sinusoid with constant frequency. Each point represents the final polarization of the bunch after 1 million turns.

In figure B.2, the resonance of the fourth synchrotron side band is shown, in case with synchrotron oscillations.

The code allows also to see the polarization level during the tracking process. In figure B.3, the polarization versus number of turns is shown for some different fixed frequencies of the kicker.

In figure B.4, the spin depolarization resonance is shown in case without synchrotron oscillations. The resonance size is comparable with the tune spread due to the energy spread. The spread in the spin tune can be computed as follows:

$$\Delta\nu_{spin} = \sigma\delta \cdot \nu_{spin0} \simeq 1.3 \cdot 10^{-2} \tag{B.3}$$

A complete depolarization procedure has been also simulated, in order to compare the simulation with the experiments.

Using the procedure found experimentally, we are not able to have a complete depolarization with the simulation. In figure B.5, the polarization versus the number of turns is shown with frequency scanned from 249 kHz to 253 kHz, using a kicker strength of 10 μrad instead of the one found in the experiment, which was 1 μrad.

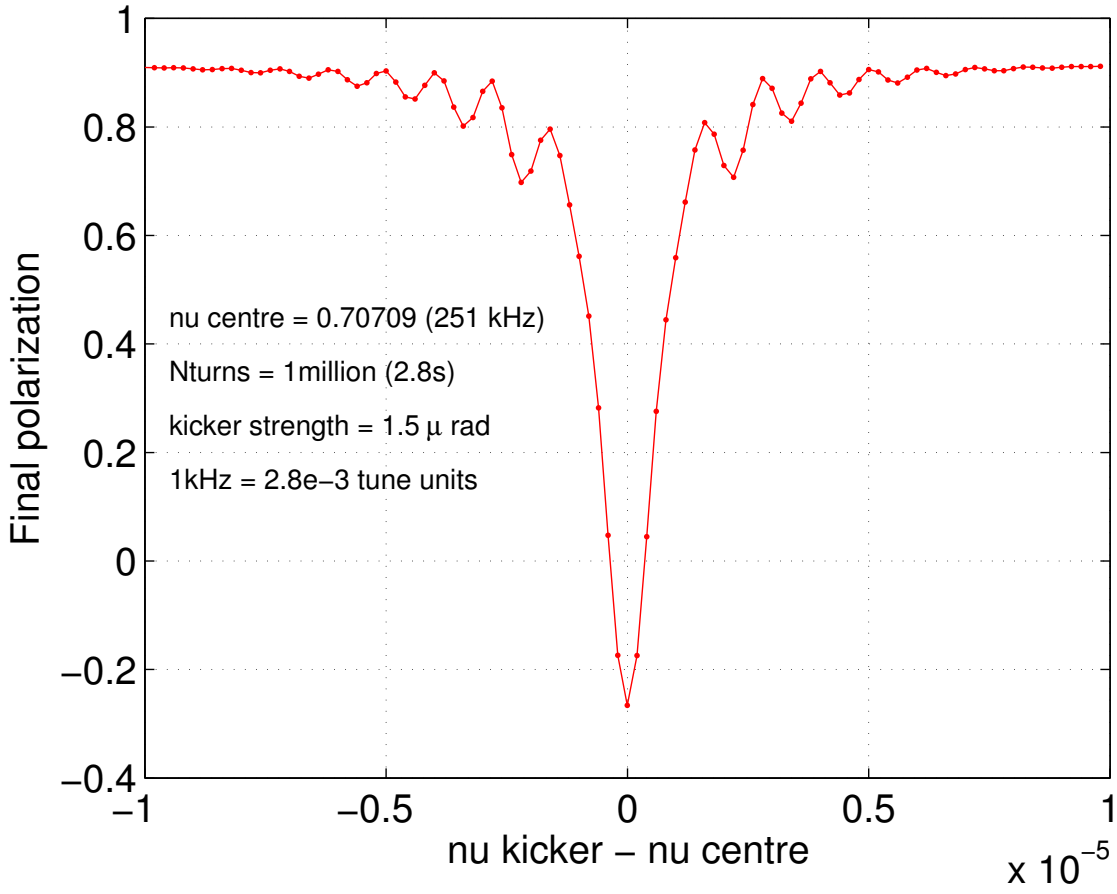

Figure B.1: Main spin depolarization resonance. The kicker strength is 1.5 μrad, the frequency is kept constant for 1 million turns. The initial polarization is 92 %, which is the Sokolov-Ternov level.

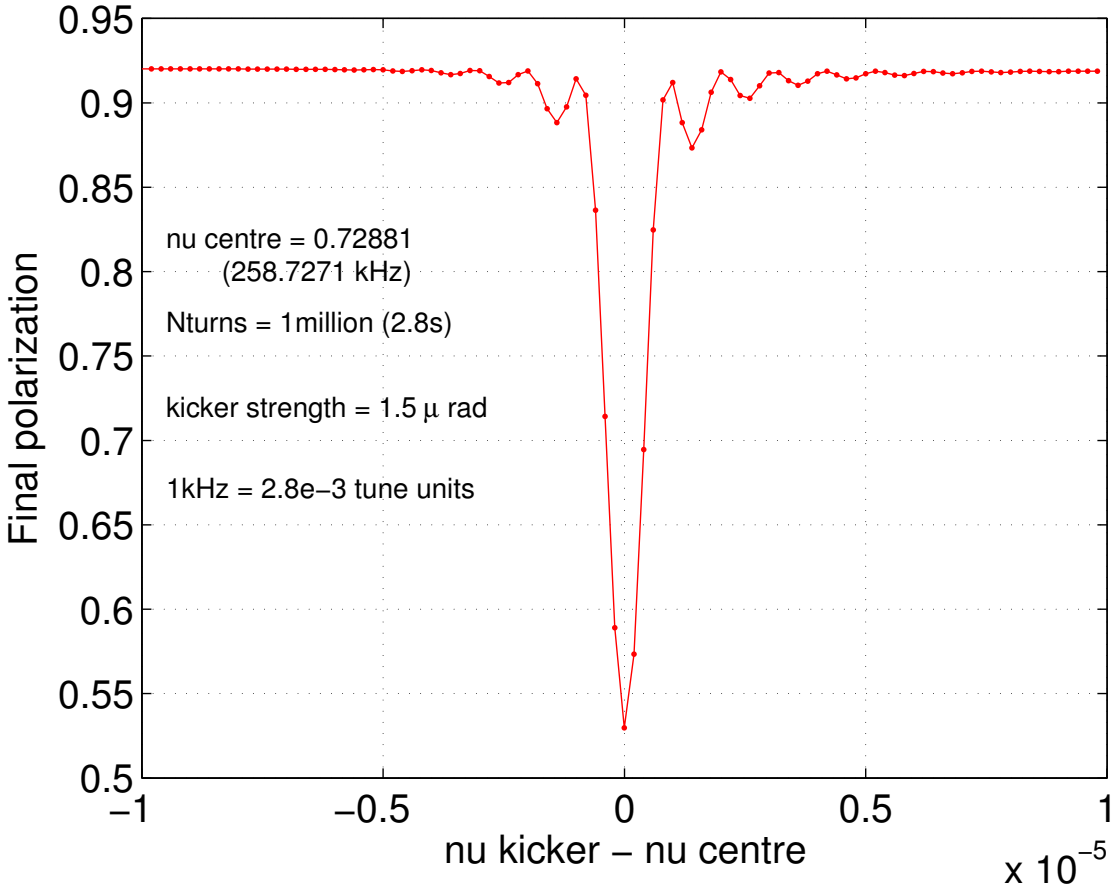

Figure B.2: Fourth synchrotron side band of the spin depolarization resonance. The kicker strength is 1.5 μrad, the frequency is kept constant for 1 million turns. The initial polarization is 0.92%, which is the Sokolov-Ternov level.

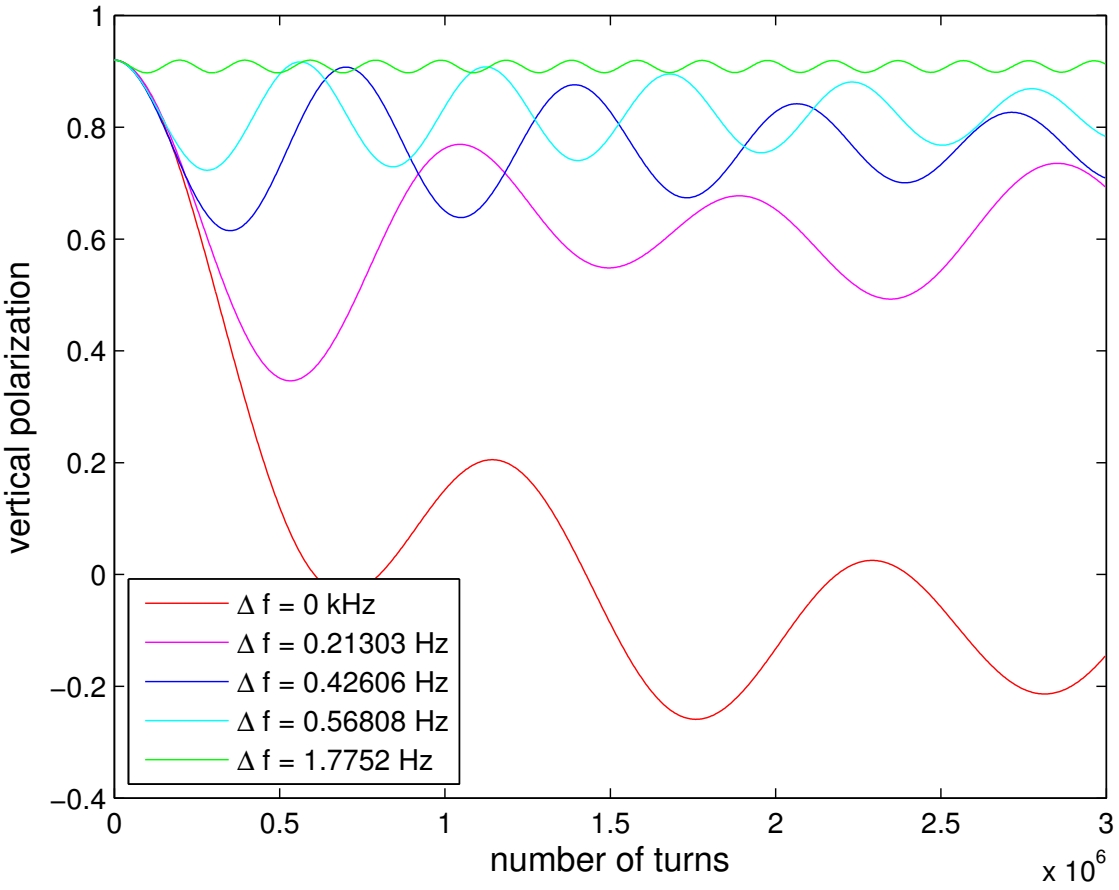

Figure B.3: Polarization versus number of turns for different kicker frequencies. The kicker strength is 0.85 μrad.

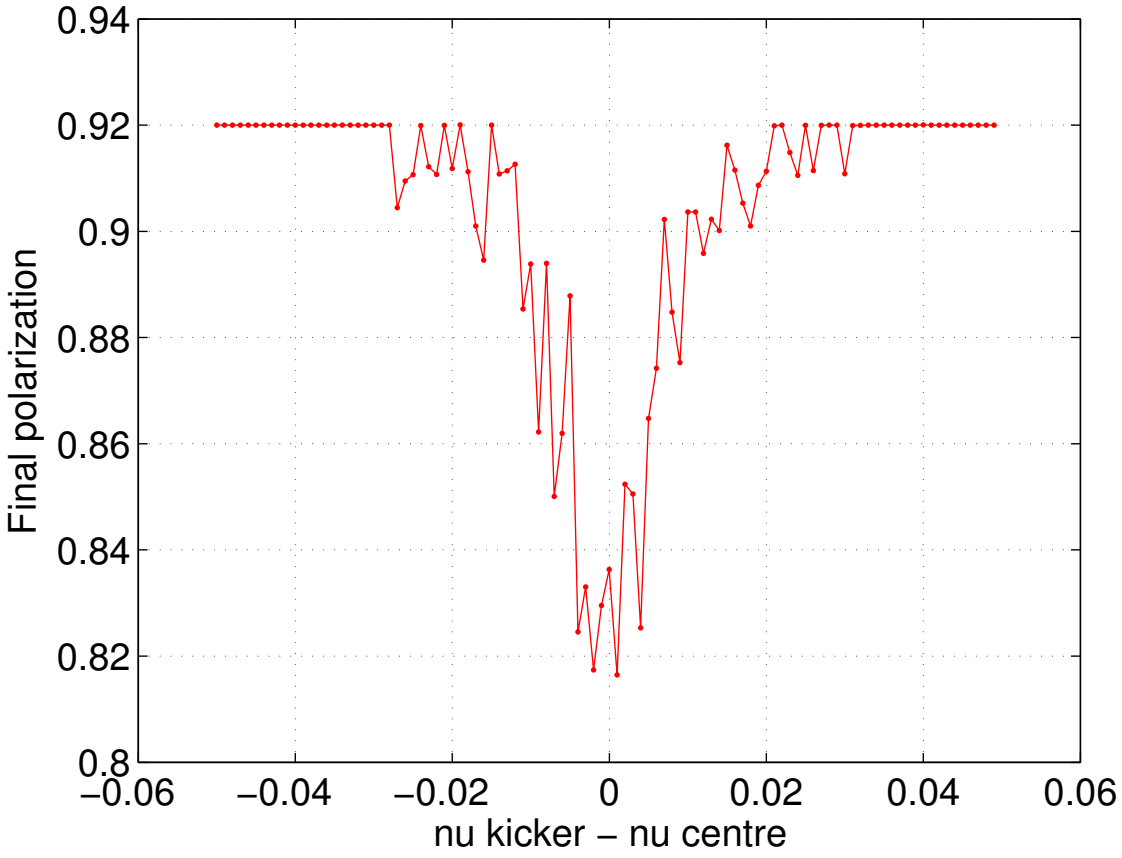

Figure B.4: Main spin depolarization resonance in case without synchrotron oscillations. The kicker strength is 15 μrad in this case, in order to have a faster depolarization. The frequency is varied between 238 kHz and 264 kHz, in 100 steps of about 260 Hz. For each step, the frequency is varied linearly in the range in 1 million turns.

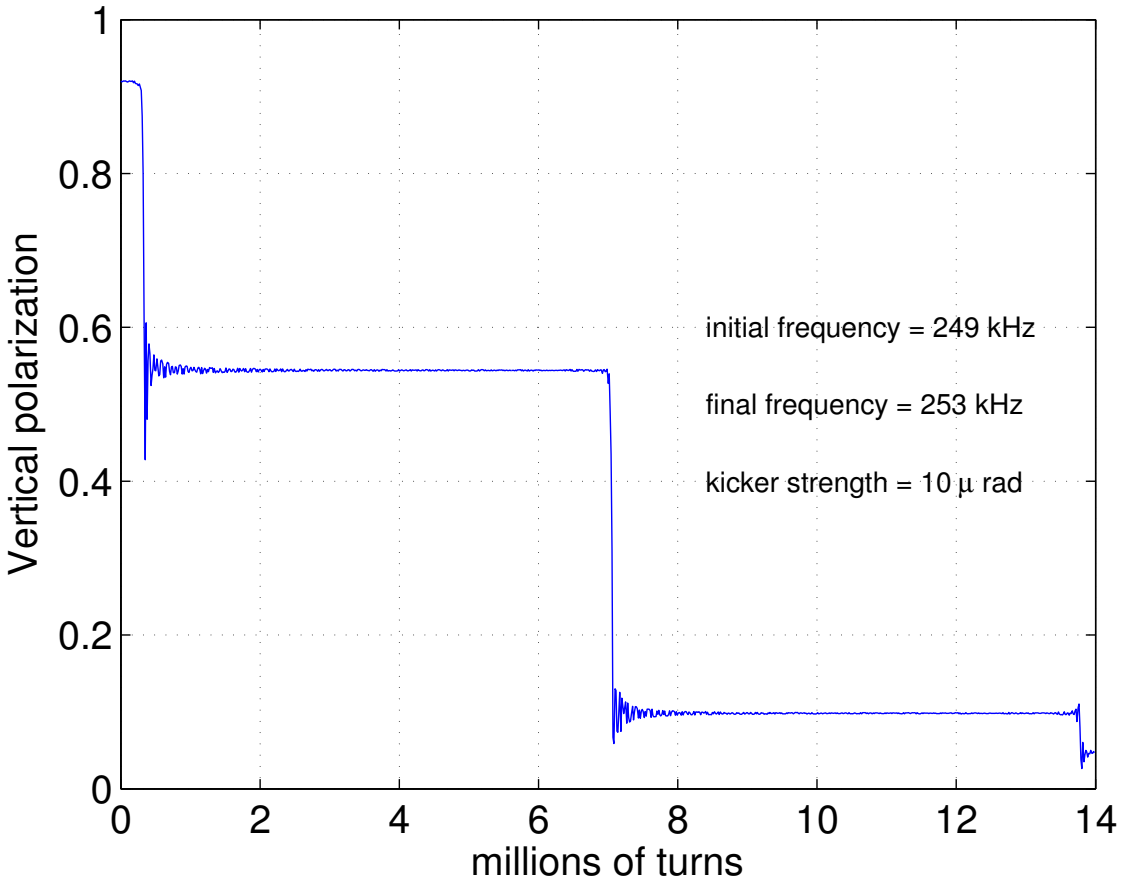

Figure B.5: Polarization procedure with 10 μrad kicker strength and frequency scan from 249 to 253 kHz.

Appendix C

Momentum compaction factor measurements

The momentum compaction factor is the dependence of the beam path length on the momentum change and it is given by:

$$\alpha = \frac{\mathrm{d}L/L}{\mathrm{d}p/p} \tag{C.1}$$

where L is the path length, p is the beam momentum.

The momentum compaction factor also determines the variation of beam momentum changing the RF cavity frequency:

$$\frac{\mathrm{d}f}{f} = -\alpha \frac{\mathrm{d}p}{p} \tag{C.2}$$

A precise measurement of the momentum compaction factor needs a precise way to measure the beam energy. The beam energy can be measured at different RF frequency.

Two different methods to measure the beam energy are possible: one uses the x-ray spectra from undulators, one uses the method of spin depolarization.

Beam energy from the undulator spectrum

The spectrum of the photon beam of an undulator consists on many peaks, at different harmonics. The photon energy of the nth harmonic, at an observation angle θ, is given by:

$$E_n(\theta) = \frac{0.95\, E_0^2\, n}{\lambda_u \left(1 + K^2/2 + \gamma^2\theta^2\right)} \tag{C.3}$$

where E_0 is the energy of the electron beam in GeV, λ_u is the undulator magnetic period in cm, γ is the Lorentz factor of the electron beam, K is the dimensionless parameter of the undulator and it is given by [44]:

$$K = \frac{eB_0\lambda_u}{2\pi\beta m_e c} \tag{C.4}$$

where B_0 is the peak magnetic field of the undulator, $\beta = v/c$, c is the speed of light, m_e is the electron mass.

The K parameter depends on the size of the undulator gap. An energy measurement has been done at ESRF with a precision better than 0.1% [45].

Beam energy from the spin depolarization

Energy measurements using the spin depolarization have been done VEPP-4 in Novosibirk [46], at LEP [13], at SLS [14] [47], at the Australian Synchrotron [48] [15], at Spear3 [15] and other facilities.

A polarized beam can be unpolarized with a sinusoidal magnetic field perpendicular to the dipoles field applied to the beam. The frequency must be related to the precession frequency of the spin:

$$f_{dep} = f_0(n + \nu_{spin}) \tag{C.5}$$

where ν_{spin} is the fractional part of the spin tune.

A polarized electron beam has a longer Touschek lifetime than an unpolarized one, as written in section 2.1, so f_{dep} can be changed until the lifetime become shorter. The spin tune can be obtained and therefore the energy of the beam can be measured.

Although attempts have been made to measure the energy with resonant depolarization at ESRF, the results have not yet been satisfactory.

Appendix D

Dynamic aperture with synchrotron oscillations

The dynamic aperture is the area, in the x-y plane, in which a particle without transverse momentum can be injected without being lost. It can be found using a particle tracking code.

The synchrotron motion can slightly change the dynamic aperture, because off axis particles travel on a different trajectory and they arrive to the cavity without the exact synchronous phase. This effect is very small in the present ESRF lattice and it is usually neglected. In figure D.1, the dynamic aperture with and without cavity are shown for present ESRF lattice. The dynamic apertures are very similar.

In all versions of the new low emittance upgrade lattice, the effect of the synchrotron oscillations in the dynamic aperture is significantly larger. In figure D.2, the dynamic apertures with and without RF cavity are shown.

In version S28 of the low emittance ESRF upgrade lattice, the dynamic aperture is reduced, including the longitudinal motion, by about 30 % both in horizontal and in vertical.

Using a particle tracking code, the lengthening of the trajectory after a single turn in the ring for different amplitudes, in horizontal and vertical, can be computed.

In figures D.3 and D.4, the difference between the length of the trajectory of the particle and the length of the trajectory of the reference particle are shown as a function of x and y initial coordinates, for the present ESRF lattice and for the upgrade lattice.

The lengthening is sextupole dependent: changing the strengths of the sextupoles, the trajectory lengthening changes.

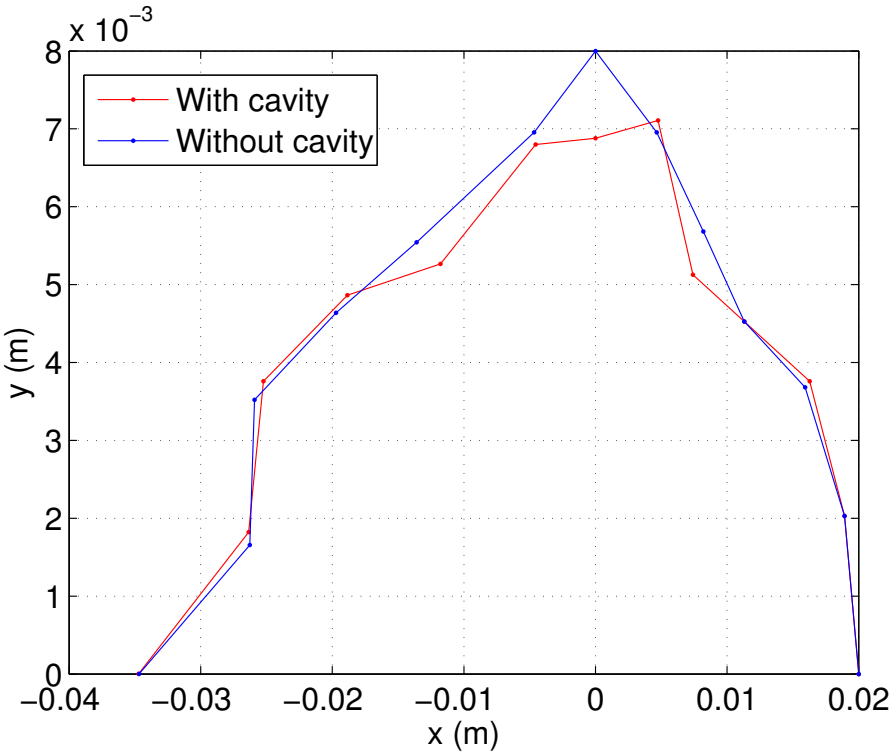

Figure D.1: Dynamic aperture of the ESRF lattice, computed with AT, without physical apertures, without errors, without radiation, with and without RF cavity.

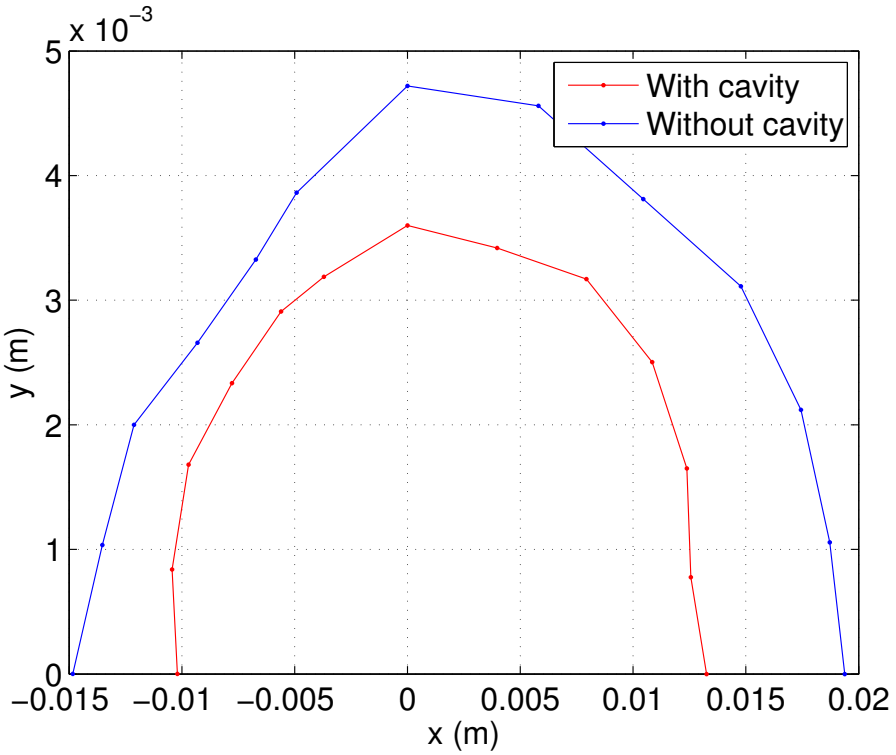

Figure D.2: Dynamic aperture of the new low emittance ESRF upgrade lattice, computed with AT, without physical apertures, without errors, without radiation, with and without RF cavity.

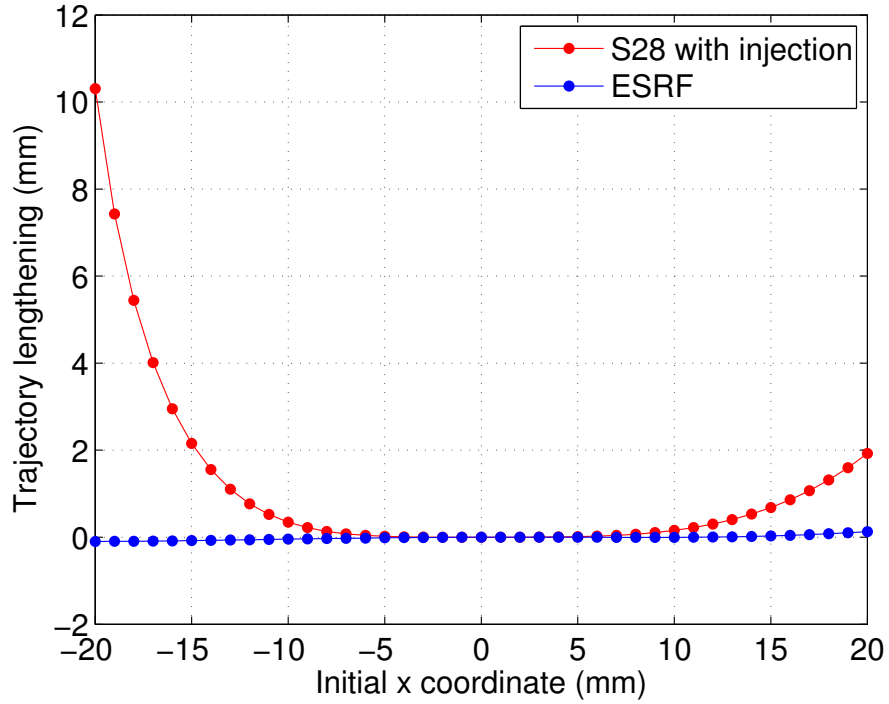

Figure D.3: Trajectory lengthening versus initial x coordinate for two different lattices: the present ESRF one and the S28 version of the upgrade.

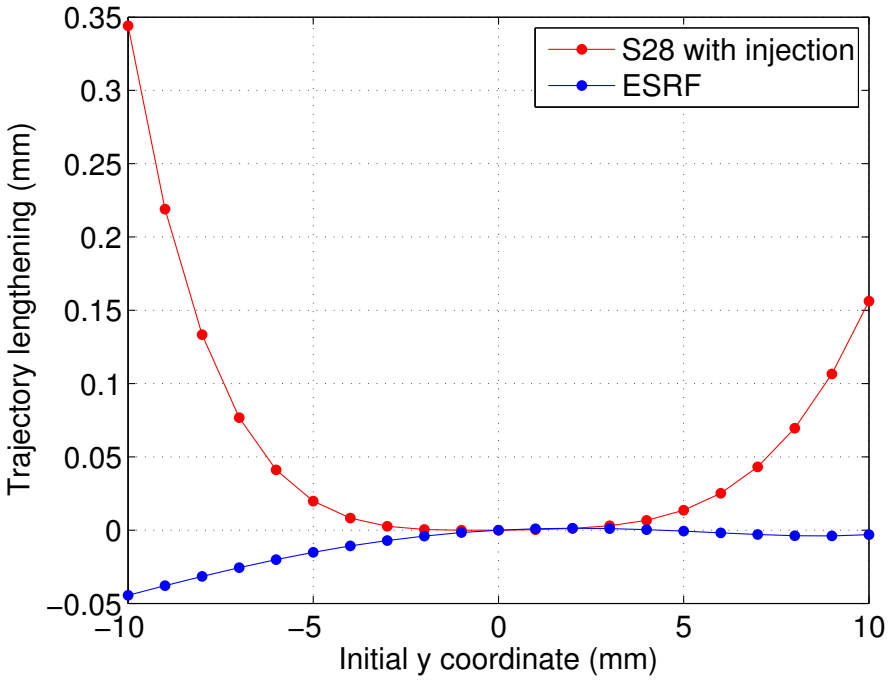

Figure D.4: Trajectory lengthening versus initial y coordinate for two different lattices: the present ESRF one and the S28 version of the upgrade.

List of Tables

List of Figures

Bibliography

[1] J.-L. Revol, J.-C. Biasci, J.-F. Bouteille, F. Ewald, L. Farvacque, A. Franchi, G. Gautier, L. Goirand, M. Hahn, L. Hardy, J. Jacob, J. M. Koch, M. Langlois, G. Lebec, J.-M. Mercier, T. Perron, E. Plouviez, P. Raimondi, K. Scheidt, and V. Serriere. ESRF operation and upgrade status. *Proceedings of IPAC2013*, 2013. 5

[2] L. Farvacque, N. Carmignani, J. Chavanne, A. Franchi, G. Le Bec, S. Liuzzo, B. Nash, T. Perron, and P. Raimondi. A low-emittance lattice for the ESRF. *Proceedings of IPAC2013*, 2013. 9

[3] S. C. Leemann, A. Andersson, M. Eriksson, L.-J. Lindgren, E. Wallen, J. Bengtsson, and A. Streun. Beam dynamics and expected performance of Sweden's new storage-ring light source: MAX IV. *Physical Review Special Topics Accelerators and Beams*, 12(120701), 2009. 9

[4] M. E. Biagini, M. Boscolo, P. Raimondi, S. Tomassini, M. Zobov, J. Seeman, M. Sullivan, U. Wienands, W. Wittmer, S. Bettoni, E. Paoloni, A. Bogomyagkov, I. Koop, E. Levichev, S. Nikitin, P. Piminov, and D. Shatilov. New low Emittance Lattice for the Super-B Accelerator. Technical report, SLAC-PUB-14652. 9

[5] J. Le Duff. Single and multiple Touschek effects. Technical Report CERN-89-01, CERN, 1989. 13

[6] H. Bruck. *Accélérateurs Circulaires de Particules: Introduction à la théorie*. Presses Universitaires de France, Paris, 1966. 14

[7] H. Wiedemann. *Particle Accelerator Physics*. Springer, third edition, 2007. 14, 90

[8] A. Piwinski. The Touschek effect in strong focusing storage rings. Technical Report 98-179, DESY, November 1998. 16

[9] F. Wang. Touschek Lifetime Calculations for the NSLS-II Electron Storage Ring. Technical Report B/SHR-2006-1, MIT-Bates, 2006. 16

[10] A. A. Sokolov and I. M. Ternov. On polarization and spin effects in theory of synchrotron radiation. *Soviet Physics Doklady*, 8:1203, 1964. 17

[11] A. Chao and M. Tigner. *Handbook of Accelerator Physics and Engineering*. World Scientific, 1999. 17, 90, 102

[12] J. Beringer and et al. (Particle Data Group). Review of Particle Physics (RPP). *Physical Review*, D86:010001, 2012. 18

[13] L. Arnaudon, B. Dehning, P. Grosse-Wiesmann, R. Jacobsen, M. Jonker, J. P. Koutchouk, J. Miles, R. Olsen, M. Placidi, R. Schmidt, J. Wenninger, R. Assmann, and A. Blondel. Accurate determination of the LEP beam energy by resonant depolarization. *Zeitschrift fur Physik C*, (66):45–62, 1995. 19, 116

[14] S. C. Leemann, M. Boge, M. Dehler, and A. Streun. Precise beam energy calibration at the SLS storage ring. *Proceedings of EPAC 2002, Paris, France*, 2002. 19, 116

[15] K. P. Wootton, M. J. Boland, W. J. Corbett, X. Huang, G. S. LeBlanc, M. Lundin, H. P. Panopoulos, J. A. Safranek, Y.-R. E. Tan, G. N. Taylor, K. Tian, and R. P. Rassool. Storage ring lattice calibration using resonant spin depolarization. *Physical Review Special Topics Accelerators and Beams*, 16:074001, July 2013. 19, 116

[16] V. S. Morozov, A. W. Chao, A. D. Krisch, M. A. Leonova, R. S. Raymond, D. W. Sivers, V. K. Wong, and A. M. Kondratenko. Narrow Spin Resonance Width and Spin Flip with an rf-Bunched Deuteron Beam. *Physical Review Letters*, 103, September 2009. 20

[17] G. W. Ford and C. J. Mullin. Scattering of Polarized Dirac Particles on Electrons. *Physical Review*, 108:477–481, October 1957. 20

[18] G. W. Ford and C. J. Mullin. Scattering of Polarized Dirac Particles on Electrons. *Physical Review*, 108:1485–1485, June 1958. 20

[19] S. R. Mane, Y. M. Shatunov, and K. Yokoya. Spin-polarized charged particle beams in high-energy accelerators. *Reports on Progress in Physics*, 68:1997–2265, 2005. 20

[20] T. Lee, J. Choi, and H. S. Kang. Simple determination of Touschek and beam-gas scattering lifetimes from a measured beam lifetime. *Nuclear Instruments and Methods in Physics Research*, A(554):85–91, 2005. 20

[21] Wolfram Research, Inc. Mathematica, Version 8.0. Champaign, IL, 2010. 22

[22] F. Ewald, P. Elleaume, L. Farvacque, A. Franchi, D. Robinson, K. Scheidt, A. Snigirev, and I. Snigireva. Vertical emittance measurement at the ESRF. *Proceedings of DIPAC 2011*, 2011. 23

[23] K. Scheidt. Review of streak cameras for accelerators: features, applications and results. *Proceedings of EPAC 2000, Vienna, Austria*, 2000. 25

[24] A. Streun. Momentum acceptance and Touschek lifetime. SLS Note 18/97, Paul Scherrer Institut, November 1997. 25

[25] B. Nash, L. Farvacque, and J. Jacob. RF Voltage calibration and Touschek Lifetime versus RF voltage. Technical report, ESRF, February 2011. 26

[26] Anke-Susanne Müller. *Precision Measurements of the LEP Beam Energy for the Determination of the W Boson Mass*. PhD thesis, Johannes Gutenberg-Universität in Mainz, 2000. 26

[27] A. Terebilo. Accelerator modeling with Matlab Accelerator Toolbox. *Proceedings of the 2001 Particle Accelerator Conference*, 2001. 30, 37

[28] K. Scheidt and B. Joly. Upgrade of beam phase monitors for the ESRF injector and storage ring. *Proceedings of IBIC 2013*, 2013. 31

[29] V. Serriere. *Longitudinal beam dynamics in electron storage rings with harmonic RF systems for bunch lengthening*. PhD thesis, University Paris XI, November 2002. 34, 103

[30] C. Limborg. *Brilliance ultime des sources de rayonnement synchrotron de la 3ème génération alimentées par un anneau de stockage potentiel de ces sources à produire des impulsions de rayons X durs courtes et intenses*. PhD thesis, Universite Joseph Fourier Grenoble, Octobre 1996. 34

[31] M. Borland. elegant: A flexible sdds-compliant code for accelerator simulation. Advance Photon Source LS-287, September 2000. 36, 102

[32] http://mad.web.cern.ch/mad/. 37

[33] M. Belgroune, P. Brunelle, and L. Nadolski. Refined tracking procedure for the SOLEIL energy acceptance calculation. *Proceedings of the 2003 Particle Accelerator Conference*, pages 896–898, 2003. 37

[34] M. Borland, V. Sajaev, L. Emery, and A. Xiao. Multi-objective direct optimization of dynamic acceptance and lifetime for potential upgrades of the Advanced Photon Source. Technical Report APS LS-319, Advanced Photon Source, August 2010. 37, 63

[35] A. Streun. Beam Lifetime in the SLS Storage Ring. Technical Report SLS-TME-TA-2001-0191, Paul Scherrer Institut, December 2001. 51

[36] K. Kubo, S. K. Mtingwa, and A. Wolski. Intrabeam scattering formulas for high energy beams. *Physical Review Special Topics Accelerators and Beams*, 8, August 2005. 77

[37] S. Liuzzo. *Optimization studies and measurements for ultra-low emittance lattices*. PhD thesis, Università degli studi di Roma "Tor Vergata", 2013. 82

[38] S. Y. Lee. *Accelerator Physics*. World Scientific, 1999. 90

[39] J. Haïssinski. Exact longitudinal equilibrium distribution of stored electrons in the presence of self-fields. *Il Nuovo Cimento*, Volume 18:pp 72–82, November 1973. 102

[40] T. Perron. Impedance and Collective Effects Evaluation for the new Machine. Technical Report 13-01, ESRF, February 2013. 103, 104

[41] T. Demma. Private correspondence, 2013. 105

[42] J. D. Bjorken and S. K. Mtingwa. Intrabeam scattering. *Particle Accelerators*, (13):115, 1983. 105

[43] K. L. F. Bane. Intra-beam scattering, impedance, and instabilities in ultimate storage rings. Technical report, SLAC-PUB-14892, March 2012. 105

[44] H. Onuki and P. Elleaume. *Undulators, Wigglers and their Applications*. Taylor & Francis, 2003. 116

[45] E. Tarazona and P. Elleaume. Measurement of the absolute energy and energy spread of the ESRF electron beam using undulator radiation. *Review of Scientific Instruments*, 1996. 116

[46] A. A. Zholentz, L. M. Kurdadze, M. Yu. Lelchuk, S. I. Mishnev, S. A. Nikitin, E. V. Pakhtusova, V. V. Petrov, I. Ya. Protopopov, E. L. Saldin, V. A. Sidorov, A. N. Skrinsky, G. M. Tumaikin, A. G. Chilingarov, Yu. M. Shatunov, B. A. Shwartz, S. I. Eidelman, and Yu. I. Eidelman. High precision measurement of the $\psi-$ and $\psi'-$ meson masses. *Physics Letters*, 96B:214–216, October 1980. 116

[47] S. C. Leemann. Precise Energy Calibration Measurement at the SLS Storage Ring by Means of Resonant Spin Depolarization. Master's thesis, ETHZ IPP, March 2002. 116

[48] H. P. Panopoulos, K. P. Wootton, M. J. Boland, and R. P. Rassool. Electron beam energy measurement at the australian synchrotron storage ring. *Proceedings of IPAC2011*, 2011. 116